Title

Search For Flavor Changing Neutral Currents and Lepton Family Number Violation in Neutral Two-Body Charm Decays

Journal

Physical Review D, 61(32005)

Author

Pripstein, D.

Publication Date

1999-06-08

LBNL-40586
UC-414

ERNEST ORLANDO LAWRENCE
BERKELEY NATIONAL LABORATORY

A Search for Flavor Changing Neutral Currents and Lepton Family Number Violation in Neutral Two-Body Charm Decays

David A. Pripstein

Physics Division

June 1997

Ph.D. Thesis

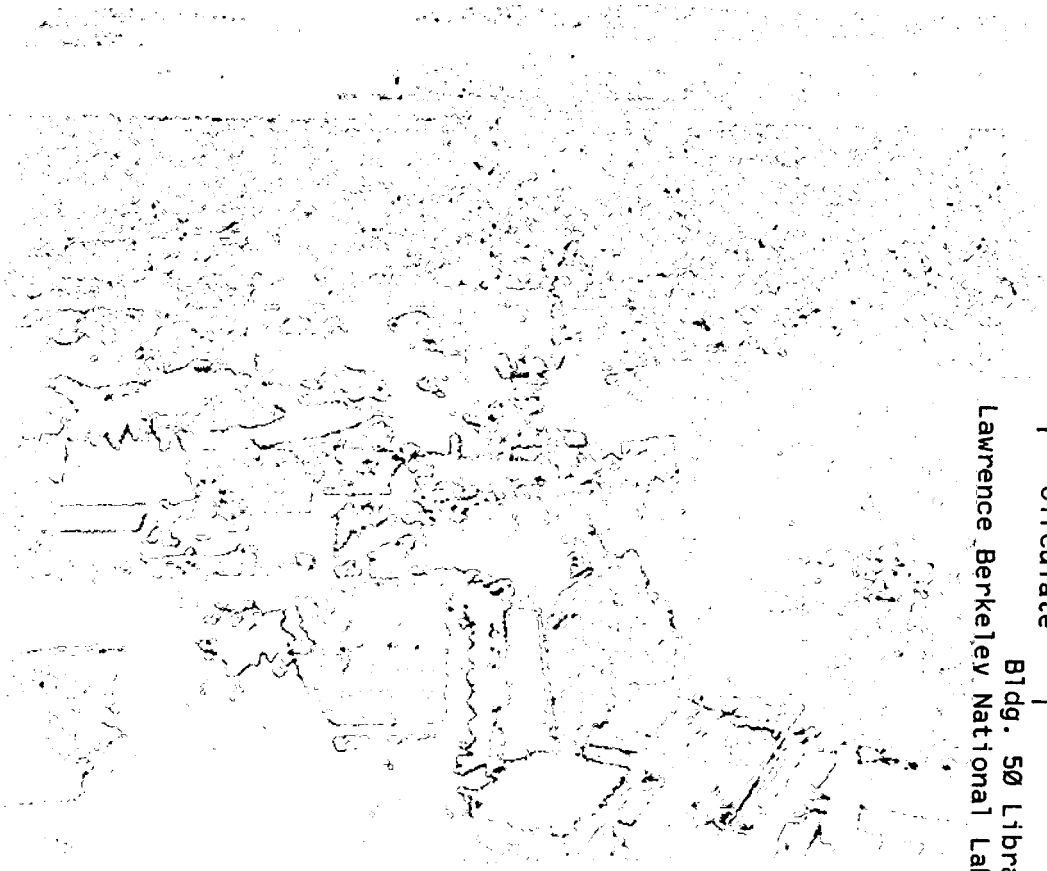

DISCLAIMER

A Search for Flavor Changing Neutral Currents and Lepton Family Number Violation in Neutral Two-Body Charm Decays

by

David Aaron Pripstein

A dissertation submitted in partial satisfaction of the

requirements for the degree of

Doctor of Philosophy

in

Physics

in the

GRADUATE DIVISION

of the

UNIVERSITY OF CALIFORNIA, BERKELEY

Committee in charge:

Professor Kam-Biu Luk, Chair
Professor Gilbert Shapiro
Professor Selig Kaplan

June 1997

A Search for Flavor Changing Neutral Currents and Lepton Family Number Violation in Neutral Two-Body Charm Decays

by

David Aaron Pripstein

Abstract

A Search for Flavor Changing Neutral Currents and Lepton Family Number Violation in Neutral Two-Body Charm Decays

by

David Aaron Pripstein

Doctor of Philosophy in Physics

University of California, Berkeley

Professor Kam-Biu Luk, Chair

This work presents a search for three rare/forbidden neutral charm decays, $D^0 \to \mu e$, $D^0 \to \mu\mu$, and $D^0 \to ee$. This study was based on data collected in Experiment E789 at the Fermi National Accelerator Laboratory using 800 GeV/c proton-gold interactions. Two statistical analyses are presented, one with background subtraction and the other without background subtraction. No evidence is found for any of the decays and the following upper limits are presented at the 90% confidence level:

	Without background subtraction	With background subtraction
$D^0 \to \mu\mu$	2.85×10^{-5}	1.56×10^{-5}
$D^0 \to ee$	1.34×10^{-5}	6.05×10^{-6}
$D^0 \to \mu e$	3.07×10^{-5}	2.35×10^{-5}

Contents

List of Figures

List of Tables

Acknowledgments

In my tenure here at Berkeley I have had the privilege of working with a number of fine, talented people. With talent abundant in our field, the pleasant demeanor is a jewel I was fortunate to discover over and over. I will surely fail to acknowledge everyone who deserves mention, and most certainly fail in giving anyone their full measure.

With the above disclaimer, I begin with my previous life working with the Chamberlain group. They were interesting times, the impact of which I am still realizing. Having Herb, Owen, and Gil to guide me from academics into the beginnings of a project being built from the ground up was invaluable. In addition, I learned a great deal watching Pier keep politics from tearing it down. Jeanne's constant smile was a pleasure and her help in keeping a hectic time organized made life a good deal easier. The lessons I learned from Ray are still presenting themselves years after our work was done. To enumerate them is not possible. I can safely say, the time I spent with Ray is time I will never forget. Through Ray I met Bojan, a truely gentle, ever friendly, person and a master at his craft. Though not formally from Berkeley at the time, Emlyn adopted us and we him. He shared the pressure, frustration, and triumph. For it, he remains part of that disfuctional family that came together for the *Compton*.

As I move on to my time spent on E789, it is appropriate to point out that through both experiments and through three semesters of TA'ing, Matt and I became a team. As unlikely a union as one might imagine, Matt and I became colleagues and friends. We shared an office, an apartment, two advisors, and too many sunrises. Though I've only been to one Grateful Dead concert and he has only done one pull-up, I suspect the influence we have had on each other together with the mutual respect that developed along the way, will last a lifetime.

In many respects the time on E789 began as a breath of fresh, be it incredibly

cold, air. Our collaboration was filled with a bunch of fine folk from many institutions. I list them in no particular order and would like to emphasize that this was, en tout, one of the more pleasant gathering of physicists: Shekhar, Tom, Mike, Yen-chu, Jen-Chieh, Chuck, Dan, Martin, Don, Pat, Jon, Derek, Krish, and the rest of E789 - An interesting group, I look forward to working (or just drinking) with any of you again.

This brings me to the Berkeley contingent of E789. Finding two nicer people than Kam-biu or George would be difficult. Kam-biu's enthusiasm is infectious, and he has been a wonderful teacher. I am pleased to pass from being his student to being his colleague, and friend. Having known George since I was much younger than I am now, I can say with all certainty, he is a true Mensch and a pleasure to work with.

The physics community lost a talent, and very good guy when Ming decided to join the real world. It was a further loss, for us, when Ping did the same. Shigeki's expertise will also be missed. Shigeki made a world of difference as he smoothed my journey into the perils of Latex and the wonders of Perl. He served as both sounding board and companion, I wish him luck.

I would also like to thank Selig for serving on my committee, he was both accommodating and friendly, what more could a student ask for?

I mentioned Gil earlier in the context of our work on the *Compton*, he contiued to serve as a member on my committee. Gil is one of the smartest and genuinely nicest people I know.

Granted I never actually worked with Mike or Richard, but how can I fail to acknowledge two guys who were so happy to see me every single day I was there.

On campus I learned from some wonderful instructors. Professors Suzuki, Jackson, Littlejohn and Zumino were a pleasure. Foremost, I was fortunate to discover Professor Commins, and ended up taking at least five semesters of courses he taught. Anyone who knows him, knows how lucky I was.

Speaking of the Physics Department, each and every graduate student has to be thankful for Anne and Donna. I wonder if they realize just how much their help makes our world seem that much more bearable - Thank You.

Through all of this my father watched. I remember first arriving at LBL and having people walk up to me to tell me how much they liked my dad. He stayed out of the way when it came to matters regarding the degree. However, seeing him in action as a physicist, leader, and person taught me a good deal. I am proud to be his son.

Mom, Jeremy, and Laura (also known as, Mom, Brother, Sister), I suppose this makes it official. I am sure we'll find something else to worry about.

Chapter 1

Introduction

This work presents a search for three neutral charm decays, $D^0 \to \mu e$, $D^0 \to \mu\mu$, and $D^0 \to ee$. This study was based on data collected in Experiment E789 at the Fermi National Accelerator Laboratory. The latter two decays are expected to be very rare and the former, forbidden. As a result, any signal in the region of current sensitivities would most certainly be a signature for new physics.[1]

1.1 Standard Model Prediction

With the absence of Lepton Family Number Violation (LFNV) in the Standard Model, $D^0 \to \mu e$ is forbidden. However, extensions to the Standard Model can accommodate $D^0 \to \mu e$ decay and will be discussed below.

Charm and Flavor Changing Neutral Currents

$D^0 \to \mu\mu$ and $D^0 \to ee$ each require a Flavor Changing Neutral Current (FCNC). In fact, the study of FCNC's and the predictions for the existence of charm were closely correlated. In the late 1960's the theory of electro-weak interactions as proposed by Weinberg [2] and Salam [3] along with the three quark flavors as introduced earlier by Gell-Mann [4] and Zweig [5] explained the observed weak charged current processes in term of the W bosons. However, for the theory to be renormalizable, neutral current processes should have been observed as well. This requirement of the theory led to the expectation

[1] see [1] for a discussion of contributions from both the Standard Model and simple extensions to the Standard Model.

that the branching ratio of $K_L^0 \to \mu^+\mu^-$ be comparable to the branching ratio for the observed process $K^+ \to \mu^+\nu_\mu$ (63.51%) [6] . Instead, there is a difference of $\sim$ eight orders of magnitude in the measured values ($B(K_L^0 \to \mu^+\mu^-) = 7.2 \times 10^{-9}$ [7]). A solution to this dilemma was proposed by Glashow *et al* [8] who postulated a fourth quark that would form a second weak isospin doublet with the strange quark. The GIM mechanism[2] allowed for the cancellation of FCNC at the tree level and thus suppressed the decay $K_L^0 \to \mu^+\mu^-$ accordingly. This cancellation was discussed in detail by Gaillard and Lee [9]. This same discussion used the measured decay rate of $K_L^0 \to \mu^+\mu^-$ and the calculated decay amplitudes of this process, modified by the charm quark, to predict the mass of this yet undiscovered quark.

That same year (1974), two groups found a resonance near the predicted mass for a $c\bar{c}$ bound state, named J/Ψ [10] [11]. By 1976 with the discovery of the D^0 meson decaying into $K\pi$ and $K\pi\pi$ [12], the existence of the charm quark was no longer in doubt.[3]

As mentioned above, $D^0 \to \mu\mu$ and $D^0 \to ee$ each require an FCNC and are thus forbidden at the tree level in the Standard Model. At the one loop level, as shown in Figure 1.1, the decays are GIM and helicity suppressed; thus very small. The one loop contribution to the decay rate is

$$\Gamma(D^0 \to l^+l^-) = \frac{G_F^4 m_W^4 f_D^2 m_l^2 m_D \mid F \mid^2}{32\pi^3}\sqrt{1 - 4m_l^2/m_D^2} \tag{1.1}$$

where

$$F = U_{us}U_{cs}^*(x_s + \frac{3}{4}x_s^2 \log x_s) + U_{ub}U_{cb}^*(x_b + \frac{3}{4}x_b^2 \log x_b) \tag{1.2}$$

with m_l being the lepton mass, m_D the D^0 mass, G_F the Fermi coupling constant, f_D the pseudo-scalar decay constant, m_W the mass of the W boson, $x_i = m_i^2/m_W^2$, and U_{uj}, U_{ck}^* the Cabibbo-Kobayashi-Maskawa (CKM) mixing matrix elements[1]. For $D^0 \to \mu\mu$ this yields a branching ratio of approximately 10^{-19} ($D^0 \to ee$ is at least three orders of magnitude smaller due to helicity suppression). As shown in Figure 1.2, the contribution of long range effects, through intermediate hadronic states for example, can raise the branching ratio as

[2] After its authors, Glashow, Iliopoulos, and Maiani.

[3] The term *open charm* refers to particles with a single charm quark. Indirect evidence of *open charm* came earlier than 1976, [13][14] but the direct observation of the D^0 decaying to $K\pi$ left no doubt. Reference [15] gives a wonderful discussion of *open charm* production.

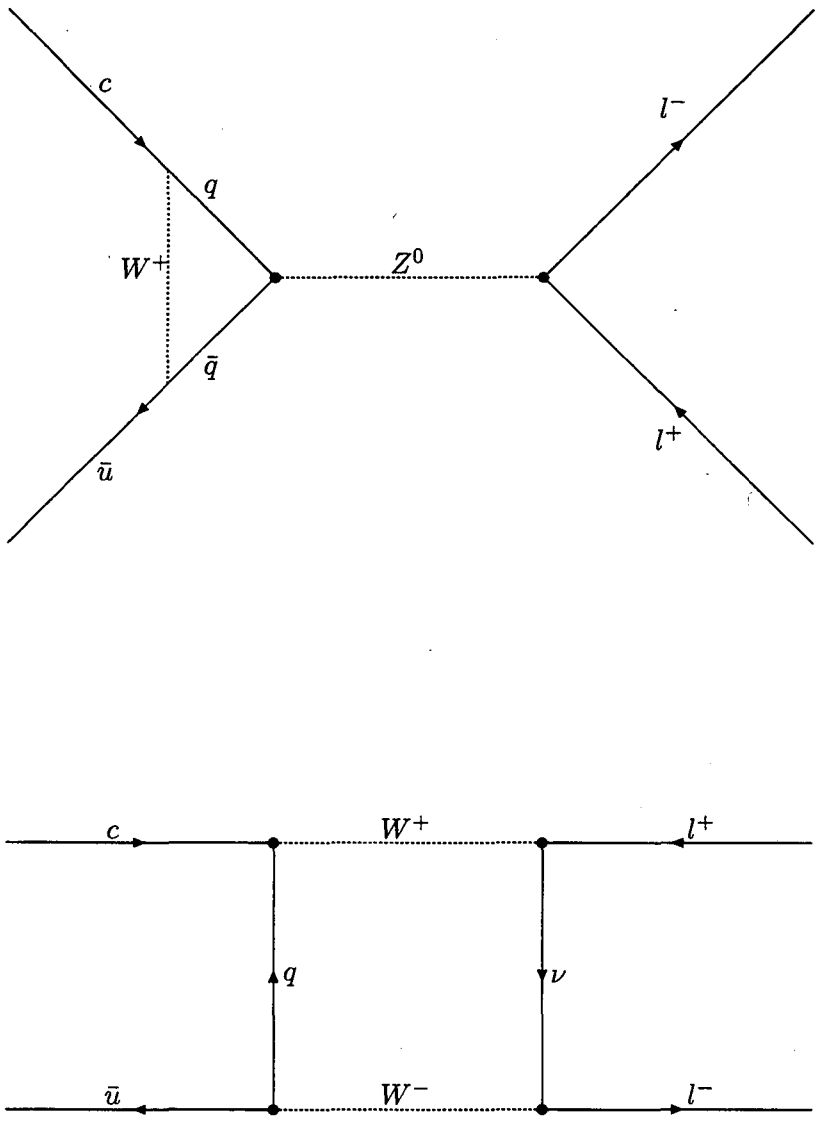

Figure 1.1: Some Feynman diagrams for short range processes that contribute to the decay $D^0 \to l^+l^-$ in the Standard Model.

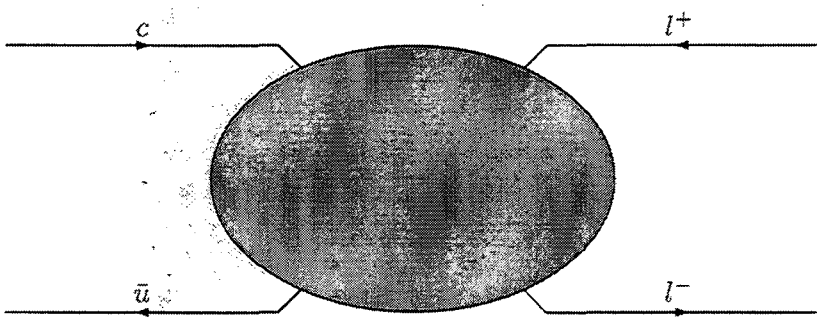

Figure 1.2: Long range contributions to $D^0 \to l^+l^-$ in the Standard Model.

high as 10^{-15} but still many orders of magnitude away from the current measured limits of around 10^{-5}.

1.2 Just beyond the Standard Model

Extensions just outside the Standard Model often allow for both Flavor Changing Neutral Currents and Lepton Family Number Violation. Lepton Family Number Violation and its possible manifestations has been thoroughly reviewed in reference [16]. The current limits for $D^0 \to \mu e$ ($\sim 10^{-5}$) are much less stringent than that on the equivalent decay for K_L^0 ($\sim 3.3 \times 10^{-11}$) [17], or on another commonly cited decay from the lepton sector, $\mu \to e\gamma$ (with a branching ratio of less than 4.9×10^{-11} [18]). However, the presence of the charm sector allows for the study of mechanisms otherwise suppressed or possibly hidden. Furthermore, if the new model involves a Higgs-like mechanism with the coupling proportional to the quark mass, the relatively heavy charm quark would then enhance that coupling.[4]

[4]See [19] for a detailed discussion of the Higgs mechanism.

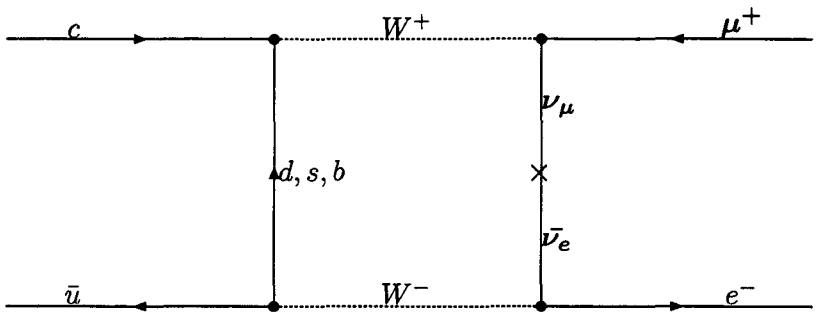

Figure 1.3: Feynman Diagram for $D^0 \rightarrow \mu e$ with Massive Neutrino.

The following lists a few mechanisms that may result in one, or more, of the three $D^0 \rightarrow$ *dilepton* decays being searched for in this analysis:

• Reference [20] discusses a leptoquark of charge -1/3, which as the name implies, couples to both quarks and leptons. In this case the leptoquark couples up-like quarks to charged leptons and down-like quarks to neutral leptons. In the charm sector this coupling leads naturally to the decay $D^0 \rightarrow \mu e$, while in the Strange sector, the decay $K^0 \rightarrow \bar{\nu_\mu}\nu_e$ results. The search for $K^0 \rightarrow \bar{\nu_\mu}\nu_e$ is much more difficult to perform, and thus $D^0 \rightarrow \mu e$ is the natural process in which such a mechanism may be found.

• A fourth generation of quarks along with a heavy neutrino could allow for a larger decay amplitude for $D^0 \rightarrow \mu\mu$, as long as the new generation coupled to the first two generations. With $m_{b'} > 100\ GeV/c^2$ and $U_{ub'}U_{cb'} \geq 0.01$, the branching ratio $B(D^0 \rightarrow \mu\mu)$ is greater than 10^{-11} [1][21].

• A massive fourth generation neutrino (N^0) can allow for $D^0 \rightarrow \mu e$ (see Figure 1.3). Acker[22] shows that with the upper bound on the braching ratio of $\mu \rightarrow e\gamma$, and $M_{N_0} > 45\ GeV/c^2$ [7], $\mid U_{Ne}U^*_{N\mu} \mid^2$ can be constrained to less than 7.1×10^{-6}. This limits the branching ratio for $D^0 \rightarrow \mu e$ to less than 10^{-22} [1].

• If a generic FCNC or LFNV Higgs boson exists, $D^0 \rightarrow$ *dilepton* decays can occur at the lowest order. As shown in Figures 1.4 and 1.5, $D^0 \rightarrow$ *dilepton* decay via the Higgs

boson is topologically identical to $D^+ \to \mu^+\nu$ which is allowed in the Standard Model at the lowest order. The similar kinematics associated with these processes allows for a simple comparison of the decay rates. The amplitude for the decay $D^+ \to \mu^+\nu$ in the Standard Model is

$$M(D^+ \to \mu^+\nu) = g_W^2/2M_W^2 \sin\theta_W(\mu_L\gamma_\alpha\bar{\nu_\mu}) \times (\bar{c_L}\gamma_\alpha d_L) \tag{1.3}$$

whereas

$$M(D^0 \to \mu e) = g_H^2/2M_H^2(\mu_L\gamma_\alpha\bar{e_L}) \times (\bar{c_L}\gamma_\alpha d_L) \tag{1.4}$$

for $D^0 \to \mu e$ through the new Higgs. The ratio of the decay rates yields,

$$\frac{\Gamma(D^0)}{\Gamma(D^+)} = \frac{g_H^4 M_W^4 \tau_{D^+}}{g_W^4 M_H^4 \sin^2\theta_W \tau_{D^0}}. \tag{1.5}$$

Assuming the relative coupling $g_W^2/g_H^2 \approx 1$ and the mass of the new Higgs be $6 \times M_W$, using the lifetimes of each particle ($\tau_{D^0} \approx 0.4 \times 10^{-12}\ sec, \tau_{D^+} \approx 1 \times 10^{-12}\ sec$ [7]), and the current limit of 7×10^{-4} for the branching ratio of $D^+ \to \mu\nu$, the $D^0 \to \mu e$ could happen at a level of 5×10^{-6}. Pakvasa adapted a gauged family symmetry and using the limits for δM_{kaon} and for $B(K_L^0 \to \mu e)$, he got a branching ratio $B(D^0 \to \mu e) \sim 10^{-13}$ [1]. Of course this flavor changing Higgs could also contribute to $D^0 \to \mu\mu$.

There are many other mechanisms (e.g. GUT, flipped left-right symmetry[23], and Technicolor) that also allow any of the above $D^0 \to l^+l^-$ processes to occur. It is generally difficult to make reliable predictions for their contributions and none predict branching ratios within six orders of magnitude of the current limits. Again, if one of the above modes is detected (especially $D^0 \to \mu e$) it is likely that new physics has been discovered.

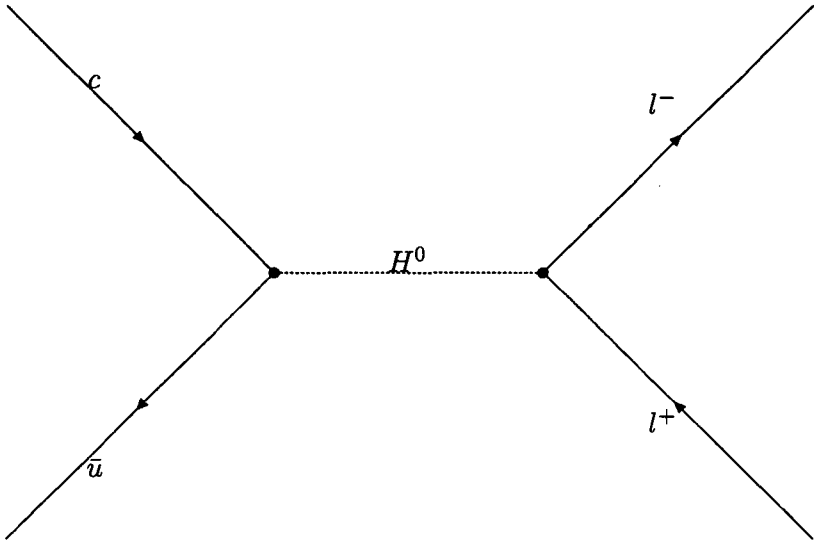

Figure 1.4: Feynman Diagram for $D^0 \to \mu e$ through neutral Higgs.

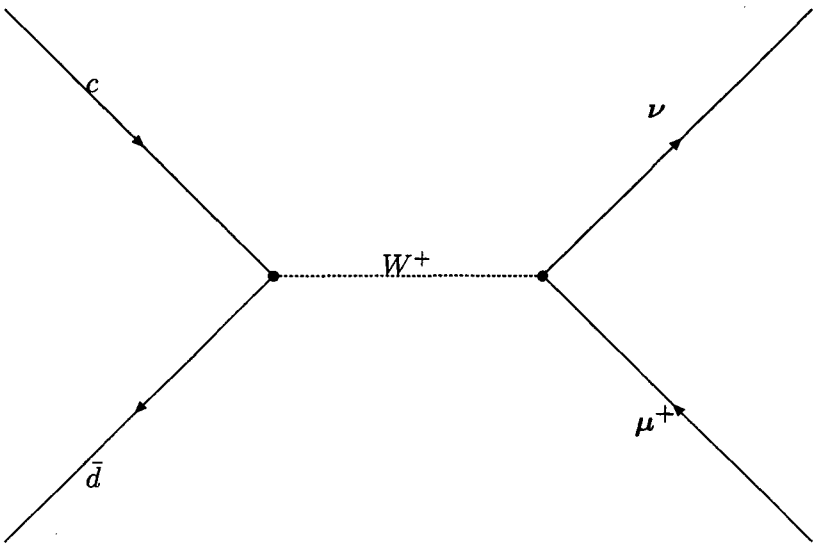

Figure 1.5: Feynman Diagram for $D^+ \to \mu^+ \nu$ decay.

Chapter 2

Experiment

The E789 experiment was carried out in the Meson East Beam line at the Fermi National Accelerator Laboratory. A beam of protons was delivered to a fixed target of either gold or beryllium. Downstream of the target, the E789 spectrometer was used to select and record processes of interest. The spectrometer had a tunable acceptance which, for this analysis, was used to select two-body decays of the D^0 meson.

2.1 The beam

The FNAL Tevatron delivered an 800 GeV beam of protons to the experiment, as a series of beam packets over a one-minute spill cycle. Each spill consisted of a ramp cycle where no beam was delivered followed by a twenty-three second beam delivery cycle. The beam delivery was further divided into intervals of 19 ns duration called buckets. Each bucket contained a single proton packet of approximately 1 ns in duration. The beam was distributed as evenly as possible among the buckets with a total between $(1-3)\times 10^{10}$ protons per spill. The cross section of the beam spot reflected the profile of the target; namely, wide in one transverse dimension (≈ 1 cm in X) and narrow in the other (0.2 mm in Y). The beam divergence was < 4 μrad in the wide dimension and < 200 μrad in the narrow dimension. A right-handed Cartesian coordinate system was selected with the beam direction coinciding with the positive Z-direction. The Y-direction was chosen to be vertically upward. The term 'downstream' is then associated with increasing Z-coordinate. This is the convention used for the entire analysis.

2.2 The E789 Spectrometer

The spectrometer,[1] as shown in Figure 2.1, with its two opposite polarity bending magnets and limited aperture was capable of confining its acceptance to particle decays of interest. The geometry and configuration were optimized for two-body processes with high transverse momentum and were further restricted to accept either Charm or Beauty decays, depending on the running period. The components of the spectrometer were as follows:

- Beam intensity and targeting monitors.
- A Silicon Strip Detector (SSD) just after the target and used to locate downstream decays.
- A copper Beam dump.
- Two bending magnets: SM12, and SM3. In addition to tuning the acceptance, SM3 was also used as a track-momentum analyzer.
- Three tracking stations consisting of drift chambers and hodoscopes.
- A sampling calorimeter with the front-end configured for detecting electrons and the back configured for hadrons.
- A muon identification station, located at the end of the spectrometer, consisting of shielding followed by both hodoscopes and proportional tubes.

There was also a Ring Imaging Cerenkov Detector but it was not used for this analysis.

2.2.1 Target

The target apparatus was installed in the beam vacuum and designed to allow for convenient switching between gold and beryllium targets. In addition, half way through the data taking period, the targets were replaced with targets of different dimensions. The installation of the new targets coincided with the change in SM12 magnet current from 1000 A to 900 A. Table 2.1 is a summary of the targets used for the data taken in this analysis. In each running period the dimensions of the Au target were the same as those of

[1] E789 and its predecessors generated many papers and theses. Reference [24] includes another fine description of the apparatus.

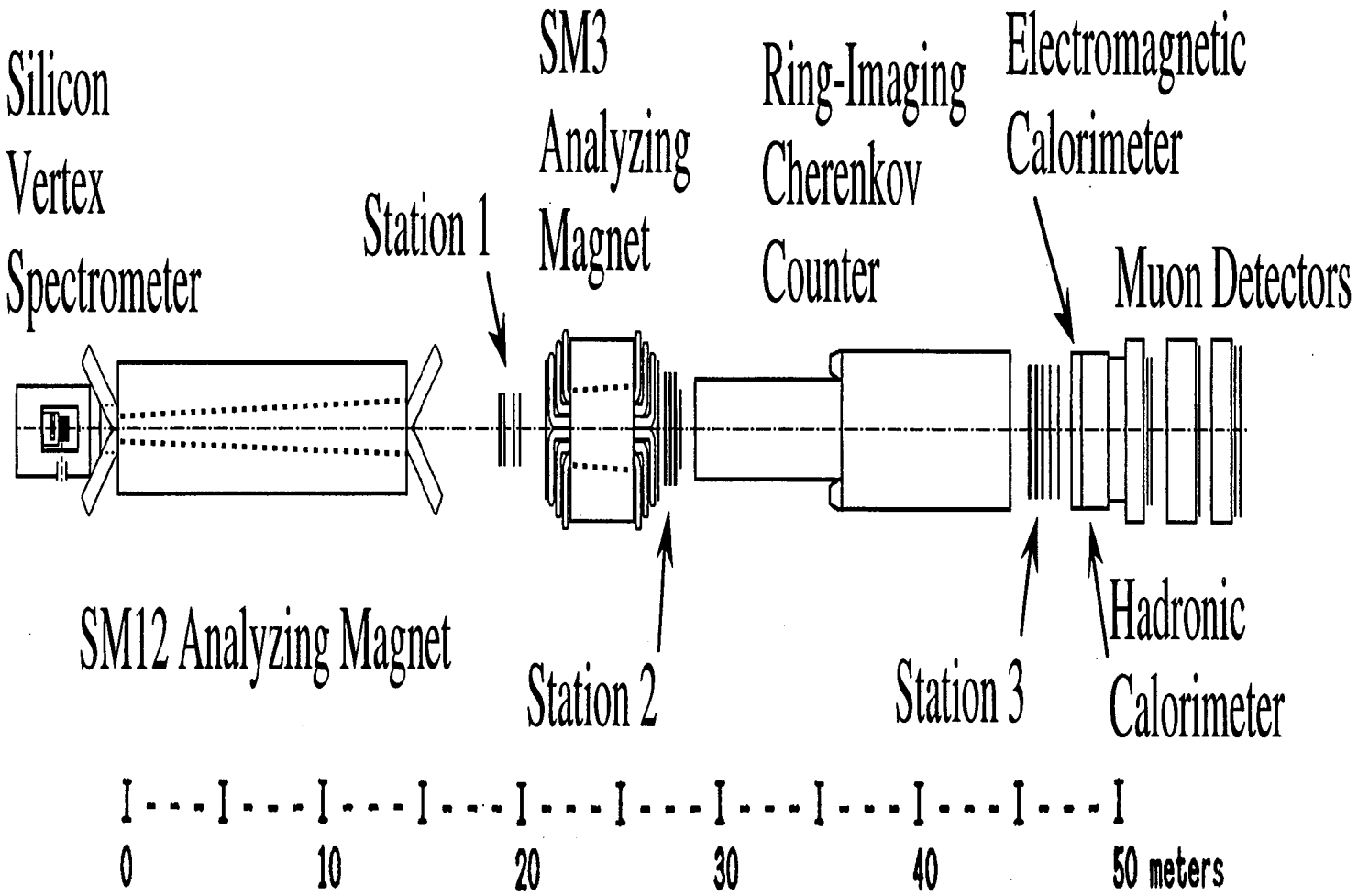

Figure 2.1: E789 Spectrometer.

	900A	1000A
Length in Z (mm)	1.5	0.8
Width in Y (μm)	150	100

Table 2.1: Target dimensions.

the Be target. The targets were much larger than the beam in the X dimension but were narrow in the Y (bend plane) dimension. The target centers were located at $\sim -130.65\ in$.

2.2.2 Beam Monitors

Beam intensity was measured using both an ion chamber and a secondary emission monitor (*SEM*), located upstream of the target. In addition, the targeting fraction was determined using an interaction monitor (*AMON*) which was simply a shielded scintillator telescope facing the target and perpendicular to the beam. The number of interactions was thus proportional to *AMON* and the targeting fraction proportional to $\frac{AMON}{SEM}$. The absolute targeting fraction could be determined by simply sweeping the target across the beam. The targeting fraction varied from 30% to 40% depending on the running conditions (see [25] for details).

2.2.3 Silicon Strip Detector (SSD)

The SSD was located just downstream of the target and consisted of two arms, each containing eight planes of detectors (see Figure 2.2). The individual plane included a silicon strip detector with a 50 μm strip pitch and an active area of approximately 5 cm by 5 cm; the thickness of the active area was 300 μm. The planes were arranged in two arms to cover a $20 - 60\ mr$ region above and below the beam. The eight planes in each arm had one of three orientations, Y, U, or V with a rotation about the Z-axis of 0°, +5°, or −5°. Each arm had the same sequential orientation, namely Y U Y V Y U Y V (see Table 2.2). The readout electronics allowed for 8544 strips to be recorded with almost one bucket resolution. To minimize secondary interactions, thermal fluctuations and detector degradation, the SSD containment area was temperature-controlled by filling with helium at 10° C. Table 2.2 lists the configuration of the SSD planes.

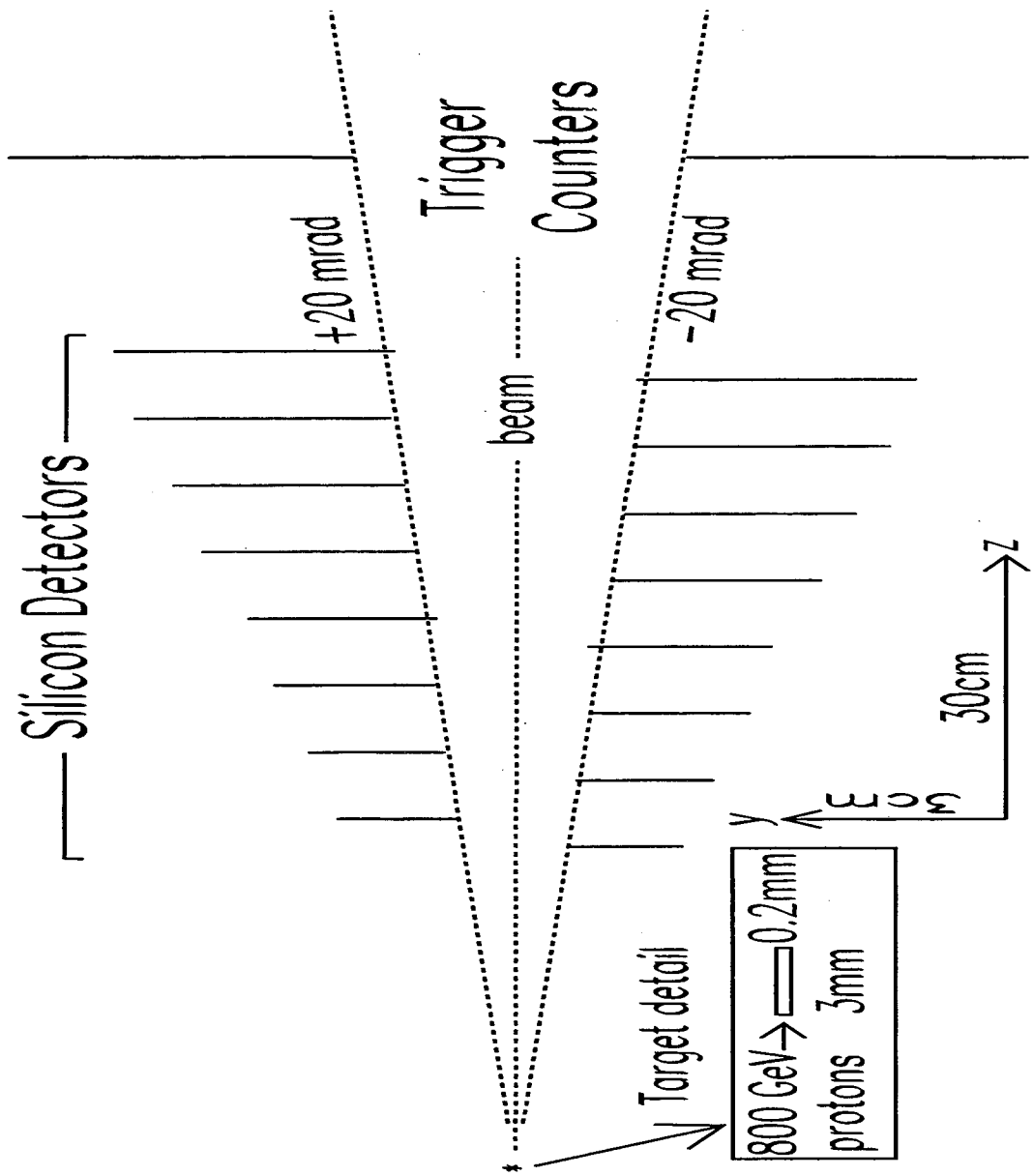

Figure 2.2: E789 Silicon Strip Detector.

Plane No.	Plane Name	Z-Position (cm)	Y-Position (cm)	Plane View	Arm	Number of Strips
1	Y1B	-294.54	-2.125	Y	Lower	316
2	Y1T	-291.36	0.949	Y	Upper	316
3	U2B	-286.92	-2.300	U	Lower	372
4	U2T	-283.74	1.066	U	Upper	372
5	Y3B	-279.30	-2.758	Y	Lower	436
6	Y3T	-276.12	1.548	Y	Upper	436
7	V4B	-271.68	-2.865	V	Lower	500
8	V4T	-268.50	1.721	V	Upper	500
9	Y5B	-264.07	-3.364	Y	Lower	572
10	Y5T	-260.88	2.217	Y	Upper	572
11	U6B	-256.44	-3.566	U	Lower	628
12	U6T	-253.26	2.289	U	Upper	628
13	Y7B	-248.82	-4.018	Y	Lower	692
14	Y7T	-245.64	2.805	Y	Upper	692
15	V8B	-241.20	-4.154	V	Lower	756
16	V8T	-238.02	2.925	V	Upper	756

Table 2.2: Silicon Strip Detector configuration.

2.2.4 Beam Dump

The E789 beam dump was a water cooled slab of copper placed along the beam trajectory after the SSD and inside the magnet SM12 (see Figure 2.3). The beam dump served to prevent unused protons and particles of low transverse momentum from entering the spectrometer. Its tapered design coupled with the baffles on the inside walls of SM12 limited the aperture for target-generated particles.

2.2.5 Spectrometer Magnets

The spectrometer contained two focusing magnets: SM12 and SM3. Together they served to guide the trajectory of charged particles in the desired momentum phase space through the aperture of the spectrometer. As mentioned earlier, the spectrometer was optimized for two-body Charm or Beauty decays. By adjusting the magnet currents in SM12 and SM3 the acceptance could be optimized for the process of interest. The magnetic fields of both magnets were carefully mapped out with the Fermilab Ziptrack. The profiles of the field were used in the data analysis.

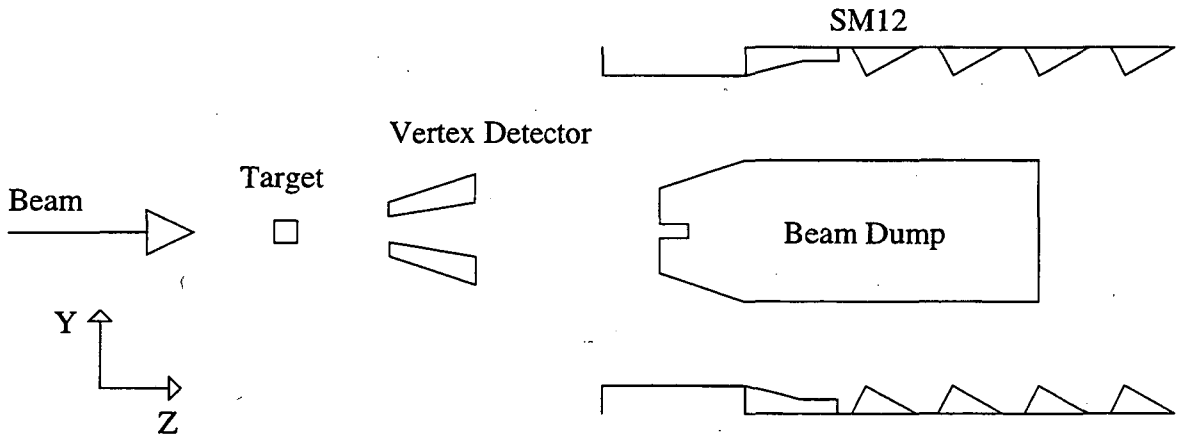

Figure 2.3: Schematic of Target through SM12, including beam dump.

SM12

SM12 was the upstream bend magnet. It was a 1200 *ton* 14.5 m-long open aperture conventional dipole magnet. At an operating current of 900 A, SM12 provided a vertical transverse impulse (P_t) of 1.6 GeV/c to the charged particle, optimal for studying a D^0 decaying to two particles.

SM3

SM3 was the second bending magnet, located between tracking stations 2 and 3 (see Figure 2.1). It served the dual purpose of complementing SM12 in focusing and providing a momentum analysis for charged particles traversing it. SM3 was a 3.4 m-long open aperture conventional magnet which, when run at an operating current of 4268 A, provided a 0.91 GeV/c vertical P_t impulse that was almost uniform throughout its aperture.

2.2.6 Tracking Stations

Three tracking stations were used to determine the charged particle trajectories through the spectrometer. The tracking information was provided by a series of multi-wire drift chambers with each station having two groups of three chambers for a total of eighteen chambers. Each grouping of three chambers, a triplet, included identical chambers except for a rotation about the Z axis to provide three dimensional tracking. The orientations, labeled Y, U, and V, were 0°, +14°, and −14° from the Y axis respectively. The second

triplet had a like orientation with designations Y′, U′ and V′. The two groups of triplets in each tracking station were offset from each other by half a cell width to resolve the left-right tracking ambiguity. The drift medium in the chambers was a gas mixture of 49.6% ethane, 49.7% argon and 0.7% isopropyl alcohol. Each sense wire of the drift chamber was connected to its own Time to Digital Converter (TDC) used to measure the drift time of the electrons from primary ionization. At operating voltages of around 2000 V, the drift velocities averaged to about 50 $\mu m/ns$. In each of the tracking stations, there were two hodoscope planes providing fast, albeit course, tracking information used in the trigger (Station 2 only had one plane). Each hodoscope plane consisted of two half planes of scintillator paddles whose light was collected using light guides and fed into Hamamatsu R329 fast photo-multiplier tubes for read out. The scintillator paddles for each plane were arranged to provide either measurement in Y (Stations 1 (HY1), 2 (HY2), and 3 (HY3) or in X (Stations 1 (HX1) and 3 (HX3)). See Table 2.6 for the hodoscope plane configurations.

2.2.7 Calorimeter

The E789 Calorimeter was used for identifying electrons and hadrons; it was a sampling calorimeter which consisted of an electromagnetic section with a hadronic section abutted behind. The electromagnetic section consists of four lead/scintillator longitudinal layers of 2, 5, 5, and 6 radiation lengths, respectively, and a total of 0.3 nuclear interaction lengths. Each layer consisted of a separate left and right section which was further divided into twelve modules for vertical resolution. Each of the resulting 96 modules (12 x 2 x 4) was read out individually, with the analog signal from the scintillator converted to digital using an ADC. The hadronic section consisted of two Iron/scintillator longitudinal layers of 2 and 6 interaction lengths with a total of 80 radiation lengths. As with the electromagnetic section, there were a left and right segment each divided into thirteen modules for vertical resolution. The hadronic section had 52 modules for a total of 148 modules over the entire calorimeter (see Figure 2.4). For details regarding the calibration see Section 3.3.

2.2.8 Muon Station

The Muon Station was located at the end of the spectrometer and contained three planes of multi-wire proportional tubes and two planes of hodoscopes. The proportional tubes were used for off-line muon identification, and consisted of either a plane of horizontal

Plane Name	Z-Position (cm)	Plane View	Number of wire	Wire Spacing (cm)
V1	1879.8	V	208	0.508
V1′	1885.0	V	208	0.508
Y1	1904.5	Y	160	0.508
Y1′	1909.7	Y	160	0.508
U1	1930.3	U	208	0.508
U1′	1935.5	U	208	0.508

Table 2.3: Station One Drift Chambers.

Plane Name	Z-Position (cm)	Plane View	Number of wire	Wire Spacing (cm)
V2	2751.8	V	160	0.986
V2′	2757.2	V	160	0.986
Y2	2776.8	Y	128	1.106
Y2′	2782.1	Y	128	1.106
U2	2802.3	U	160	0.986
U2′	2807.6	U	160	0.986

Table 2.4: Station Two Drift Chambers.

Plane Name	Z-Position (cm)	Plane View	Number of wire	Wire Spacing (cm)
V3	4546.8	V	144	2.021
V3′	4553.8	V	144	2.021
Y3	4572.5	Y	112	2.083
Y3′	4579.5	Y	112	2.083
U3	4598.0	U	144	2.021
U3′	4605.0	U	144	2.021

Table 2.5: Station Three Drift Chambers.

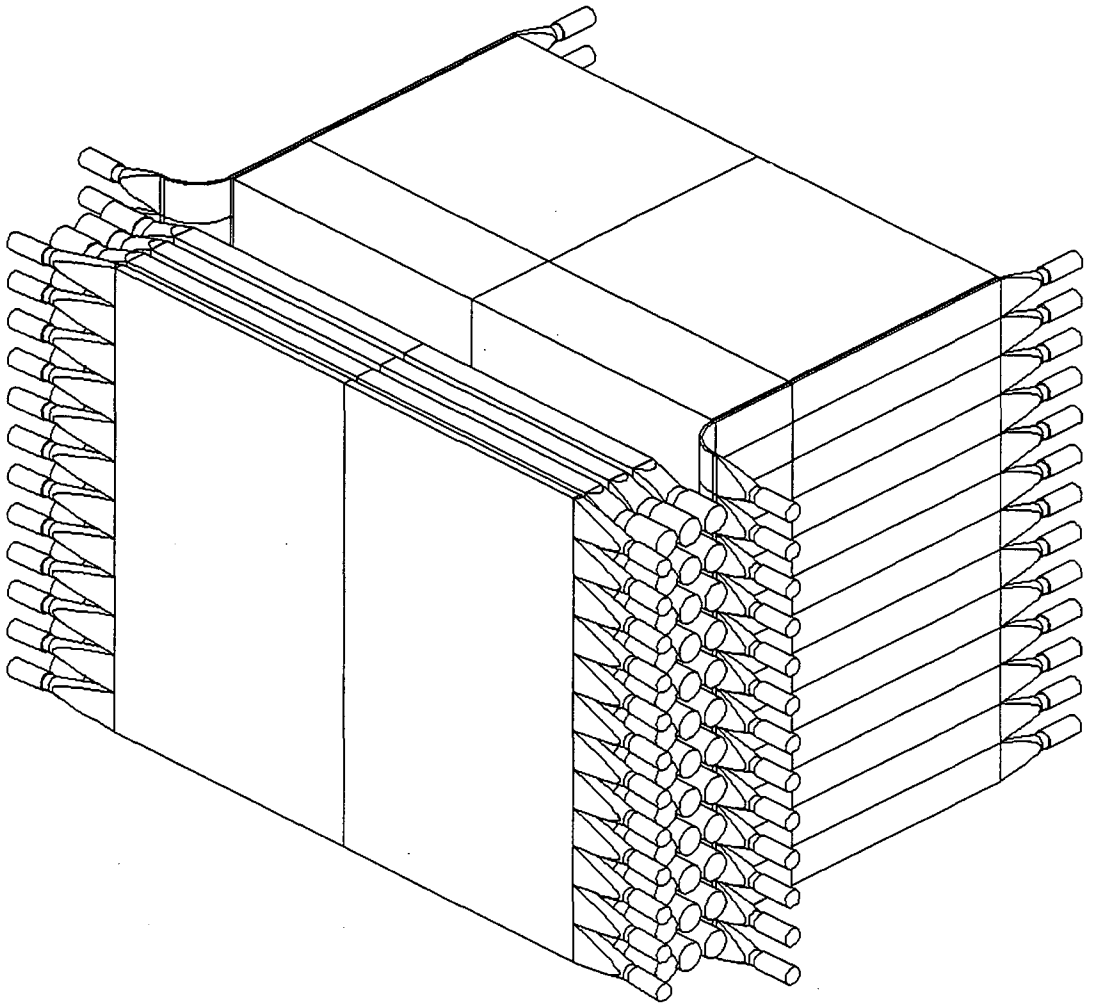

Figure 2.4: E789 Calorimeter.

Plane Name	Z-Position (cm)	Plane View	Number Counters	Aperture	
				X (cm)	Y (cm)
HX1	1959.61	X	12x2	120.75	76.20
HY1	1995.80	Y	2x12	120.35	77.95
HY2	2831.95	Y	2x16	163.83	123.51
HX3	4627.88	X	12x2	267.16	233.68
HY3	4653.28	Y	2x13	264.16	233.68
HY4	5170.17	Y	2x14	294.64	254.00
HX4	5413.04	X	16x2	320.04	289.56

Table 2.6: Hodoscope Planes.

cells for Y determination (PTY1, PTY2) or vertical cells for measuring the X coordinate (PTX). Each plane was made of two layers of 1 in $\times$ 1 in aluminum cells; the layers were offset by half a cell width from the other. They were read out with latches, so no timing information was recorded. The gas mixture used was the same as in the drift chambers. The hodoscopes were comprised of the same scintillator and read-out as those in the tracking stations. They were used for both triggering and particle identification. There were two planes HY4 and HX4, providing Y and X information respectively. The sensitivity of the station to muons stemmed from the shielding both in front of and within the station. With the calorimeter and added zinc blocks, lead, and concrete absorbers, at least 16 interaction length of material lay upstream of the station. In addition, a concrete absorber positioned between HY4 and HX4 added approximately 5 more interaction length of shielding. The configuration of the proportional tube chambers and muon hodoscopes are summarized in Tables 2.6 and 2.7.

Plane Name	Z-Position (cm)	Plane View	Number of wire	Aperture	
				X (cm)	Y (cm)
PTY1	5186.04	Y	120	297.2	304.8
PTX	5425.12	X	135	343.9	308.6
PTY2	5589.90	Y	143	359.4	363.2

Table 2.7: Muon Proportional Tube Chambers.

2.3 Data Acquisition

E789 required a high rate data acquisition system (DAQ) (see [26] for a thorough review of the E789 DAQ system). The DAQ used a pipeline architecture which was configured to maximize throughput. The event readout was supported by a Nevis Transport system which controlled and sequenced the detector output. As the event information came off the Nevis Transport, it was temporarily stored in a memory module before it was piped to the VME-based archiving system which formatted the buffered event packets and fed them out to up to four Exabyte 8200 tape drives. The system was capable of streaming more than a megabyte/second, only limited by the write-speed of the tape drives. The maximum throughput for actual running conditions was approximately 40 megabytes/spill to tape. To supplement event data, scalers summed over an entire spill were also recorded. Spill scalers recorded trigger counts, trigger component counts, and beam intensity information with and without system deadtime.

2.4 Trigger

To enhance the number of events of interest written to tape, a trigger was used. An event was first required to satisfy the Trigger-Fan-In (TFI), a low level fast trigger used to bias the sample towards multi-track events. An event satisfying the TFI was fed to the Trigger-Generator-Output (TGO). The TGO imposed further requirements, targeting events that most likely contained the physics processes being studied. Finally a trigger processor examined hit patterns in stations 1, 2, and 3, as well as hits in the Silicon Strip Detector (SSD) to enhance the prospect of finding events that contained decay vertices downstream of the target that masked to downstream tracks. An event that satisfied all three levels of trigger was then written to tape. In addition, at each level of trigger, some events were prescaled and forced through to the next level.

2.4.1 TFI

As the fastest trigger, the TFI utilized information discerned exclusively from the hodoscopes. Tracking stations 1, 2, and 3 and the muon station (station 4) each contained hodoscopes used in the TFI. The hodoscopes were labeled with either HX or HY denoting the orientation of the scintillator paddles and a number 1, 2, 3, or 4, denoting the station.

The TFI had three separate sub-components, $\frac{n}{4}\mu LR$, $\frac{n}{4}LR$, and $\frac{2}{4}M$. The notation $\frac{n}{4}\mu LR$ represented a logical AND of $\frac{n}{4}\mu L$ with $\frac{n}{4}\mu R$. The component $\frac{n}{4}\mu L$ required that any n of HX1, HY2, HX4 and HY4 fired their left half. Likewise $\frac{n}{4}\mu R$ required n from the same group to fire their right half. The trigger $\frac{n}{4}LR$ imposed a similar requirement except that planes HX1, HY2, HX3, and HY3 were used. There were two separate running periods. In the run with SM12 current set to 1000 A, n was set to 3. In the second period (900A), it was set to 4.[2] Component $\frac{2}{4}M$ used a hodoscope hit pattern matching algorithm called the Matrix. The Matrix used hit combinations in the HY2 and HY3 hodoscope planes to predict hit windows in HY1. The predictions were done with a fast lookup table which was based on Monte Carlo track trajectory simulations (see Figure 2.5). The Matrix divided the spectrometer into four equal quadrants in the X-Y plane and thus a $\frac{2}{4}M$ requirement stipulated that 2 of the 4 quadrants contained hits consistent with a track. All three TFI components were then combined in a logical OR to form the TFI.

2.4.2 TGO

The TGO was a second level trigger used to focus further on events likely to contain processes of interest. The TGO was composed of a series of components that served to select events with either oppositely charged particle tracks or like-sign particle tracks. The like-signed events could be used to study some systematic errors though they were not needed for this analysis. The two-track components consisted of a Matrix combination that required a track in the upper arm of the spectrometer (MU) and a track in the lower arm (MD). There were also scintillators placed at the end of both the upper (SU) and lower (SD) SSD arms to ensure that some tracks traversed the SSD. High multiplicity events were vetoed by counting the number of paddles fired in the hodoscope HX1 ($\overline{NX1}$) and the paddles fired in HX3 ($\overline{NX3}$). Finally the TGO incorporated an event identification component using both the calorimeter and the muon station to characterize the event. Given the character of this analysis, namely that all signal modes are presented as a ratio to the normalization mode, understanding this component of the trigger is vital. The major difference in the acceptance of each event type was due to the event identification segment of the TGO. The dimuon TGO ($\mu^+\mu^-$) required that $2HX4$ and $2HY4$ be satisfied; two paddles in hodoscope HX4 and hodoscope HY4 register a hit respectively (recall that both HX4 and HY4 are

[2]The two running periods were characterized by the SM12 magnet current as discussed in Section 2.

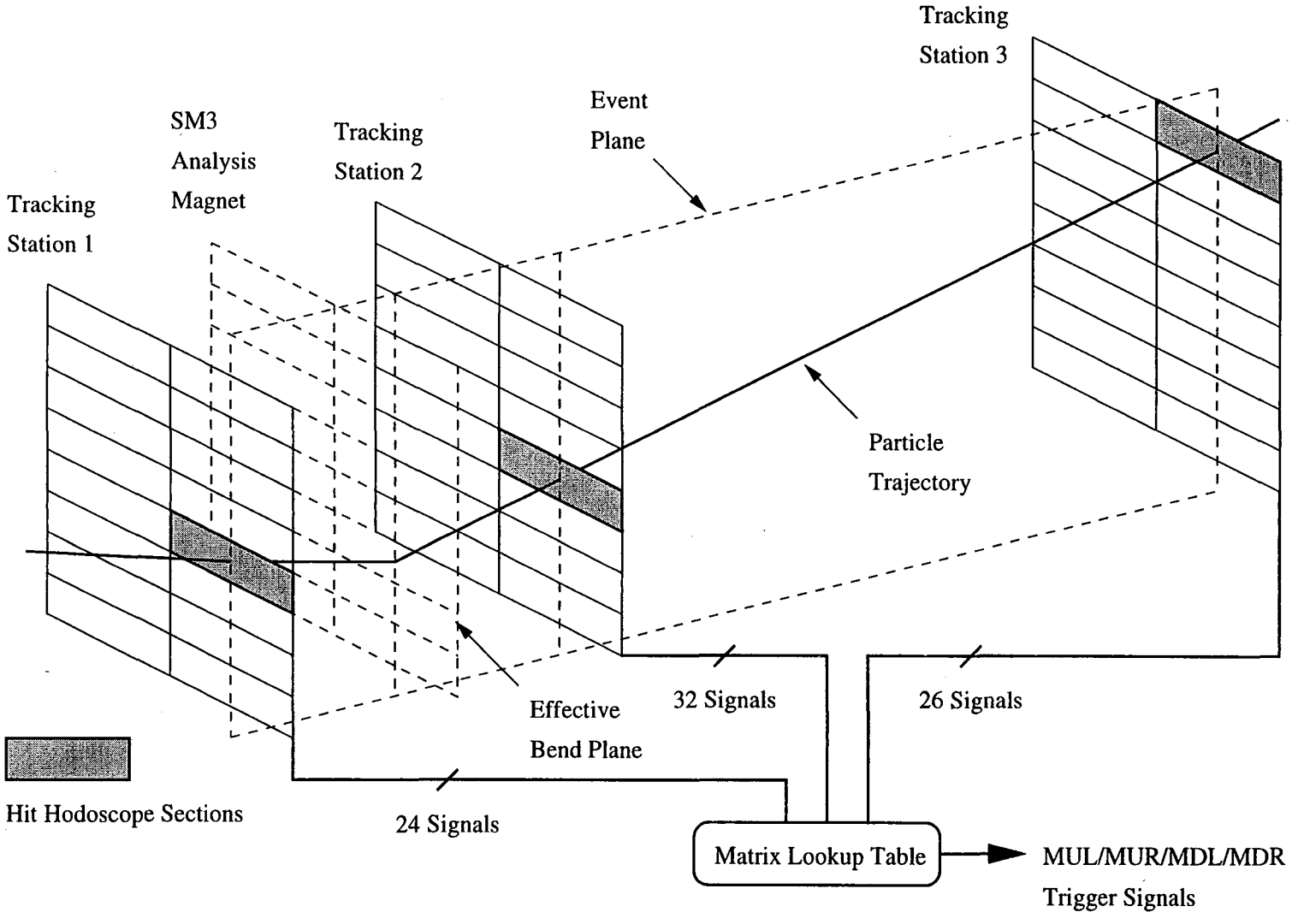

Figure 2.5: Trigger Matrix Schematic.

located in the muon station). The calorimeter provided an analog sum of the dynode signal sensitive to electrons (E2+E3) and a sum sensitive to hadrons (H1+H2+E1+E4). Each sum was further discriminated with a low and high threshold. The low threshold was set for sensitivity to single particles and the high threshold set to pass two-particle events. The notation associated with the various calorimeter trigger components is as follows: for the electromagnetic section e, E for low and high thresholds respectively, and for the hadronic, h, H, again with the upper case referring to the high threshold. Each complete TGO trigger would then consist of $MU \cdot MD \cdot SU \cdot SD \cdot \overline{NX1} \cdot \overline{NX3}$ combined with a logical AND to one of the event ID components. The TGO reduced the trigger rate by about a factor of 30 compared to the TFI. Each TGO is listed in Table 2.8.

2.4.3 Trigger Processor

If an event satisfied one of the TGO triggers, the Trigger Processor then formed combinations of potential target tracks using hits in the Y-drift chambers in station 1, 2, and 3 that were masked by both the hodoscopes and the calorimeter. The potential target tracks were then projected to the SSD and masked SSD hits in the Y-SSD planes. A fast track finding algorithm was then used to determine tracks in the SSD and form resulting vertices.[3] A cut was then made on the impact parameter of the SSD tracks and the location of the vertex to increase the likelihood that the event contained a downstream decay. The Trigger Processor served to further reduce the trigger rate by an order of magnitude beyond the TGO reduction.

Table 2.9 gives a typical spill profile for the TFI, TGO, and Triggers After Processor (TAP). In Table 2.9, l^+l^- refers to any of the dilepton triggers. Clearly the dihadron trigger dominated the dilepton triggers. For one running period, the dihadron trigger was prescaled by a factor of 32 and the intensity was increased to enhance the dilepton sensitivity.

2.5 Data

There were four data sets collected during the running period dedicated to Charm decays. They were labeled as the 1000A-Au, 900A-Au, 900A-Be, and the dedicated dilepton running periods. However, in this analysis only the first three data sets were used. Each of

[3]See [27] for details regarding the E789 Vertex Processor and its implementation.

Trigger Name.	Description
h^+h^-	$M_U \cdot M_D \cdot S_U \cdot S_D \cdot \overline{NX1} \cdot \overline{NX3} \cdot H$
$\mu^+\mu^-$	$M_U \cdot M_D \cdot S_U \cdot S_D \cdot \overline{NX1} \cdot \overline{NX3} \cdot 2HX4 \cdot 2HY4$
e^+e^-	$M_U \cdot M_D \cdot S_U \cdot S_D \cdot \overline{NX1} \cdot \overline{NX3} \cdot E$
$e^\mp\mu^\pm$	$M_U \cdot M_D \cdot S_U \cdot S_D \cdot \overline{NX1} \cdot \overline{NX3} \cdot e \cdot HX4 \cdot HY4$
$h^\mp e^\pm$	$M_U \cdot M_D \cdot S_U \cdot S_D \cdot \overline{NX1} \cdot \overline{NX3} \cdot h \cdot e$
$h^\mp\mu^\pm$	$M_U \cdot M_D \cdot S_U \cdot S_D \cdot \overline{NX1} \cdot \overline{NX3} \cdot h \cdot HX4 \cdot HY4$
$h^\pm h^\pm$	$M_{LIKE} \cdot (S_U + S_D) \cdot \overline{NX1} \cdot \overline{NX3} \cdot H$
$\mu^\pm\mu^\pm$	$M_{LIKE} \cdot (S_U + S_D) \cdot \overline{NX1} \cdot \overline{NX3} \cdot 2HX4 \cdot 2HY4$
$e^\pm e^\pm$	$M_{LIKE} \cdot (S_U + S_D) \cdot \overline{NX1} \cdot \overline{NX3} \cdot E$
$e^\pm\mu^\pm$	$M_{LIKE} \cdot (S_U + S_D) \cdot \overline{NX1} \cdot \overline{NX3} \cdot e \cdot HX4 \cdot HY4$
$h^\pm e^\pm$	$M_{LIKE} \cdot (S_U + S_D) \cdot \overline{NX1} \cdot \overline{NX3} \cdot h \cdot e$
$h^\pm\mu^\pm$	$M_{LIKE} \cdot (S_U + S_D) \cdot \overline{NX1} \cdot \overline{NX3} \cdot h \cdot HX4 \cdot HY4$

Table 2.8: TGO Trigger Components.

Trigger	TFI	TGO	TAP
H^+H^-	1.4×10^6	49×10^3	4.5×10^3
l^+l^-	1.4×10^6	6.8×10^3	$.55 \times 10^3$

Table 2.9: Typical trigger rates per spill.

Data set	$AMON \cdot \overline{SB}$	TAPS
1000A-Au	3.9×10^6	3.8×10^8
900A-Au	8.4×10^5	8.7×10^7
900A-Be	9.8×10^5	7.3×10^7
Dilepton	3.4×10^6	7.0×10^7

Table 2.10: Summary of data sets.

the three analyzed data sets is distinguished by the SM12 current setting (900 A or 1000 A), the target dimensions, and target material (see Section 2). The dedicated dilepton run was identical to the 900A-Au running period except that it focused on the dilepton decays by prescaling the dihadron trigger and increasing the intensity (for details regarding the trigger, see Section 2.4). Each set was processed separately and each yielded a normalization signal ($D^0 \rightarrow K\pi$), a crucial component of the analysis.

The ultimate yield of any data set depended on the reconstructed signal in the normalization mode ($D^0 \rightarrow K\pi$) and the associated efficiencies for each decay mode. However, data sets may also be characterized and compared by considering the number of live interactions, $AMON \cdot \overline{SB}$,[4] and the number of events written to tape (TAPS). Table 2.10 lists each data set collected during the running periods dedicated to two-body Charm decays; only the first three were used for this analysis.

[4] $AMON$ is the count proportional to the number of target interactions and is described in Section 2.2.2. $\overline{SB}$ is *true* when the system is able to accept data. $\frac{AMON \cdot \overline{SB}}{AMON}$ is thus a measure of the *live time* of the data acquisition and ran about 50%.

Chapter 3

The Measurement

The result of this analysis will be a limit on the branching ratio for each of the rare modes, $D^0 \to ee$, $D^0 \to \mu e$, and $D^0 \to \mu\mu$. To determine the ratio, we need the total number of D^0 's produced and the efficiency for each dilepton mode. The number of $D^0 \to l^+l^-$ events is simply the number of decays seen divided by the efficiency for observing the decay. The total number of D^0 's produced can be determined with the observation of a normalization signal, namely $D^0 \to K\pi$. Thus the number of D^0 's produced becomes the number of $D^0 \to K\pi$'s seen divided by both its branching ratio and the efficiency for seeing a $D^0 \to K\pi$. Thus:

$$B(D^0 \to l^+l^-) = \frac{N_{l^+l^-}}{\epsilon_{l^+l^-}} \times \frac{\epsilon_{K\pi} \times B(D^0 \to K\pi)}{N_{K\pi}} \quad (3.1)$$

$$= \frac{B(D^0 \to K\pi) \times \epsilon \times N_{l^+l^-}}{N_{K\pi}} \quad (3.2)$$

where $N_{l^+l^-}$ is the number of $D^0 \to l^+l^-$ events seen, $N_{K\pi}$ is the number of $D^0 \to K\pi$ events seen, $\epsilon_{l^+l^-}$ is the efficiency of observing a $D^0 \to l^+l^-$ event, $\epsilon_{K\pi}$ is the efficiency for observing a $D^0 \to K\pi$ event, and $\epsilon = \frac{\epsilon_{K\pi}}{\epsilon_{l^+l^-}}$ is the relative efficiency. In addition to pinning down the number of D^0 's produced, using a normalization mode also allows for cancellation, or partial cancellation, of many correction factors when the ratio of the efficiencies was formed. For example, many of the trigger components were identical for each mode and thus the efficiencies associated with the common components cancel when the relative efficiency is formed. A second example is the track reconstruction (SSD and Downstream), which involves no particle identification and thus does not distinguish between modes. Again, common efficiencies do not affect the ratio. There are small differences in

the kinematics which slightly affect the relative efficiencies but can be incorporated in the efficiency measurements. It is clear that the existence of a normalization mode provides a powerful handle for the measurement.

The measurement was thus separated into two parts, searching the data for each decay mode, and determining their relative efficiencies. The efficiencies are discussed in Chapter 4, the search for two-body Charm decays is discussed below.

3.1 Event Reconstruction

Finding D^0 decays requires a spectrometer with excellent mass resolution to display a measurable D^0 peak in the reconstructed invariant mass distribution. Good mass resolution depends on accurately determining the momentum of each decay constituent (both are the result of the downstream track reconstruction which used both the tracking stations and the spectrometer magnets). However, by itself, the mass resolution is not sufficient to provide a measurable signal above the background. With a total nuclear inelastic cross section per nucleon for Gold of $\sim 40\ mb$ and an inclusive D^0 production cross section of $\sim 40\ \mu b$ at a center-of-energy of 39 GeV [28], a branching ratio $B(D^0 \to K\pi)$ of $\sim$ 4% [7] results in a search for 1 event in at least 25 thousand for the normalization signal. In this experiment, with an average D^0 decay distance of $\sim 3\ mm$ (corresponding to an average D^0 momentum of 56 GeV/c), precise reconstruction of the decay vertex is thus a powerful tool to separate D^0 decays from other processes predominately occur in or very near the target. For this purpose, the Silicon Strip Detector (SSD) provided the key contribution. The SSD allowed a precise reconstruction of the decay distance and the impact parameter[1] for each track that formed a downstream vertex. The impact parameter could then be used to eliminate tracks likely to come from the target and thus reduced the background significantly. In the end the large $D^0 \to K\pi$ yield demonstrates the efficacy of both the downstream and SSD reconstruction (see Section 5). Finally, events selected as likely candidates had to be categorized by decay type. Event categorization required particle identification which will be discussed later in this Section as well as in Section 4.

[1]The impact parameter is the transverse distance of the track from the target center when it is projected to the z-location of the target.

3.1.1 Downstream Tracking

Downstream track reconstruction began by finding hit clusters in each of the chamber sets in the three tracking stations (see [24] for a detailed description of the downstream tracking). A hit cluster consisted of a hit in one or both Y-planes and in either of the associated U, and V planes for a total of at least 4 out of 6 possible hits. Once the clusters have been found, track segments were formed in stations 2 and 3 which, when projected, masked off clusters in Station 1 that were consistent with tracks coming from the target and not the beam dump. As a result, not all tracks were reconstructed. Only those with the greatest potential of being generated at the target were determined. With a set of clusters in all three tracking stations, the full 18 plane fit was formed (3 stations, 6 chambers each). Tracks that satisfied the final selection criteria with respect to the quality of fit were then stored in the reconstructed track bank that was written out as part of the Data Summary Tape (DST). Since the trajectory of the track was known both before and after SM3 (the second bend magnet), along with the field map of SM3, the momentum associated with the track was determined. The track was then traced back through SM12 (the large bend magnet) based on the field profile, through the SSD, and finally to the target. The trace-back through SM12 was an iterated procedure. The first iteration simply traced the track from SM3 to the target region. Any track that fell outside a pre-defined aperture of ± 5 *in* from the center of the target, or tracked into the beam dump was eliminated. The subsequent iterations required the track to trace very close to the target.[2] The result was a complete trajectory of the particle candidate from the target through the entire spectrometer. The final traceback used the downstream decay vertex determined by the SSD to enhance the determination of the proper decay angle and resulting opening angle. The opening angle, determined from the iterative traceback for the two-body decay with a downstream vertex, coupled to the total momentum of each daughter particle, as determined by SM3, were used to form the invariant mass of the event. Figure 3.1 shows a two-track event from real data that passed all the tightest event selection cuts. The event shows the hit clusters in the tracking stations and hodoscopes. Each track is reconstructed and traced to the target. There are two reconstructed hadrons and one unreconstructed muon that is either from the beam dump or, more likely, falls out of the timing window of the event.[3]

[2] All real tracks that passed the previous loose cuts could come only from the target region; the trace-back was to ~ 1 *mm* downstream of the target to help mask the SSD for downstream decays.

[3] The muon shows drift chamber hits but no hodoscope hits because the hodoscope timing has well under one bucket resolution whereas the drift chambers do not. Thus it is common for an out-of-time track not to

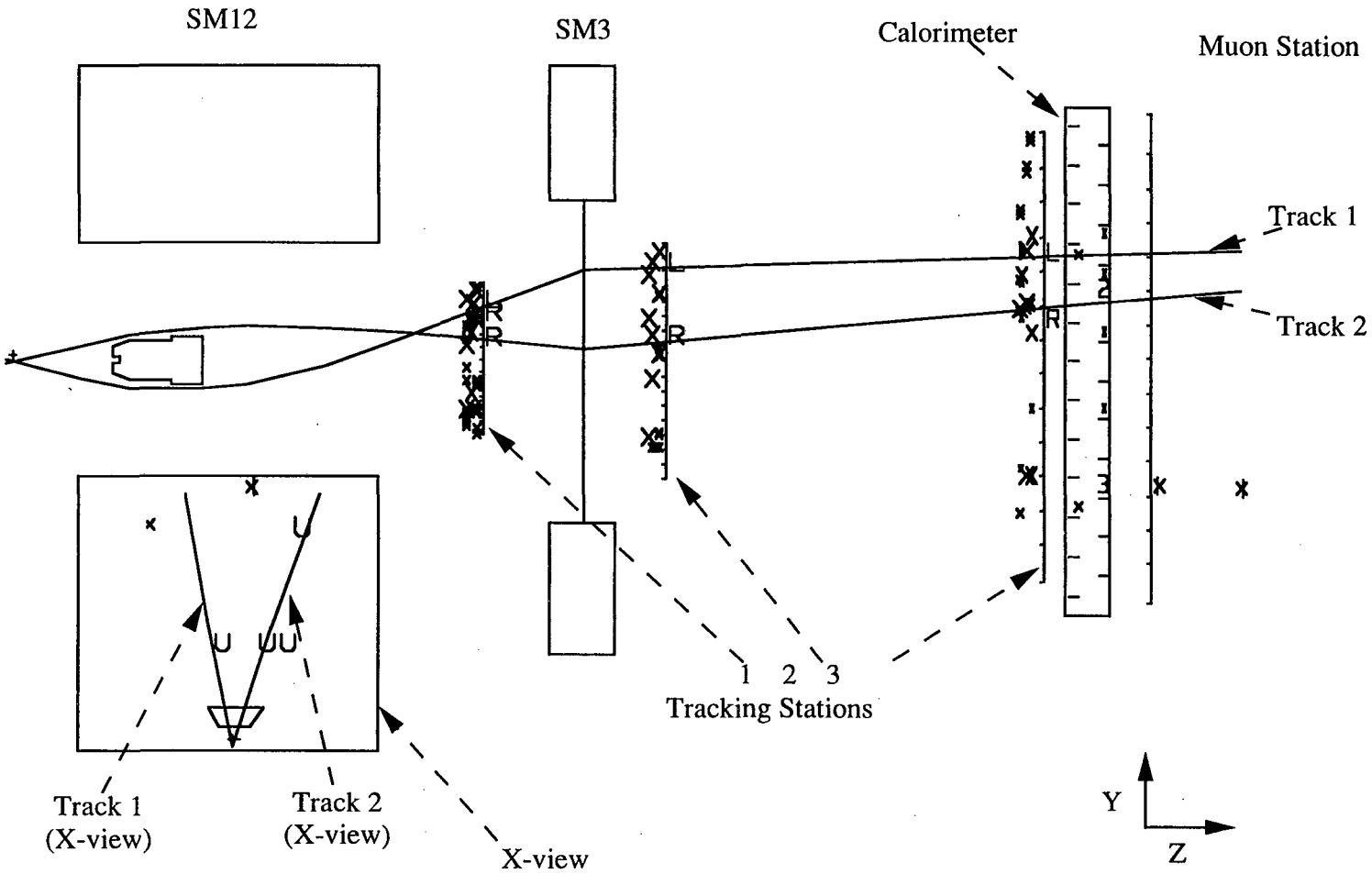

Figure 3.1: Example of a reconstructed dihadron event.

3.1.2 SSD Reconstruction

After the downstream tracking, all tracks in the SSD (Silicon Strip Detector) were reconstructed.[4] In each of the SSD arms, the four Y-planes were first used to find potential tracks.[5] In each Y-plane, each hit was used as a pivot to form windows for the other planes. The first window was created using the location of the pivot (the hit location) as well as the Y and Z coordinates of the target. The window was projected to another Y-plane and each hit in the window for that plane was selected to form potential tracks. Once two hits in two planes had been selected, the final two planes then were used to complete the fit to a straight track in the Y-Z plane. The last two planes only contributed the hit nearest to the line formed by the hits in the first two planes. The preliminary Y-tracks were then used to mask hit-windows in the U and V planes (used to form the X-view). Hits within the windows were then combined to find the best track using only the UV information (same algorithm as that for the Y-planes). Finally the complete set of hits were combined such that a full three-dimensional reconstruction could be formed. If the $\frac{\chi^2}{\text{degrees of freedom}}$ of a track was improved by eliminating one hit, that hit was removed and the old track was replaced with the new one.

To eliminate unnecessary tracks, the SSD tracks were compared to downstream tracks.[6] Each downstream track might mask[7] any SSD track that fell within the Y-Z angle matching window of $\pm 1.5\ mr$. Each opposite-sign pair of masked SSD tracks was then used to form a vertex. The vertexing required that each SSD track of a pair candidate be adjusted such that each originated from a common vertex. The final iterations were determined by finding the configuration that minimized the $\frac{\chi^2}{\text{degrees of freedom}}$ for the set of hits chosen by the track reconstruction.

The most important variable for enhancing the fraction of true downstream decays was the impact parameter of the track determined before the vertex constraint was imposed. This will be discussed in more detail in Section 3.2.3.

Figure 3.2 shows the SSD reconstruction for the same event as shown in Figure 3.1. Note that with masking, only tracks associated with the downstream tracks are

have hodoscope hits associated with it.

[4] See Section 2.2.3 for details of the SSD configuration.

[5] In the final passes over the data, the downstream tracks were used to mask the SSD hits, the track-finding algorithm was essentially the same.

[6] Most particles with tracks reconstructed in the SSD did not propagate through the entire spectrometer.

[7] The term 'mask' implies an association.

reconstructed. Figures 3.3 and 3.4 show expanded views of the upper and lower SSD arms for the same event. Note that, with each SSD view, the raw SSD hits are shown. As a result, the rotated U and V planes display their hits slightly above or below the two dimensional projection of the track. In Figures 3.2, 3.3, and 3.4 there are clearly other target tracks that have been ignored by the tracker because they fall outside the masking windows. This limits the reconstruction of unnecessary tracks, thus speeding up the processing and more importantly, lessening the opportunity of spurious hits confusing the tracker.

To verify that the Downstream-Tracker was masking the correct hits (and thus tracks) in the SSD, a study of events in which there was only one track in either SSD arm was performed. The single track in the SSD arm could then be compared with the downstream track as it was traced through the silicon. Figure 3.5 shows the distance between the SSD hit used in the reconstructed SSD track and the downstream track traced to that plane. The planes compared here are the Y-planes for the lower arm. Figure 3.6 shows the same quantity but for the U and V planes in the upper arm.[8] Figure 3.7 shows the angular difference between the downstream and SSD tracks in both X and Y for both arms. In addition to confirming the alignment and traceback, these distributions could also be used to determine the hit-windows for each plane and angle- matching windows for each coordinate.

3.2 Event Selection

3.2.1 Pass One

The first pass of data processing served primarily to convert the raw data into reconstructed particle trajectories through both the downstream spectrometer and the SSD. Track reconstruction coupled with loose vertexing requirements in the SSD and a cut on the reconstructed invariant mass provided a four to one data reduction. The original raw data and the newly reconstructed downstream track information was stored as part of the Data Summary Tapes (DST's) which were generated as output of the first pass.

For each event, each opposite-sign pair of tracks was reconstructed as though they decayed from a single parent through each of the decay modes, $D^0 \to K\pi$, $D^0 \to \mu\mu$, $D^0 \to \mu e$, or $D^0 \to ee$.[9] The resulting invariant mass had to fall within a 500 MeV/c^2

[8] Of course, each arm has a complete set of Y, U, and V planes.

[9] The sign of the track is determined by the bend magnet.

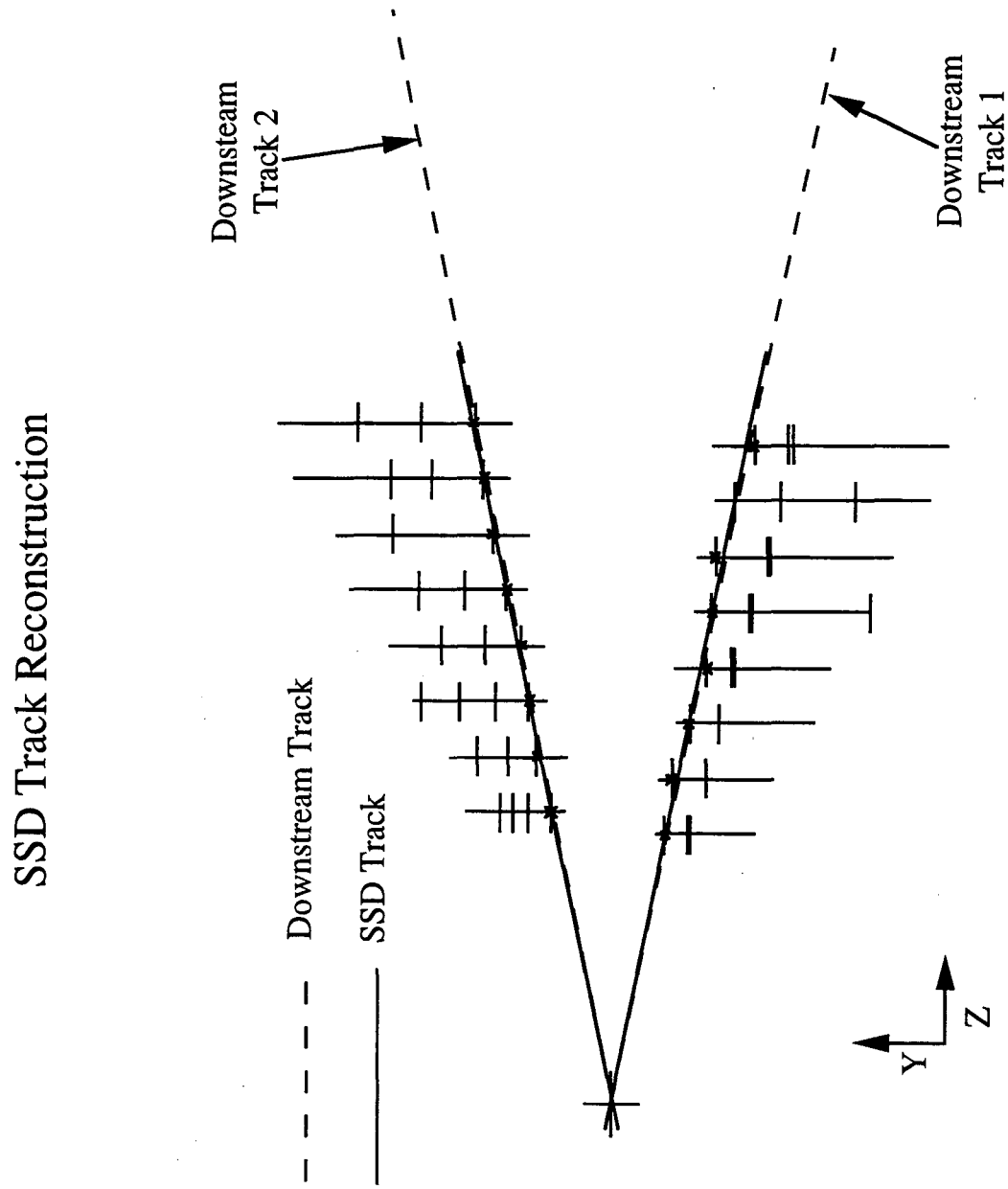

Figure 3.2: SSD reconstruction of event displayed in Figure 3.1. U and V planes are rotated; thus U,V hits appear off-set.

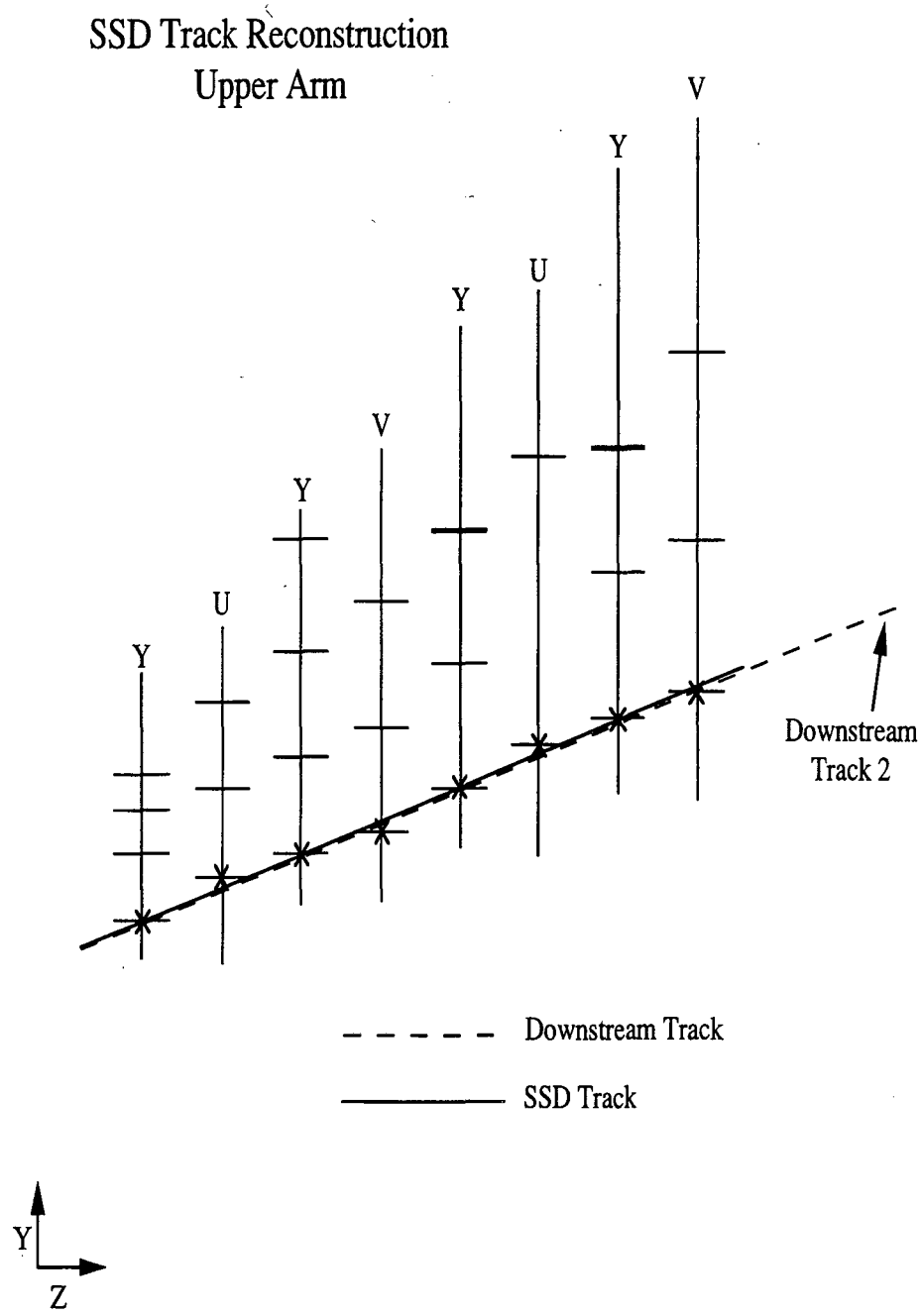

Figure 3.3: Expanded view of upper SSD arm for event displayed in Figure 3.1. U and V planes are rotated; thus U,V hits appear off-set.

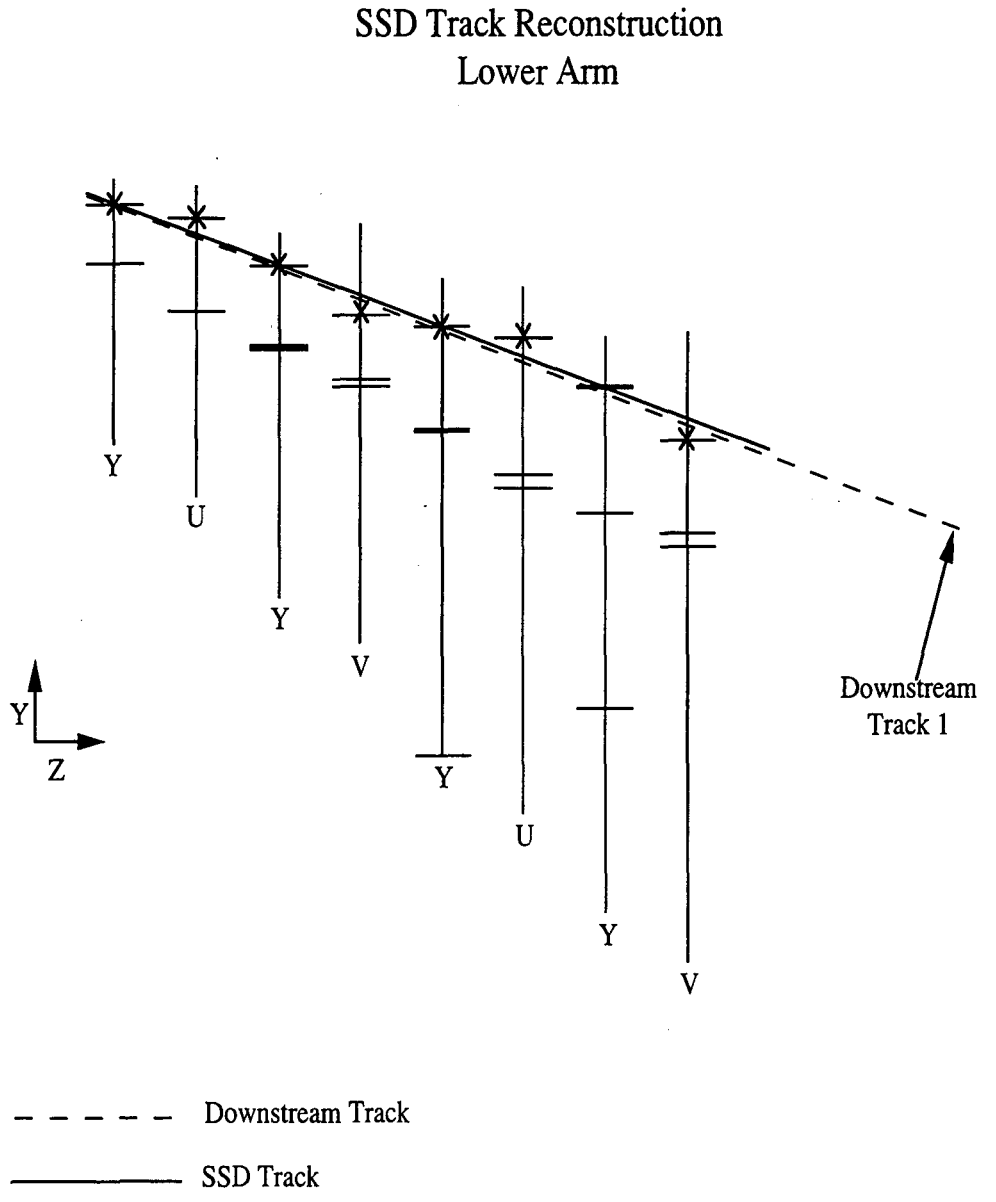

Figure 3.4: Expanded view of lower SSD arm for event displayed in Figure 3.1. U and V planes are rotated; thus U,V hits appear off-set.

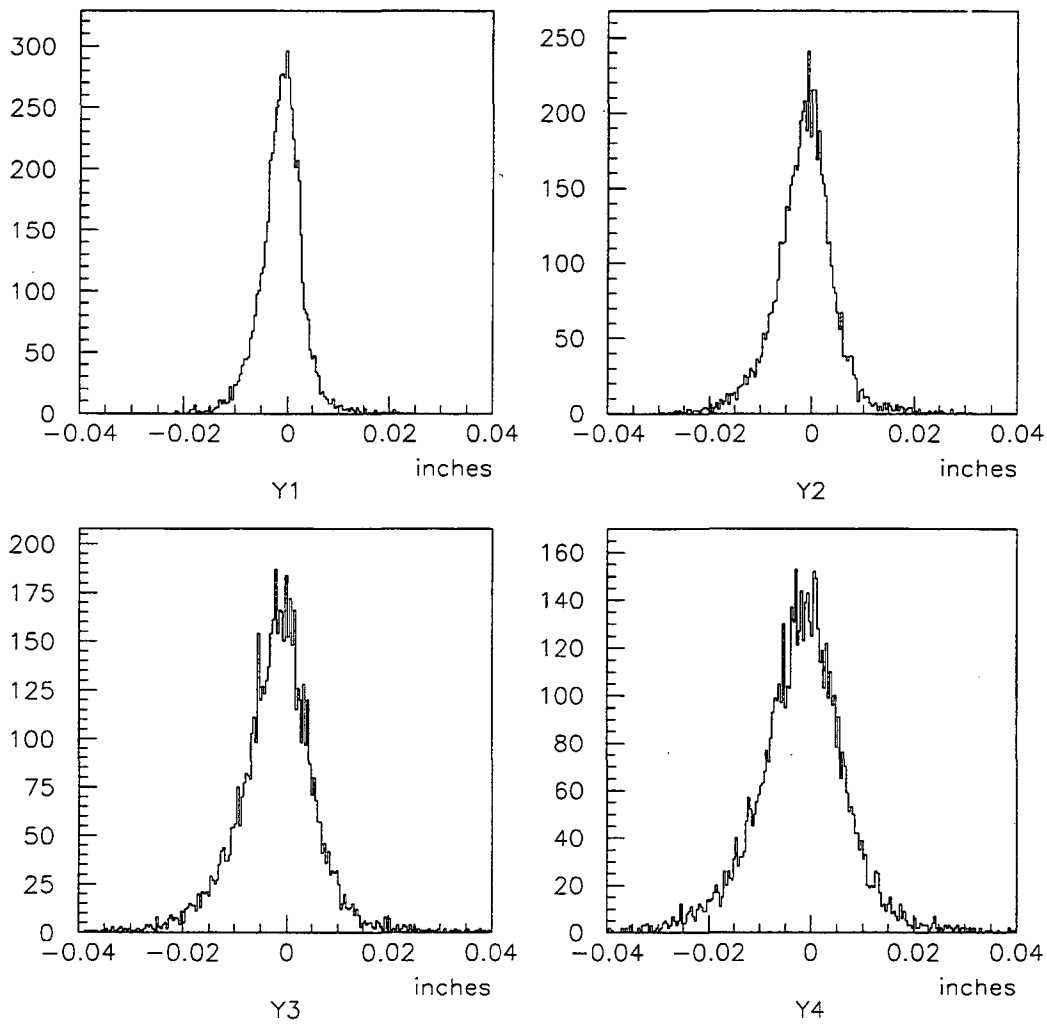

Figure 3.5: Distance between the downstream track and the associated SSD hit for the Y-planes in the lower SSD arm for events with only one SSD track in the arm.

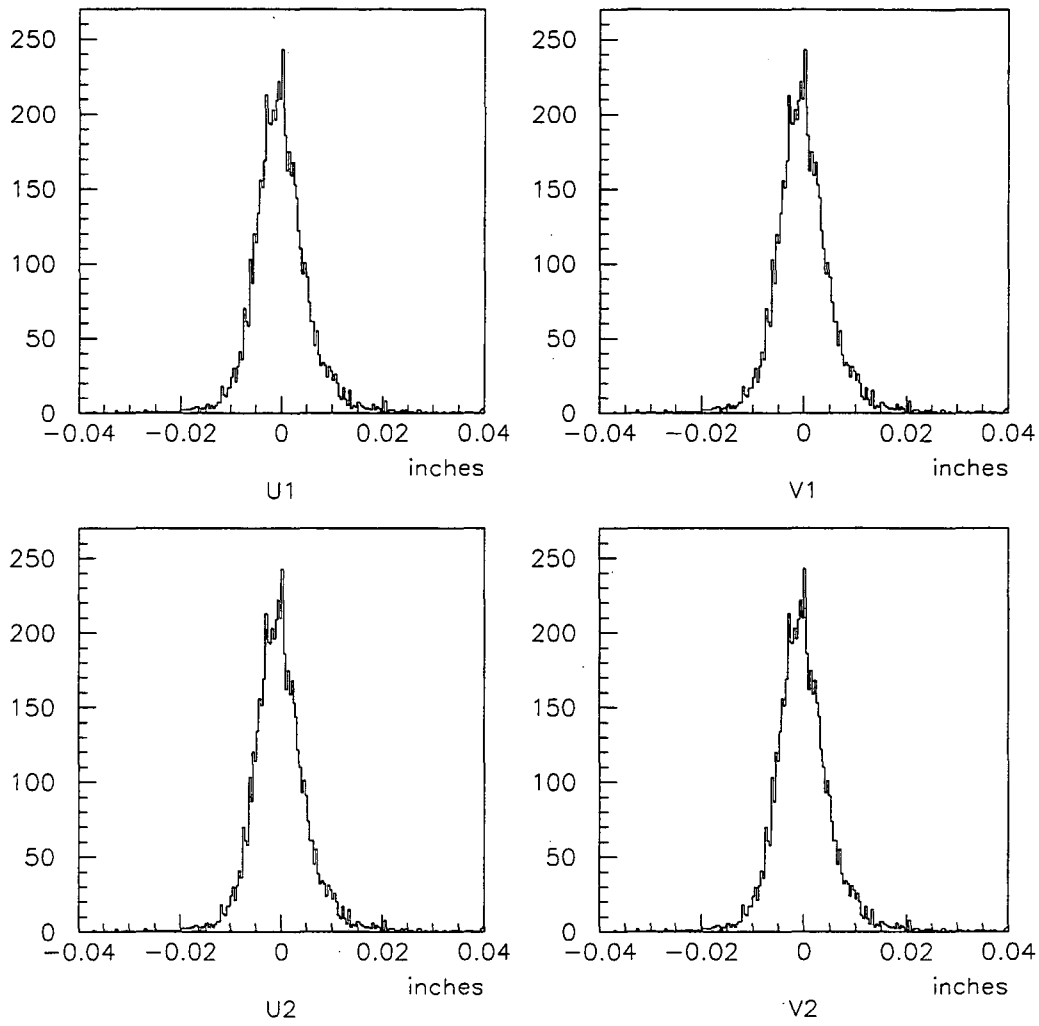

Figure 3.6: Distance between the downstream track and the associated SSD hit for the U and V planes in the upper SSD arm for events with only one SSD track in the arm.

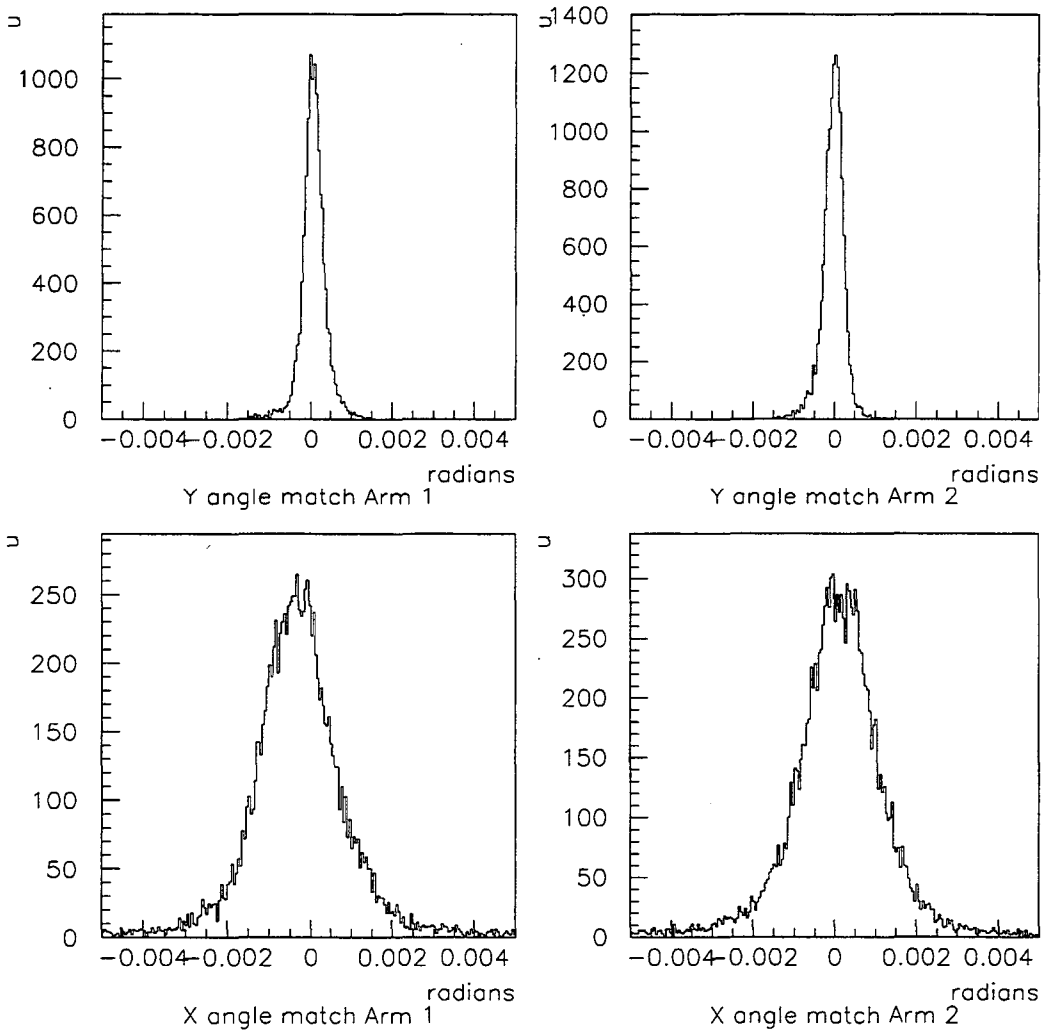

Figure 3.7: Y- and X-angle matching between downstream track and SSD track for both SSD arms for events with only one SSD track in either arm.

window extending from 1.65 GeV/c^2 to 2.15 GeV/c^2 for any of the decays. Finally, events were selected if they had at least one opposite-sign pair of tracks that formed a vertex with the Z-location outside a 0.2 *in* window centered on the target. In addition, a prescaled sample of all events with at least one opposite-sign vertex were included without a Z-cut, as were a prescaled sample of events where the two tracks forming the vertex had the same sign (like-sign events), again with no Z-cut.

3.2.2 Pass Two

The second pass analysis provided another factor of five reduction of the data set. The second pass utilized a tighter mass cut along with various tracking enhancements. The major contribution to the tracking upgrade involved the SSD. A new alignment of the detector, coupled with masking of acceptable SSD hits in Y with the downstream tracks, reduced the number of unwanted SSD tracks and sped the processing.

In an average event, more than one vertex was formed by SSD tracks that masked in the Y dimension to the downstream tracks. To help select the correct vertex, additional matching in the X-angle was then applied. A list of vertices was formed with one track in each opposite arm of the SSD masking the two opposite signed tracks in the downstream spectrometer. Vertices in an event were categorized by the number of tracks that matched in the X-angle (i.e. 2, 1, or 0). Only vertices that fell in the best matching category were used. Vertices having only one matching track were used only if no vertices had two matching tracks. Relatively few (2%) vertices had no X-matching tracks. In order to maximize the efficiency for accepting a vertex resulting from the decay of a D^0 , we use a neural net[10] to compare the various vertices in an event. The Net used three variables, the impact parameter of each SSD track used in the vertex and the position of the vertex in the z-coordinate. All subsequent characterization of an event used the vertex with the highest probability of being a D^0 decay. In addition to the tighter masking, an overall probability cut was applied. The overall probability was determined by the neural net (see Appendix A for details).

Particle identification had little to do with the *Pass Two* event reduction. Each event was reconstructed under the $D^0 \to K\pi$, $D^0 \to \mu e$, $D^0 \to \mu\mu$, and $D^0 \to ee$ hypothesis. The invariant mass of the reconstructed event was required to fall within a 200 MeV/c^2

[10]The neural net, though adequate for eliminating much of the background, was not useful for final signal to noise enhancement and thus not used for *Pass 3*. See Appendix A for details.

window about the D^0 mass (1.864 GeV/c^2 [7]) for any of the modes.

3.2.3 Pass Three

The third pass incorporated all the enhancements used for the final event selection and served to further reduce the data set. *Pass Three* included:

- New Vertex Selection
- Event Categorization
- Final event selection

Vertex Selection

In the final pass, a new vertex selection criterion was used to select a single vertex from the multiple vertices event. Multiple vertices resulted either from multiple downstream tracks or multiple SSD tracks masking to a downstream track. The vertexing algorithm has been described in Section 3.1.2. Each vertex consisted of two oppositely charged downstream tracks that each masked to an SSD track. The quality of a vertex was evaluated using nine parameters. The value associated with each parameter for each vertex in a single event was assigned to a probability and the overall vertex probability was simply the product of the nine probabilities.

The nine parameters used to define the quality of a vertex were:

- Y-angle matching between each downstream track and its SSD track. (*2 parameters*)
- X-angle matching between each downstream track and its SSD track. (*2 parameters*)
- $\frac{\chi^2}{\text{degrees of freedom}}$ for each SSD track. (*2 parameters*)
- $\frac{\chi^2}{\text{degrees of freedom}}$ formed with the physical distance between the associated SSD hit and the projected track at each SSD plane. (*2 parameters*)
- $\frac{\chi^2}{\text{degrees of freedom}}$ for the SSD vertex. (*1 parameter*)

Each angle matching parameter was assigned a probability assuming it was characterized by a Gaussian distribution. The parameters of the Gaussian were determined by fitting a Gaussian to each distribution using events where there was only one SSD track in either

SSD Plane	$\sigma_j(in \times 10^{-3})$ Arm 1	$\sigma_j(in \times 10^{-3})$ Arm 2
Y1	3.522	5.687
U1	4.584	4.604
Y2	4.829	6.923
V1	5.956	5.914
Y3	6.485	7.926
U2	7.255	7.237
Y4	7.740	8.964
V2	8.511	8.271

Table 3.1: Standard deviations used to form χ^2 in Equation 3.3.

arm (see Figure 3.7). The standard deviations (σ) associated with the distributions for X and Y angle matching were 9.5×10^{-1} mr and 2.5×10^{-1} mr respectively. In addition, there was a slight offset of the mean of the distribution, < 0.4 σ, for the X-angle matching. This offset was also incorporated.

The number of degrees of freedom associated with the χ^2 of each SSD track was simply the number of hits used to form the track minus two. For the vertex, it was the total number of hits minus two for each track and three for the vertex (total number of hits minus 7). The χ^2 formed with the SSD hits and the projected downstream track is

$$\chi^2 = \sum_j \frac{(Y_{jdownstream} - Y_{jSSD})^2}{\sigma_j^2} \tag{3.3}$$

where j is summed over all planes used to form the track. The σ_j were based on the residuals of the single-track data set discussed in Section 3.1.2 and are listed in Table 3.1. Figures 3.5 and 3.6 show the distributions of the difference between the SSD hit and the projected downstream track at each SSD plane. Figure 3.2.3 show the χ^2 distributions associated with Equation 3.3 for each SSD arm.

Final Event Selection

The final pass selected events that were most likely D^0 decays. A fully reconstructed event consisted of one opposite-sign pair of SSD tracks that masked to one pair of downstream tracks.

The most effective variable used to enhance the $D^0 \to K\pi$ yield was the impact

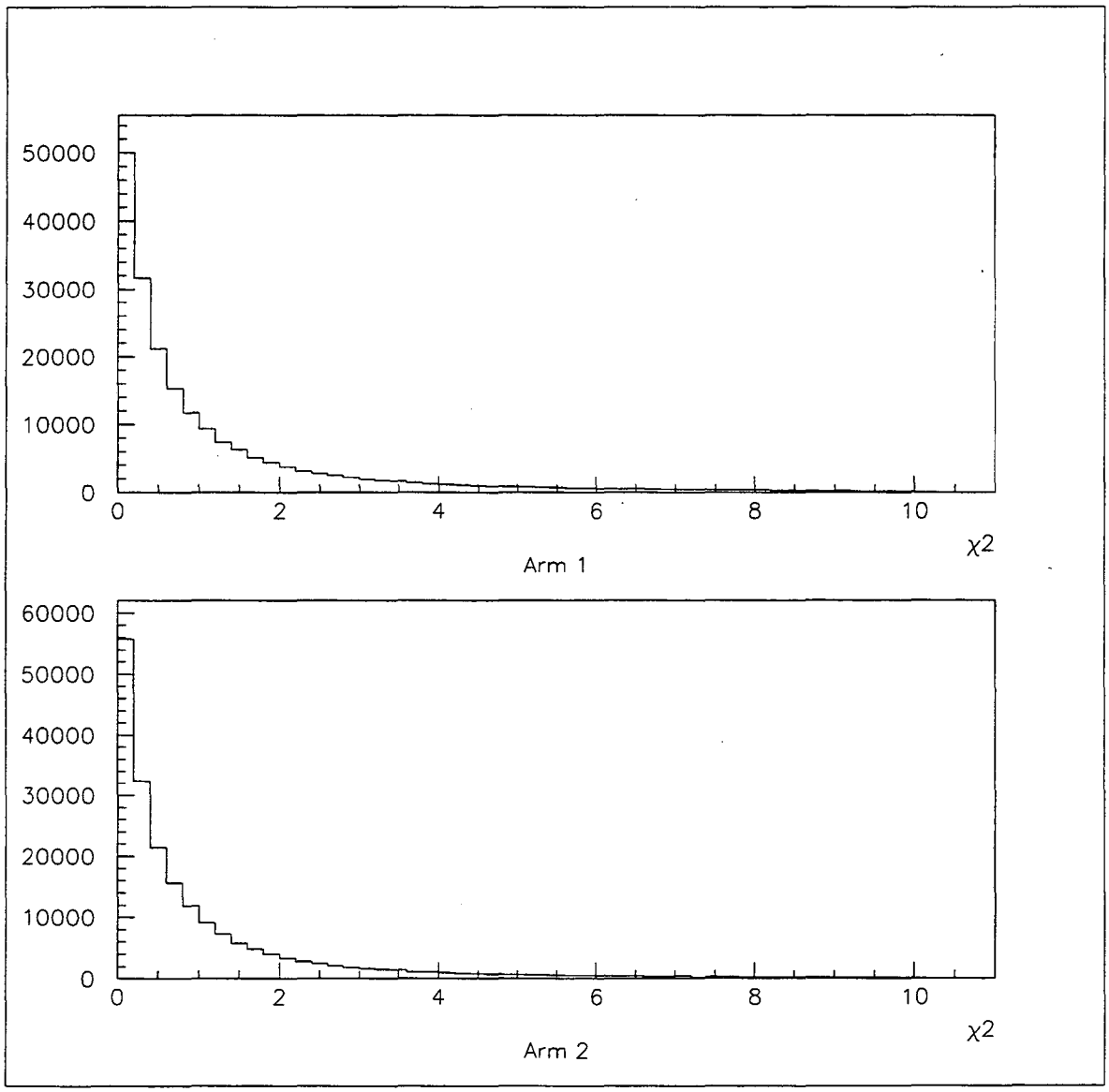

Figure 3.8: χ^2 distributions associated with Equation 3.3 for each SSD arm.

parameter of each SSD track with respect to the target in the y-coordinate before the vertex-constrained fit. The incorrectly reconstructed events often contained at least one track that came from an interaction in the target with a small impact parameter. By eliminating events in which either track projected to the target, the sensitivity to true downstream decays was enhanced. Using the track before it has been constrained to a vertex prevents the other track in the vertex from influencing the impact parameter of the first track.

To further enhance the accuracy of the reconstruction, events were excluded if more than four SSD tracks masked to either downstream track or more than ten vertices were reconstructed. In addition, a variable was formed by dividing the distance of the vertex from the target center by the quantity $\gamma\beta c\tau$, the average decay distance of the D^0 assumed to be associated with the decay. Thus $\frac{decay\ distance}{\gamma\beta c\tau}$ can be termed a cut on the number of average decay distance, *lifetime significance*. The final combined set of cuts was determined by adjusting each of the two variables for each decay mode such that best limit could be extracted from each data set. The limit calculation along with the final results are presented in Chapter 5.

3.3 Calorimeter Calibration

The Calorimeter[11] was calibrated using a large sample of events consisting of isolated, charged particles that were not muons. The calorimeter was optimized by matching the particle's momentum, measured by the spectrometer, to its energy, as determined by the calorimeter. The calibration procedure is as follows: Events used for calibration came from the same data set used in the analysis; no special trigger was required. A selected event consisted of any particle trajectory which had no second charged track within a seven module vertical window centered on the module where the particle hit at the electromagnetic and hadronic sections of the calorimeter. In addition, the particle had to fall completely within the fiducial region of the calorimeter; the fiducial region did not include the gap ($\sim 3.8\ in$) that separates the left and right sides of the calorimeter. Muons were excluded from the calibration data set by requiring the muon station, at the rear of the spectrometer, to register zero hits associated with the track. Once a track was selected, the unprocessed calorimeter ADC values of the modules associated with the track were written to a calibration DST along with various pertinent tracking parameters. The ADC required a quadratic mapping

[11] Section 2.2.7 includes a detailed description of the calorimeter.

to recover the energy deposited in that module. With N_{nk} = ADC count in n^{th} module of the k^{th} event, the energy in a module given by $Q_n = (a_n \times N_{nk}^2 + b_n \times N_{nk} + c_n)$, where a_n, b_n, and c_n are constants to be determined. Let **t** include all the calibration parameters **a**, **b**, **c**:

$$t_i = a_{i\{i=1,\ldots,N_{adc}\}} \tag{3.4}$$

$$t_j = b_{j\{j=N_{adc},\ldots,2\times N_{adc}\}} \tag{3.5}$$

$$t_l = c_{l\{l=2\times N_{adc},\ldots,3\times N_{adc}\}} \tag{3.6}$$

where N_{adc} = number of modules. Also, let **f** be defined as follows:

$$f_{ik} = N^2_{ik\{i=1,\ldots,N_{adc}\}} \tag{3.7}$$

$$f_{jk} = N_{jk\{j=N_{adc},\ldots,2\times N_{adc}\}} \tag{3.8}$$

$$f_{lk} = 1_{\{l=2\times N_{adc},\ldots,3\times N_{adc}\}} \tag{3.9}$$

where, as above, k represents the event.

The energy of a track, $E_k = \sum_j Q_j = \sum_j((t_j + \delta_j) \times f_{jk})$ where δ_j is the variation of the initial calibration parameters and j is summed over modules the track traverses plus its nearest neighbors. For example, if the i^{th} module was used in the energy sum, then j would sum over $i, i + N_{adc}$, and $i + 2 \times N_{adc}$ for that module.

To remove variation in the signal due to particles hitting the module at different X-positions, a small fiducial region ($\sim 12\ in$) was initially defined in X for each side of the calorimeter; the X-dependence was later incorporated using the entire fiducial region.

To account for noise that might result from contamination due to neutrals, or to the electronics between the scintillator and the ADC, an ADC count distribution for modules with no track traversing that module or any module nearby was used; each module thus had a noise histogram associated with it. As each raw ADC count was read in during the calibration a random number was generated based on the noise distribution associated with that module. If the noise count was less than or equal to the raw ADC count, the noise was converted into an effective energy and then subtracted from the energy that mapped to the raw ADC count (necessary to account for the quadratic nature of the ADC to energy mapping). If the new, noise subtracted, energy was above the hardware pedestal of the module, the noise subtracted energy was converted back to a noise subtracted ADC count that can be used for the calibration; otherwise the ADC count was set to zero. If the random

noise count generated was larger than the raw ADC count, a new random noise count was generated.

The calibration consisted of a minimization of the quantity $\chi^2 = \sum_k \frac{(P_k - E_k)^2}{P_k}$; where P_k is the momentum of the track as measured by the spectrometer, and k is summed over all events used in the calibration (each event consists of one isolated track). Furthermore, a module could only contribute to the energy if it had a noise subtracted ADC count that was greater than the hardware pedestal for that module. Setting the derivative of χ^2 with respect to the variables δ_i equal to zero yields the following:

$$1/2 \times \frac{\partial \chi^2}{\partial \delta_i} = \sum_k \frac{(P_k - E_k)}{P_k} \frac{\partial E_k}{\partial \delta_i} \tag{3.10}$$

$$= \sum_k \frac{P_k - \sum_j (t_j + \delta_j) \times f_{jk}}{P_k} \times f_{ik} \tag{3.11}$$

$$= \sum_k f_{ik} - \sum_j \sum_k \frac{t_j f_{jk} f_{ik}}{P_k} - \sum_j \sum_k \frac{\delta_j f_{ik} f_{jk}}{P_k} \tag{3.12}$$

$$= 0 \tag{3.13}$$

Now rewriting the final equation using the following definitions:

$$h_i = \sum_j \sum_k \frac{t_j f_{jk} f_{ik}}{P_k}; \quad b_i = \sum_k f_{ik}; \quad F_{ji} = \sum_k \frac{f_{ik} f_{jk}}{P_k};$$

gives

$$b_i - h_i = \sum_j F_{ji} \delta_j$$

which can be rewritten in vector notation, $\mathbf{b} - \mathbf{h} = \mathbf{F} \cdot \boldsymbol{\delta}$. Thus the problem is reduced to solving for $\boldsymbol{\delta}$; with **b**, **h**, and **F** calculated over many events. To account for the X-dependence of the scintillator response over either side of the calorimeter, a second calibration was done. Each side of the calorimeter was divided into ten bins whose X-boundaries are chosen to allow for approximately equal statistics in each bin; in effect, each module was further divided into ten sub modules. In this case, $Q_j = g_j \times (a_j \times N_{jk}^2 + b_j \times N_{jk} + c_j)$ where **g** is an overall gain that incorporates the X-dependence and j indicates the new effective module that includes the X-slice the track traverses at the original, un-sliced, module. $j = \{1, \ldots, N_{adc}\}$ for the first X-bin, $j = \{N_{adc} + 1, ..., 2 \times N_{adc}\}$ for the second and so on; keep in mind that the **a**, **b**, and **c** vectors do not vary in X and thus $a_j = a_j + N_{adc}$, $b_j = b_j + N_{adc}$, and $c_j = c_j + N_{adc}$. The only modification to the above formalism is that

the **a**, **b**, and **c** vectors are fixed and **g** is varied. Thus $f_{jk} = (a_j \times N_{jk}^2 + b_j \times N_{jk} + c_j)$ and $\mathbf{t} = \mathbf{g}$. Once **g** was found, the X-dependence of a module associated with a particle was determined by first finding the X-bin that was traversed by the particle at that module. Then a piecewise interpolation between the g_j of that X-bin and its nearest neighbor results in the overall multiplicative factor g_n. The energy associated with the k^{th} track $= E_k = \sum_n Q_{nk} = \sum_n g_n \times (a_n \times N_{nk}^2 + b_n \times N_{nk} + c_n)$ where N_{nk} is the ADC count of the n^{th} module; n was summed over the modules that the track traversed and those nearby. The calibration was divided into three passes. *Pass One* set the starting values for the **a**, **b**, **c**, and **g** vectors. The calibration parameters determined in *Pass One* were then used to select a subset of the original calibration data set consisting of electrons. A particle was identified as an electron if the fraction of energy deposited in the electromagnetic section of the calorimeter was greater than 90% of the total energy deposited along the particle trajectory in the calorimeter ($Emfrac \geq 0.9$). In addition, it was further required that the total energy deposited in the calorimeter be at least 50% of the measured energy as determined by the spectrometer (E/P $\geq$ 0.5). *Pass Two* used the electron data set and only the calibration parameters in the electromagnetic segment were allowed to vary. In effect, *Pass Two* was a separate calibration of the electromagnetic section. *Pass Three* then used the entire data set (which consisted almost exclusively of hadrons) to do a separate calibration of the hadronic section. In *Pass Three*, both the electromagnetic and hadronic segments of the calorimeter were used for the energy calculation. However, only the parameters associated with the hadronic section were allowed to vary. In each pass the **a**, **b**, and **c** vectors were first determined and then the X-dependence (**g**) was found.

Calorimeter Survey File

With a complete calibration, the calibration parameters were written to a survey file. The a_i, b_i, and c_i were written for each ADC (148 ADC's $\times$ 3 = 440 parameters). In addition, to accommodate the X-dependence of each ADC, the gain parameters g_i were written for each X-slice of each ADC (148 ADC's $\times$ 5 slices = 740 parameters). The reconstruction used exactly the same algorithm as the calibration for assigning energy to each track. Furthermore, a series of E/P distributions were written to the calibration file for both electrons and hadrons. With both the width and mean of the E/P distribution dependent on the deposited energy, a separate mean and width were fit and recorded for

E/P survey values

	EM	EM	Had	Had
Energy (GeV)	Mean	σ	Mean	σ
18.25	1.082	.1530	1.1097	.1957
23.75	1.066	.1234	1.0850	.1695
29.25	1.049	.1001	1.0503	.1516
34.75	1.029	8.599×10^{-2}	1.0189	.1381
40.25	1.015	7.897×10^{-2}	1.0071	.1279
45.75	1.009	7.855×10^{-2}	1.0038	.1174
51.25	1.004	7.249×10^{-2}	1.0041	.1079
56.75	1.005	6.865×10^{-2}	1.0029	.1012
62.25	.9986	6.320×10^{-2}	1.0019	9.507×10^{-2}
67.75	.9968	6.178×10^{-2}	.9971	9.072×10^{-2}
73.25			.9951	8.924×10^{-2}
78.75			.9910	8.361×10^{-2}
84.25			.9898	8.016×10^{-2}
89.75			.9839	7.983×10^{-2}
95.25			.9831	7.731×10^{-2}
100.75			.9787	7.666×10^{-2}

Table 3.2: E/P survey parameters for the 900A running period.

each 5.5 GeV binned interval. The intervals both spanned the entire accepted energy range for hadrons or electrons in any of the decay modes studied. Table 3.2 shows the E/P survey parameters for the 900A data set. The hadrons were much more abundant and their yield extended to a higher energy range; as a result, so did the survey.

Figure 3.11 shows the E/P for electrons, including X-dependence. Figures 3.12 and 3.13 show the same for hadrons. Figures 3.9, and 3.10 show E/P distributions for a series of 5 GeV bins for electrons and hadrons respectively.

3.4 Particle Identification

3.4.1 The Calorimeter

Electrons and Hadrons were identified using the E789 Calorimeter.[12] The identification procedure required two steps: first, that the energy deposited in the calorimeter be assigned to a track, and secondly that the profile of the energy deposition in the calorimeter

[12]The details regarding deposited energy readout and calibration are included in Section 3.3.

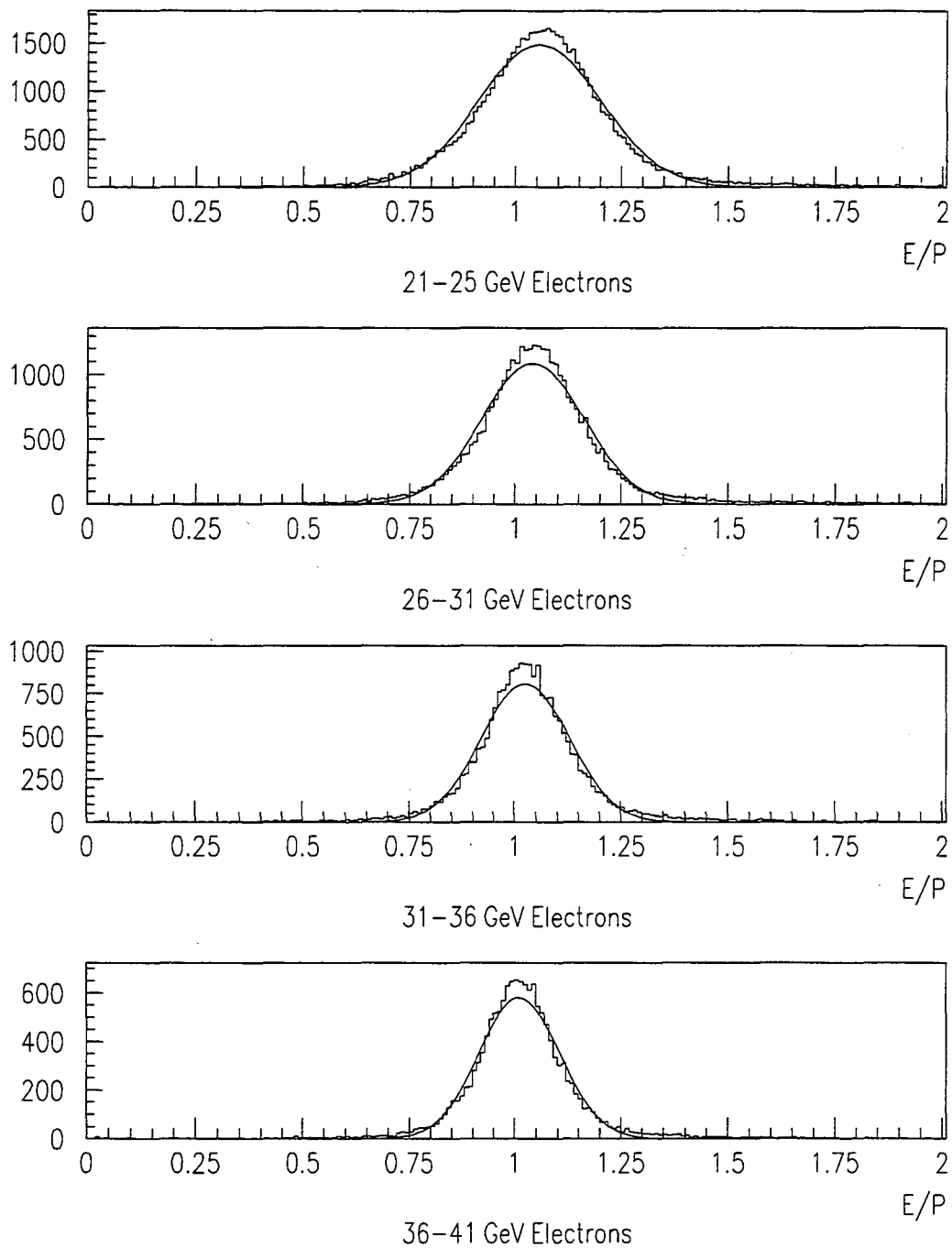

Figure 3.9: E/P distributions of electrons for a series of 5 GeV energy bins.

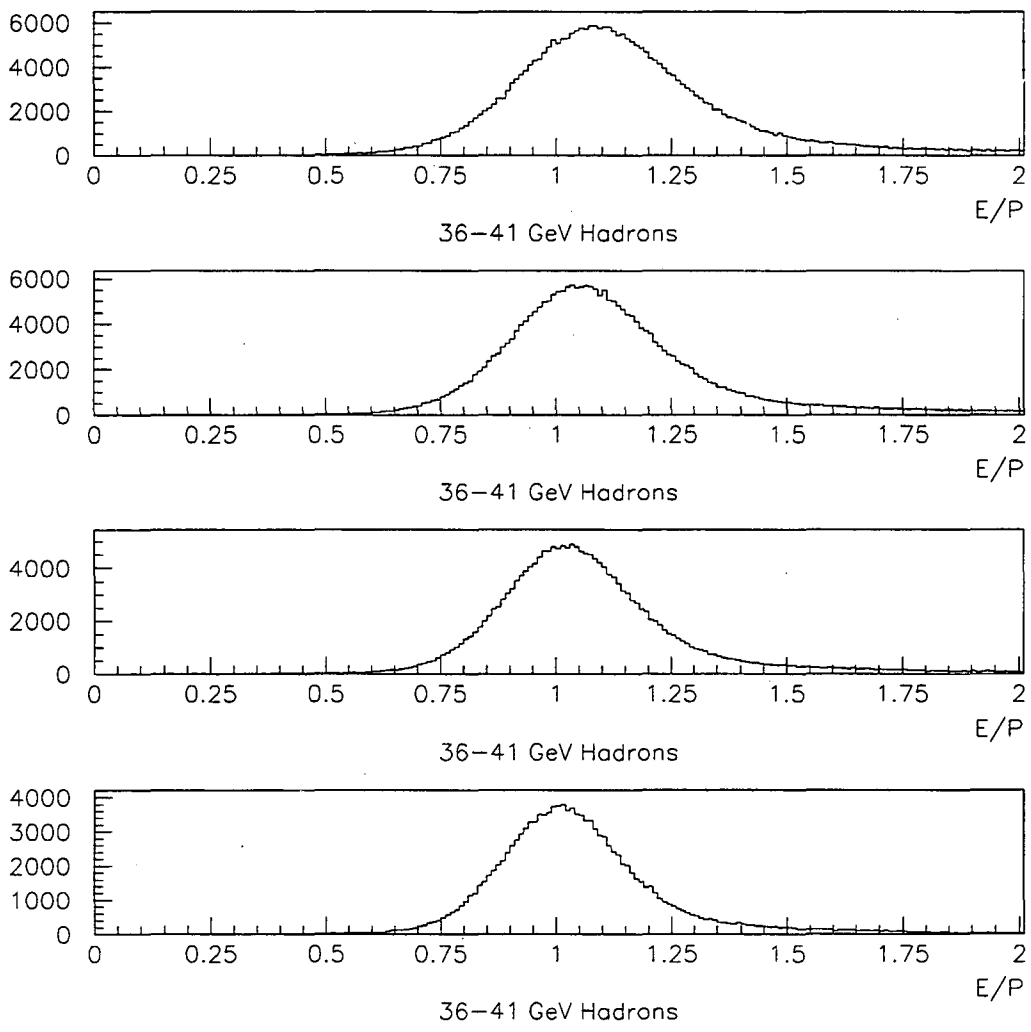

Figure 3.10: E/P distributions of hadrons for a series of 5 GeV energy bins.

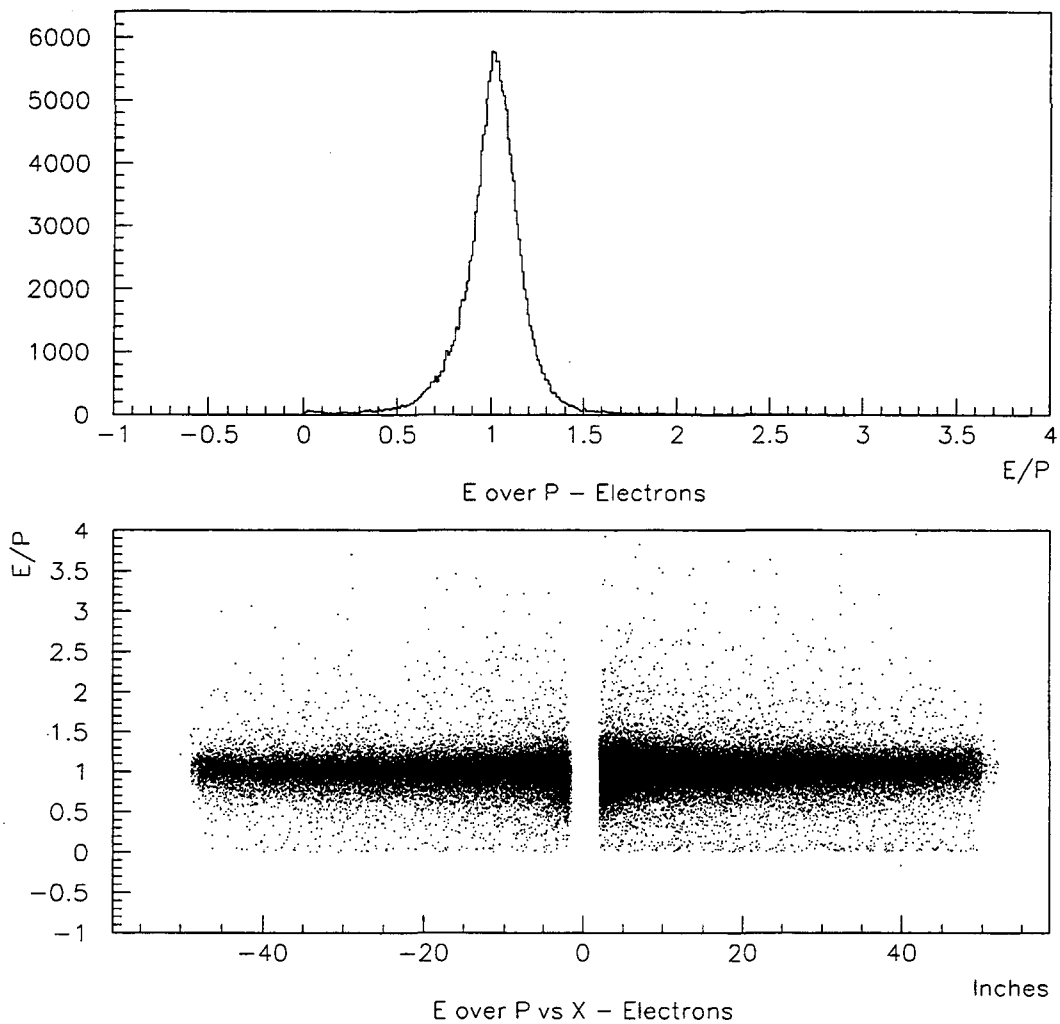

Figure 3.11: E/P distributions for electrons. The plot at the bottom shows the X-dependence of E/P.

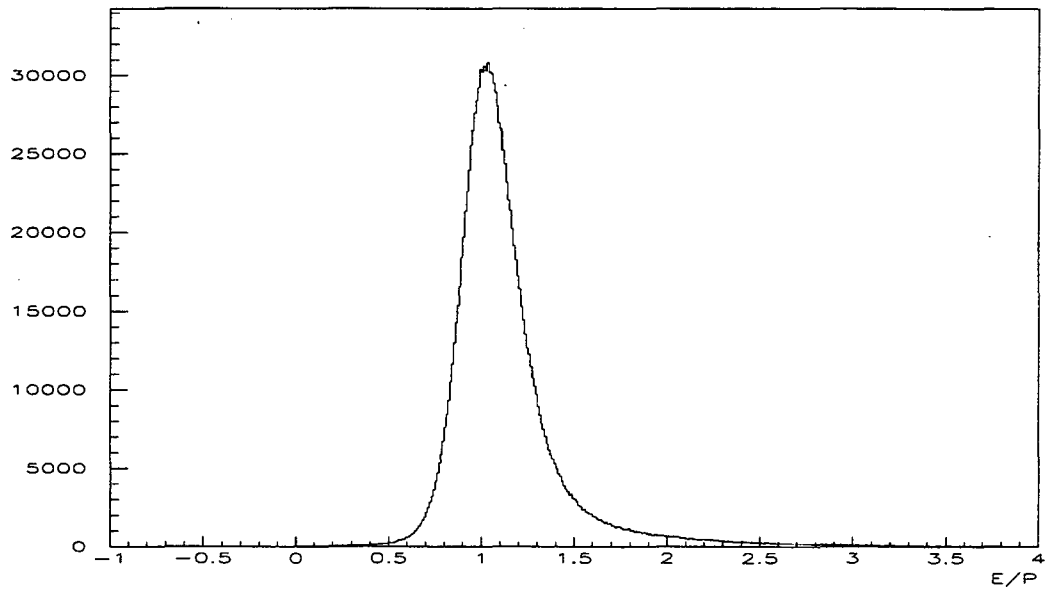

Figure 3.12: E/P distribution of hadrons.

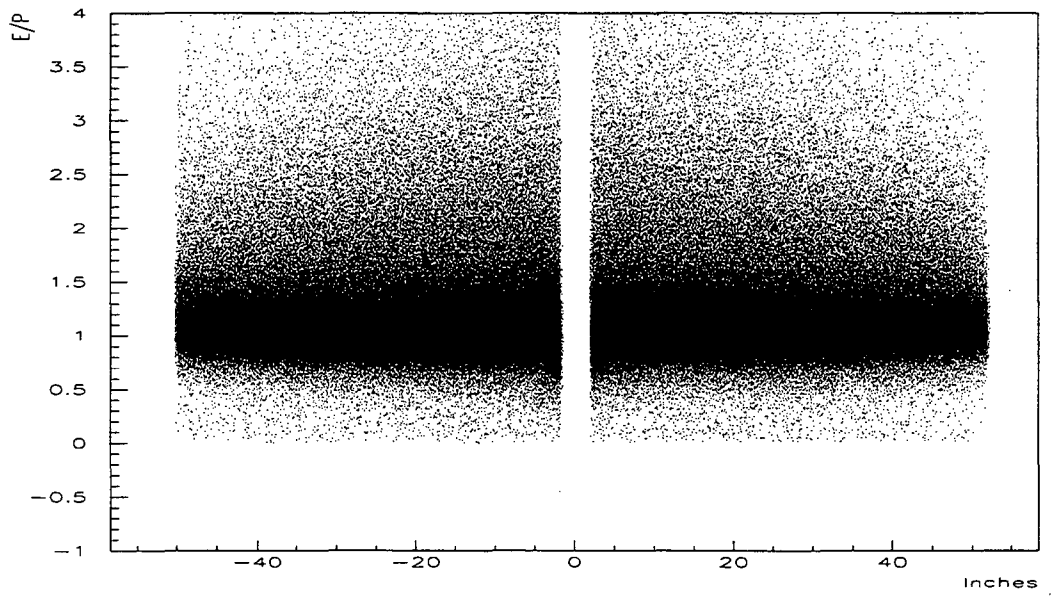

Figure 3.13: X-dependence of the E/P distribution for hadrons.

be used to label it as either a hadron or an electron.

Energy Assignment

For each event, the ADC count associated with each module of each layer of the calorimeter was converted to the amount of energy deposited in each module (see Section 3.3). The reconstructed particle trajectory was then projected through each layer of the calorimeter. At each layer, the energy associated with the module intersecting the trajectory and its nearest transverse neighbors were added to the track energy. The trajectory was complete in all three dimensions and thus allowed for the X-correction to be applied to the charge associated with each module.[13]

If the track had no other track within two transverse modules at each longitudinal layer, it was considered isolated and its total energy as well as the EM-fraction[14] were recorded with the track. The energy deposition transverse to the beam in the EM section was virtually limited to one module. As a result, if a second non-muon track was close enough such that each shared a common module used for charge summation, that module could be eliminated if either track was more than half a module away from the one in common. For example, a track passing through the lower half of an EM module would not need the upper adjacent module for charge summation; that module was not used if a second track passed anywhere above the middle of that adjacent module. In this case, the module traversed, and its lower adjacent neighbor would be used for charge summation. In the hadronic section, shower width was wider, an adjacent module was eliminated only if the track was in the lower 10% of the module. That is, in most cases, all three transverse modules were needed for the hadronic part of the charge summation. Figures 3.14 and 3.15 show the fraction of energy deposited in the adjacent module farthest away from the track. Each distribution only includes the energy deposited from tracks whose location in the adjacent module fits the criteria for exclusion, half a module away for the EM section and 9/10 of a module in the hadronic.

[13]The geometry of the calorimeter was such that the output of a module depended on the track's location in the module in the X-dimension. The details are discussed the Section 3.3.

[14]The EM-fraction is the fraction of energy deposited in the electromagnetic portion of the calorimeter divided by the total deposited energy. See Section 3.3

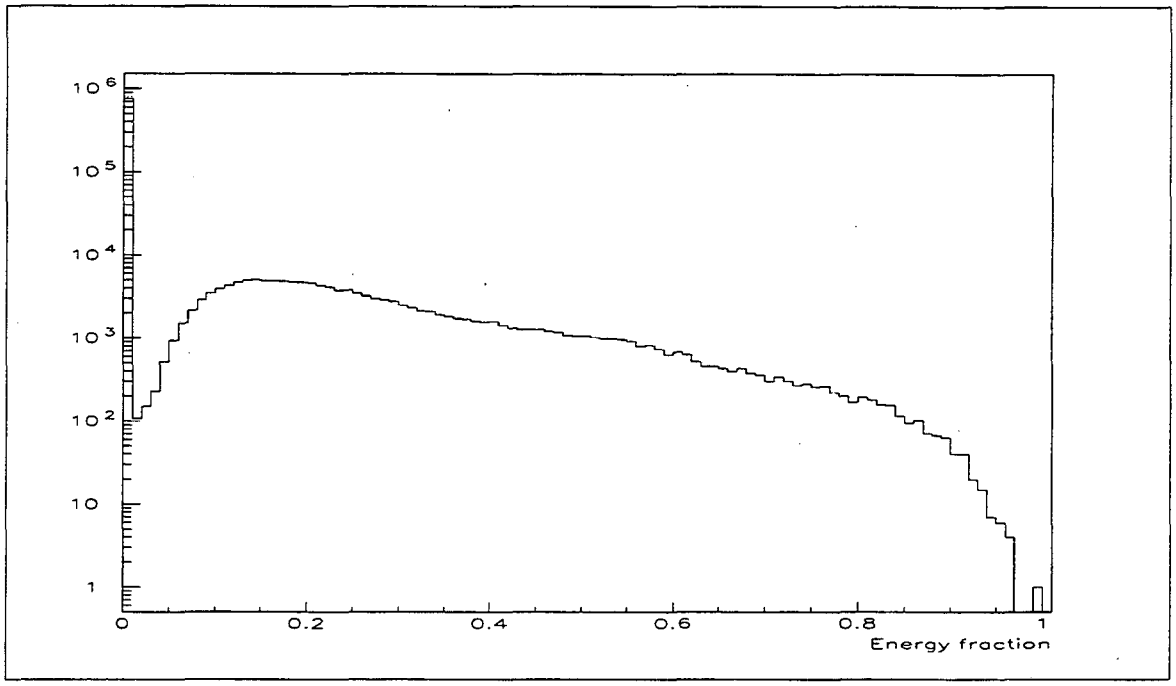

Figure 3.14: Fraction of total energy deposited in the farthest adjacent EM module.

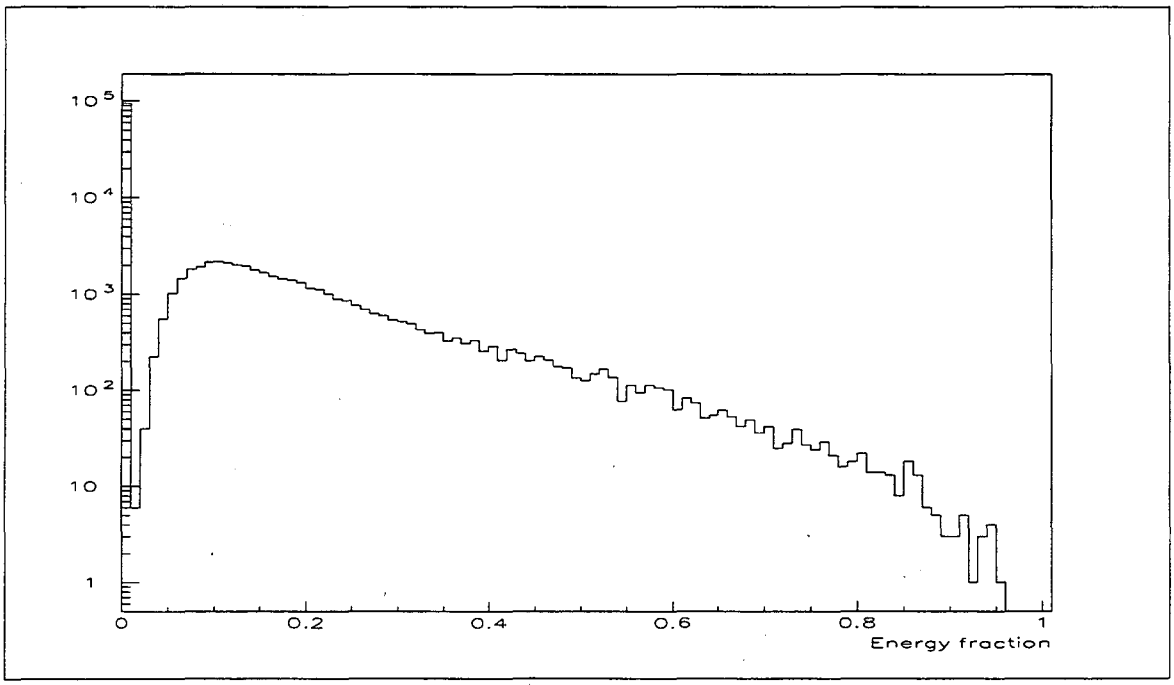

Figure 3.15: Fraction of total energy deposited in the farthest adjacent hadronic module.

3.4.2 Electron, Hadron identification

Once an event had passed all the requirements for isolating potential D^0 decays (see Section 3.2 for details), the tracks were identified as electrons, hadrons, or muons. The electron/hadron identification was done using the calorimeter. For an isolated track, the particle associated with the track was labeled as electron if the fraction of energy in the EM section divided by the total deposited energy (*EMfrac*) was ≥ 0.95. Furthermore, the total deposited energy divided by the momentum determined by the spectrometer, E/P, was required to be within 2.58 standard deviations (σ) from the mean of the E/P distribution associated with the appropriate energy bin.[15] For hadrons, the *EMfrac* was required to be below 0.7 and the 2.58-σ cut was the same.[16] Figure 3.4.2 shows *EMfrac* as a function of the X-position.

Overlap

If two non-muon tracks shared at least one module, as described in Section 3.4.1, they could often be identified using the energy deposition in each section of the calorimeter separately (EM vs. Had). If two electrons overlaped (very rare) they would both pass the *EMfrac* cut for electrons separately and the E/P requirement was waived. The same was true for overlapping hadrons (99% of all raw tracks were hadrons.). If one or both tracks failed either cut, each track was checked to see if it was possibly an electron. This was done by comparing the energy deposited in just the EM segment to the total momentum (E_{em}/P). Again the mean had to fall within $\pm 2.58\ \sigma$. The hadronic segment could have been compared as well but the E/P distributions were much wider than the EM distributions and thus were not as useful. In addition, narrow shower width in the EM section made energy matching, in that section, more reliable. Recall the calorimeter was only used to identify and distinguish electrons from hadrons. If the first track did not match as an electron but the second track did, the first track was labeled a hadron.

3.4.3 Muon Identification

Muon identification depended primarily on the Muon Station (Station 4, see Section 2). A track was projected to the Muon Station and each plane was checked to see

[15] In Section 3.3 the E/P characterization as a function of energy is discussed.

[16] Of course the E/P distributions were different in mean, σ, and energy dependence. This is taken into account and described in Section 3.3.

if there were any hits in the momentum dependent hit-windows (see Section 4.3 for a detailed discussion of the hit-windows). For a track to be qualified as a muon candidate, both hodoscope planes and at least two proportional tube planes had to fire in the Muon station. The hodoscopes had a time resolution under one bucket. Requiring them to have hits dramatically reduced the number of out-of-time tracks. Furthermore, the trigger required both hodoscopes as did the trigger simulation. In addition to Station 4, the calorimeter could also be employed for muon identification. 99.99% of the muons under 100 GeV/c left less than 35% of their energy in the calorimeter. If a track passed the Station 4 hit criteria and had an E/P greater than 35%, it was tagged as ambiguous but still counted as a potential muon. The most likely mechanism for muons having high E/P is for them to overlap with a non-muon track in the calorimeter. To remove fake dimuon events from a non-muon overlapping with a muon in Station 4, an isolation requirement was applied. Each track in the reconstructed dimuon event had to have unique hodoscope hits in Station 4. In addition, no more than one Proptube plane could contribute a shared hit. A hit in any plane was considered shared if it was the closest hit to each track.

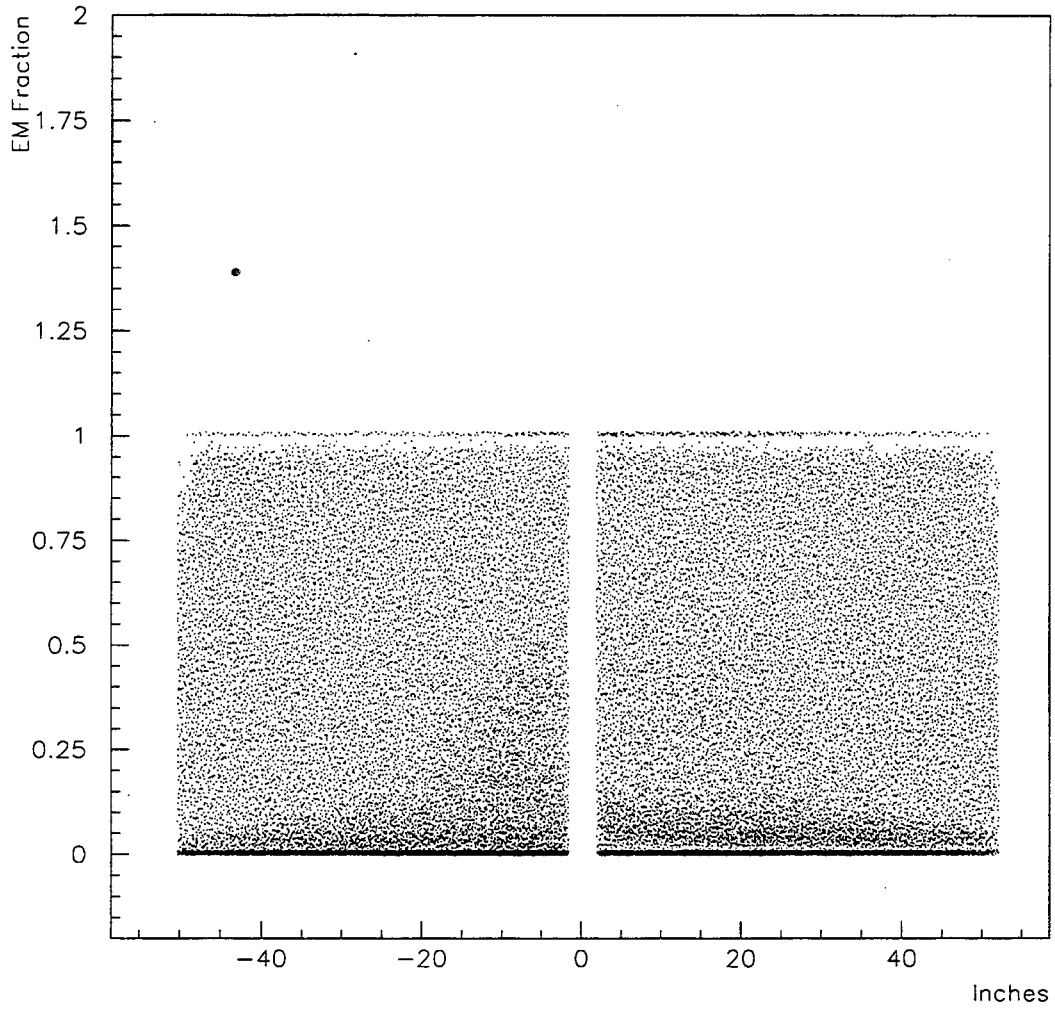

Figure 3.16: EM-fraction vs. X-position. Events include hadrons and electrons.

Chapter 4

Efficiencies

It is necessary to understand the acceptance efficiencies associated with each dilepton decay relative to the normalization decay. The relative acceptance efficiencies depend on both the kinematics and decay constituents of each mode.

4.1 Monte Carlo Simulation

The Monte Carlo (MC) program was used to generate events of each dilepton mode as well as the normalization mode. In addition, to simulating the kinematics, trigger and particle ID information were also incorporated. For each event type, the Monte Carlo program generated events that could be processed by the data analysis code. To generate MC events that best represented the real data, the MC used the same physical surveys and magnet field maps as used by the data analysis. Multiple scattering contributions throughout the spectrometer were also included. In addition, though of lesser importance when determining a relative efficiency, detector efficiencies were included and noise hits, extracted from data, were added to the silicon detectors for each generated event.

Event Generation

The D^0 was generated with an 800 GeV/c proton beam impinged on a fixed target. The fraction of momentum carried by the generated D^0, X_F, was characterized as $(1-X_F)^n$ with $n = 6.9$. [28] The transverse momentum distribution of the D^0 (P_t) was characterized as $e^{-bP_t^2}$ with $b = 0.84\ (GeV/c)^{-2}$ (see Figure 4.1). [28] Once the D^0 has been generated, it was allowed to propagate and decay via one of the aforementioned modes. Figure 4.2 shows

the distribution the decay vertex in the z-coordinate. Each decay was a two-body process generated with a flat angular distribution in the rest frame of the D^0. After boosting to the frame of the experiment, the decay constituents ($\mu\mu, \mu e$, or ee) were then allowed to propagate through the software-defined geometry of the spectrometer. Finally, each event that passed the geometric restrictions was required to satisfy the trigger as modeled for the decay of interest. Figure 4.3 compares the generated and accepted Z component of the momentum of the parent.

Comparison of Monte Carlo Events to Data

To demonstrate the efficacy of the Monte Carlo in generating events that accurately represent the data, a data set was chosen for comparison. The events were selected from real data to predominately include $D^0 \to K\pi$ decays. Each event had to have a reconstructed $K-\pi$ invariant mass near the D^0 mass and passed some loose Silicon Strip Detector impact parameter and vertexing cuts. The resulting mass distribution is in Figure 4.4. By making a further requirement that the reconstructed invariant mass fell within a tight window between 1.84 GeV/c^2 and 1.879 GeV/c^2, the final sample included a large proportion of $D^0 \to K\pi$ decays. The Monte Carlo events can now be compared to the data using selected reconstructed event parameters. Figures 4.7 and 4.8 compare the reconstructed momentum of the parent D^0 for both Monte Carlo events and data.

The distributions resulting from the $D^0 \to K\pi$ decay constituents can also be compared. However, while the kaon and pion were positively identified for events generated by the Monte Carlo program, there was no definitive mechanism for distinguishing between them in the data. The following procedure provides a large enhancement of $D^0 \to K\pi$ decays with each decay constituent properly identified. For $D^0 \to K\pi$ decays where the wrong particle ID was assumed, the invariant mass distribution was almost 7 times as wide (see Figure 4.6). As a result, a narrow cut on the invariant mass distribution filled with events reconstructed using only one reconstruction hypothesis (e.g. kaon charge > 0 and pion charge < 0) coupled with even tighter $D^0 \to K\pi$ selection criteria,[1] selected events whose decay constituents were likely to be properly identified (see Figure 4.5 for the invariant mass plot with the tight selection criteria before the mass cut).

Thus, the same tight mass cut for one mass combination allowed a crude pion/kaon

[1]The $D^0 \to K\pi$ signal was enhanced relative to the background through tight impact parameter cuts as described in Section 3.2.3.

track identification. Of course the pion/kaon identification was not exact; there could still be some fake $D^0 \to K\pi$ events. However, the tight mass cut and tight $D^0 \to K\pi$ requirements minimized the contamination. Once the $D^0 \to K\pi$ events were selected from data and the kaons and pions were identified, the MC could be compared to the data. Figures 4.9 and 4.10 compare the reconstructed momentum of pions for accepted Monte-Carlo-generated $D^0 \to K\pi$ events and real events. Figures 4.11 and 4.12 compare the reconstructed momentum of kaons for the same MC and real events. Finally, for the dilepton decays the only difference in the kinematics is due to the masses of the decay constituents. Figures 4.14 and 4.15 show the reconstructed momentum distribution of both muons and electrons in accepted Monte Carlo $D^0 \to \mu e$ events.

As a further comparison between Monte Carlo and data, Figure 4.13 shows the Y coordinate of each track in the Muon Station (at the end of the spectrometer) as a function of the track momentum. Negative and positive charged tracks are compared separately.

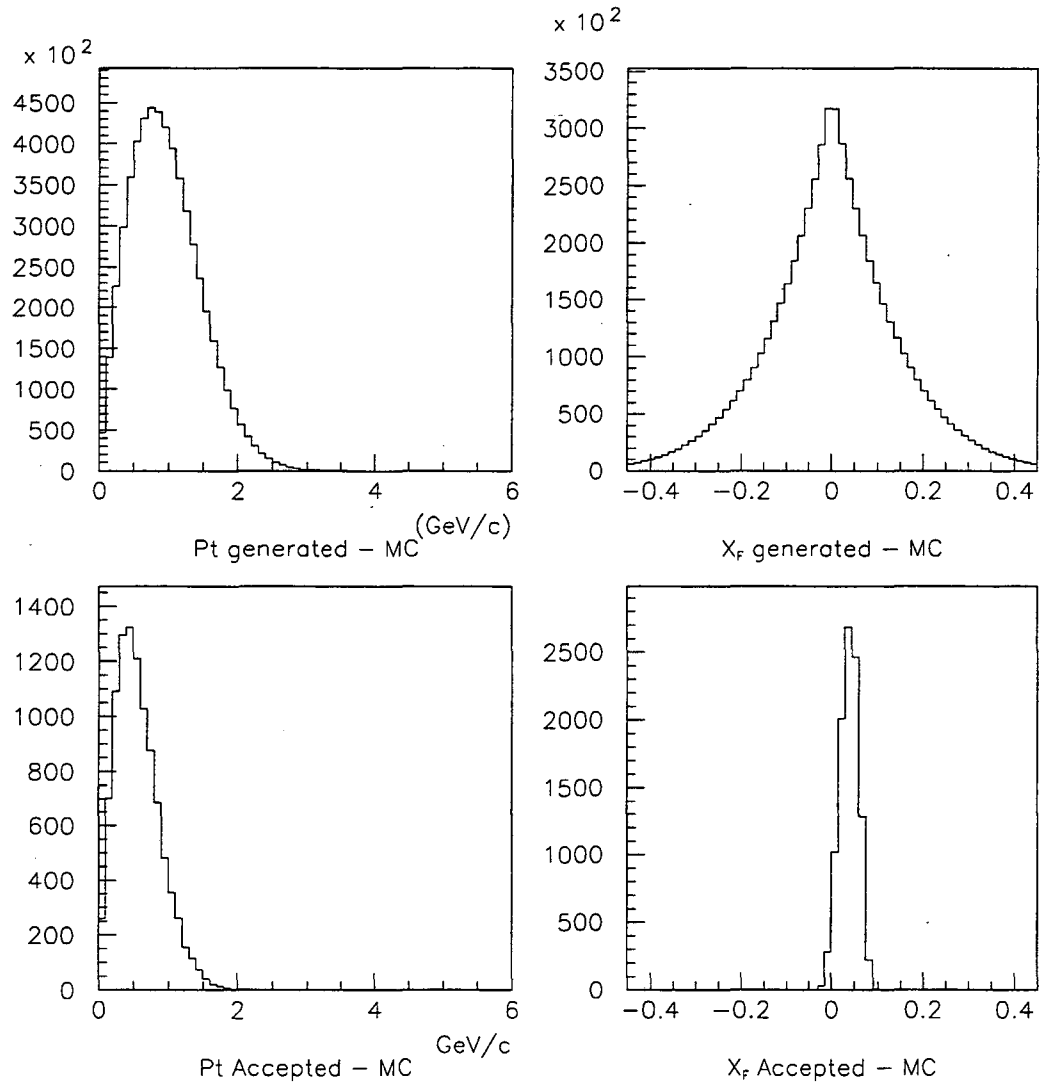

Figure 4.1: P_t and X_F distributions of Monte Carlo D^0 events. Distributions of generated events are above, accepted one are below.

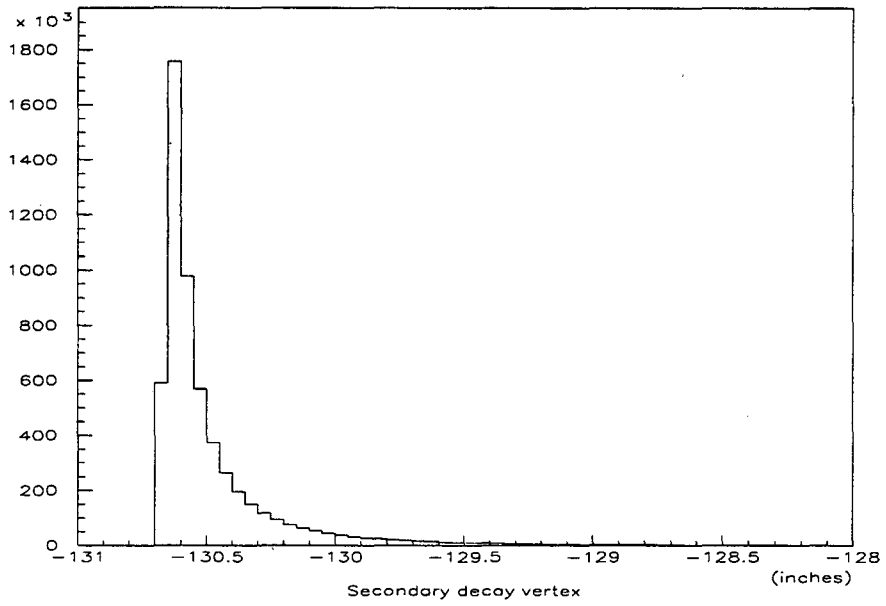

Figure 4.2: Generated Z-coordinate for the decay vertex of Monte Carlo D^0 decays.

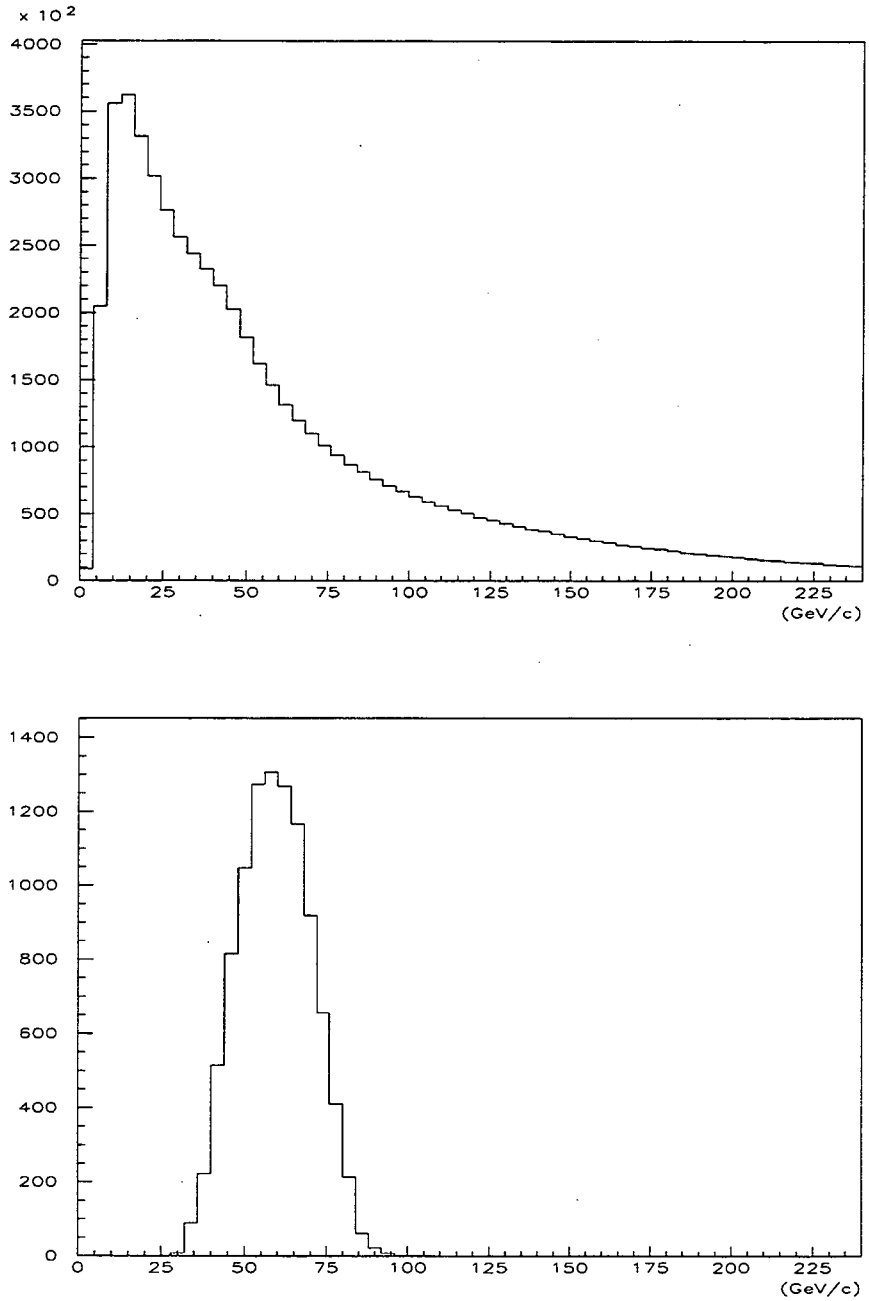

Figure 4.3: P_z distribution of Monte Carlo generated D^0 decays. Distribution of generated events is above, accepted one is below.

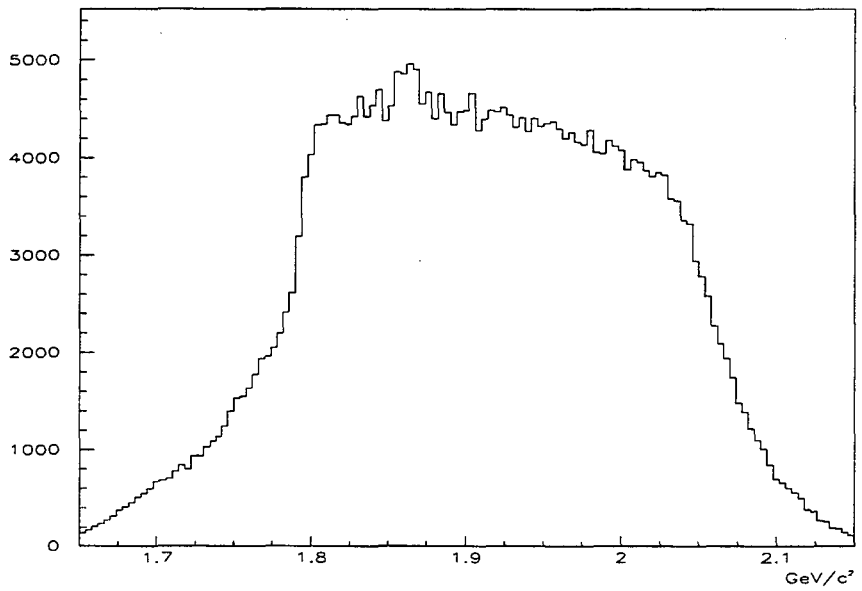

Figure 4.4: $K - \pi$ invariant mass distribution of dihadron events.

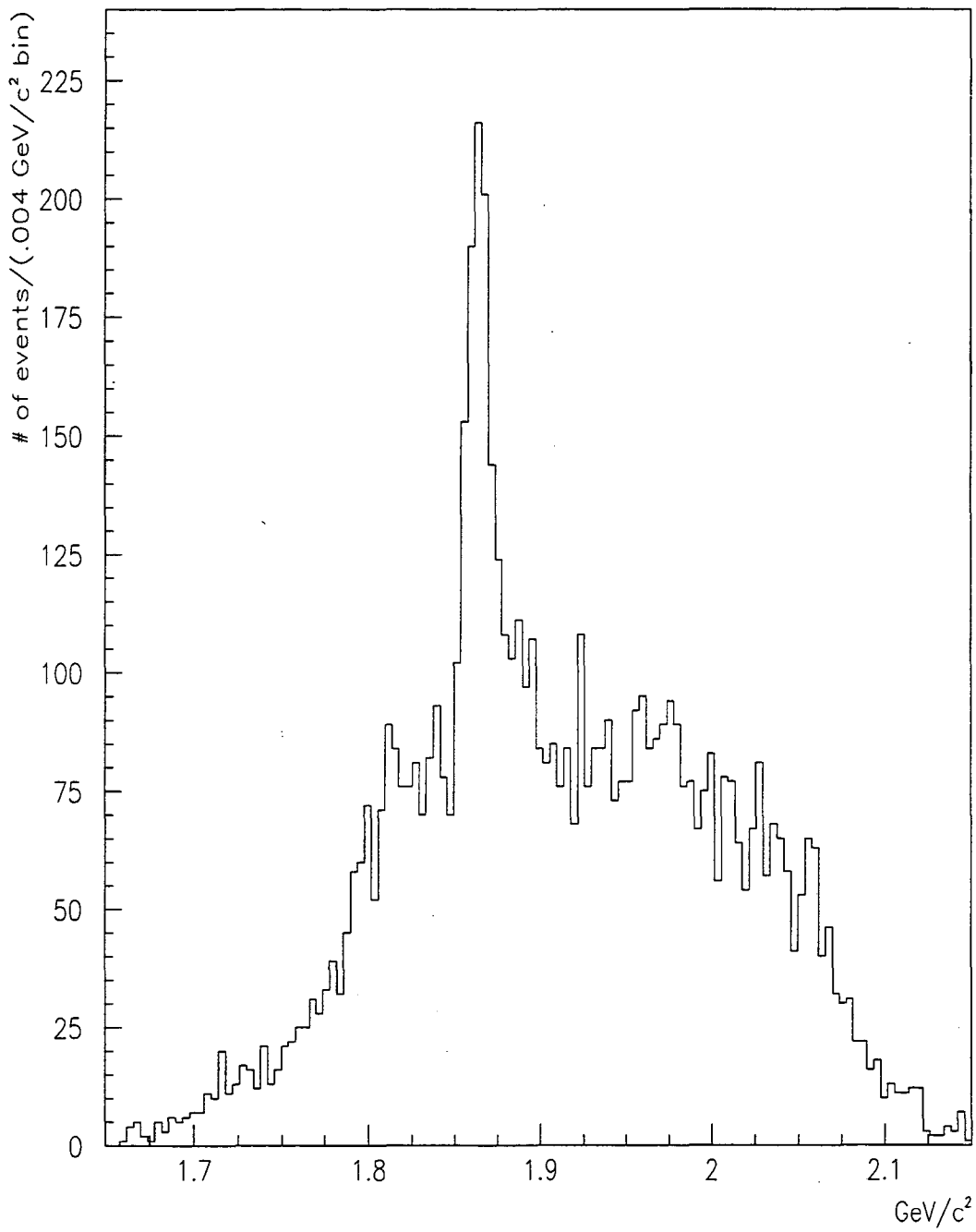

Figure 4.5: Invariant mass distribution for $D^0 \to K\pi$ events using tight selection criteria.

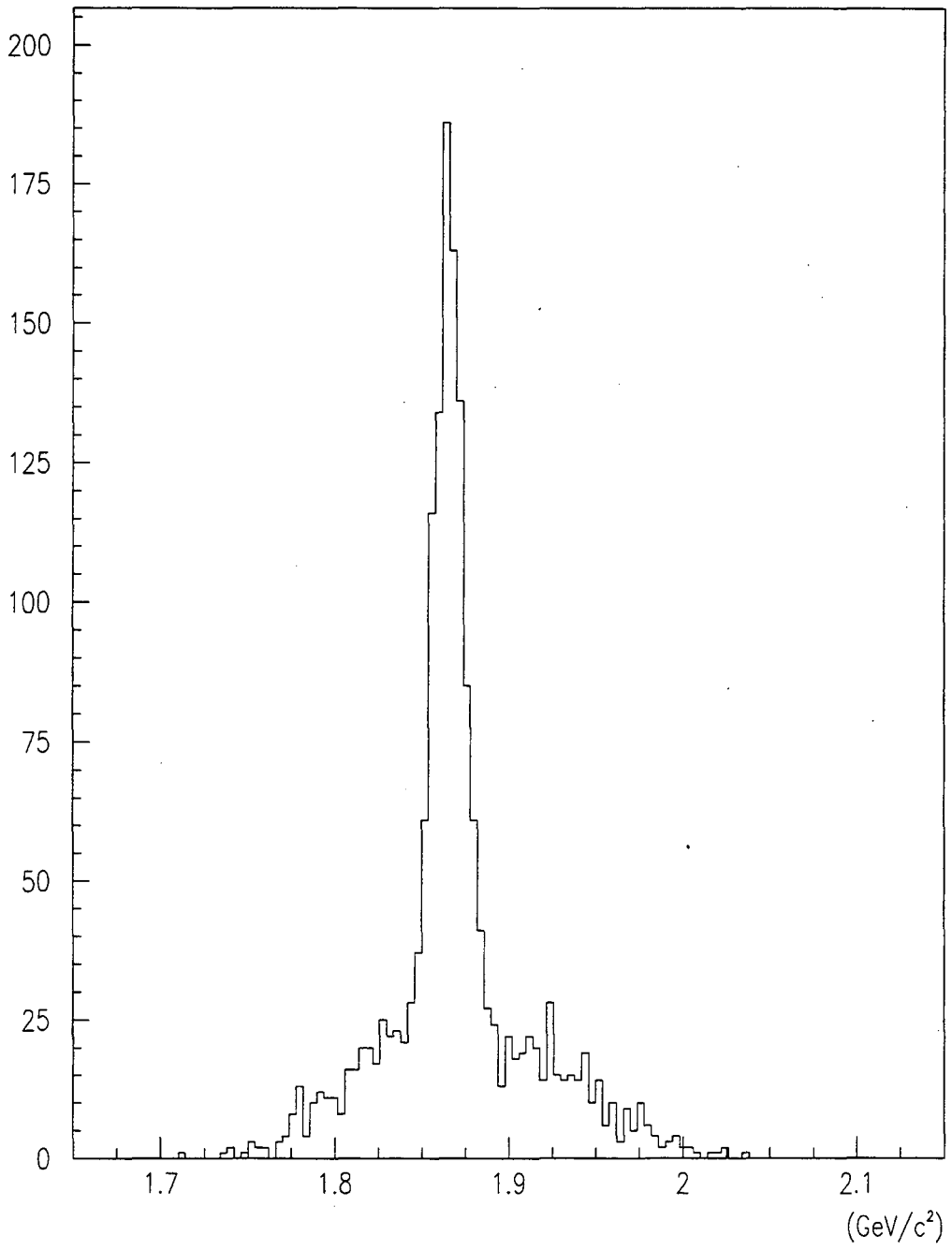

Figure 4.6: $D^0 \rightarrow K\pi$ invariant mass distribution of Monte Carlo events, with right and wrong particle ID assignment.

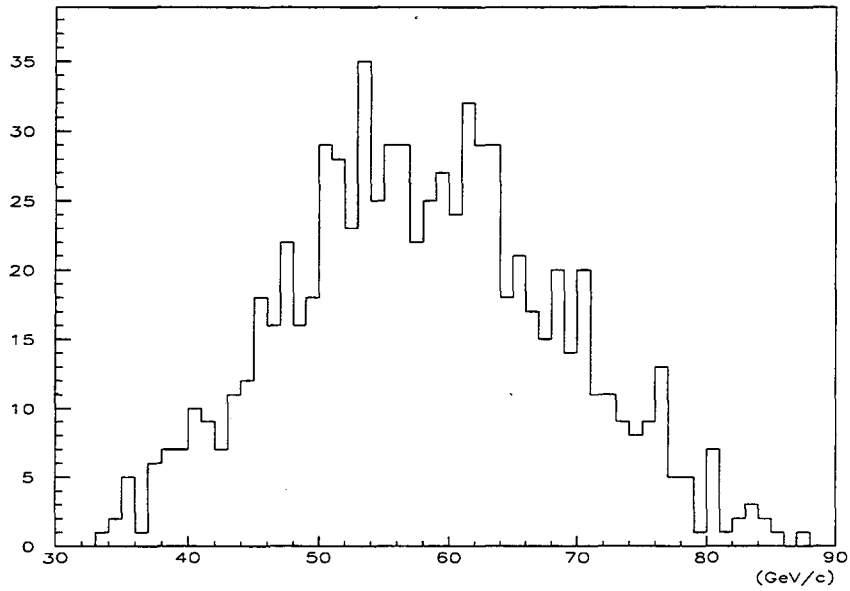

Figure 4.7: Reconstructed D^0 momentum of accepted Monte Carlo events.

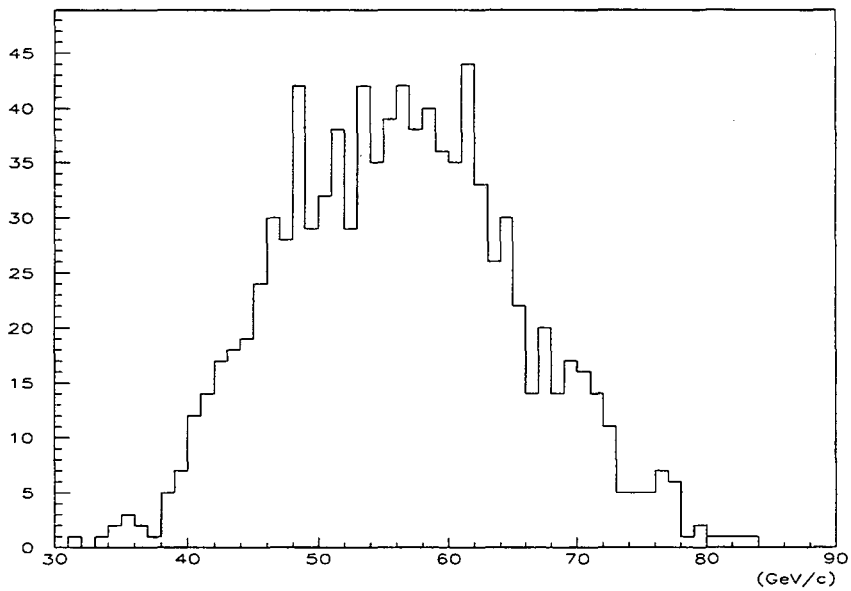

Figure 4.8: Reconstructed D^0 momentum from data under the D^0 mass peak.

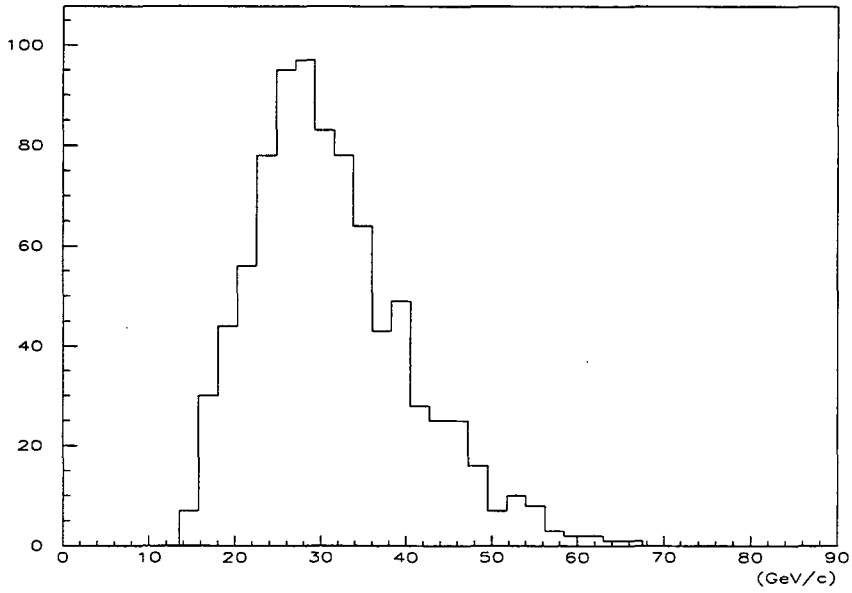

Figure 4.9: Reconstructed pion momentum of accepted Monte Carlo $D^0 \to K\pi$ events.

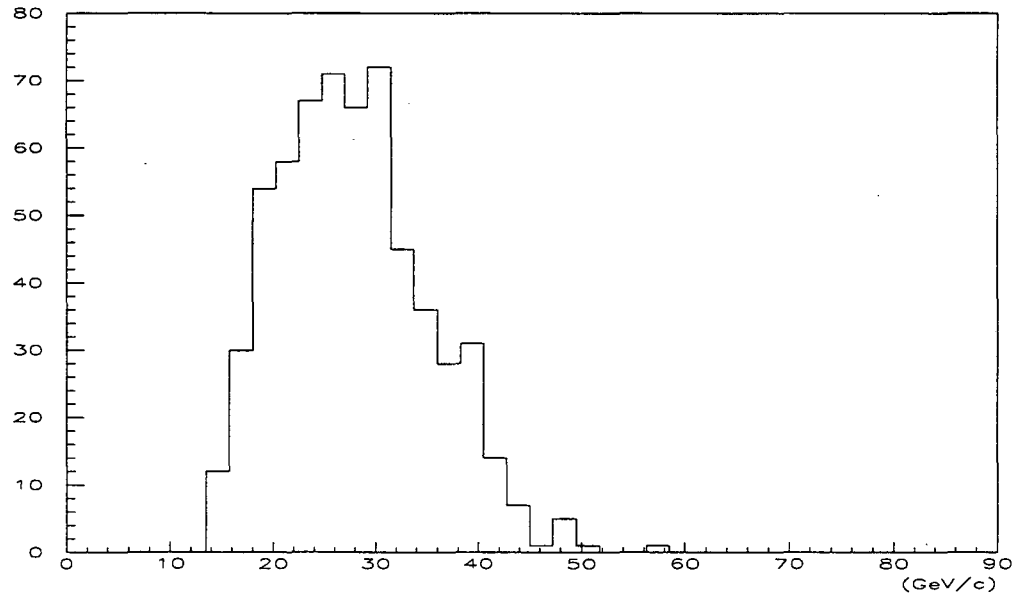

Figure 4.10: Reconstructed pion momentum from data under the D^0 mass peak.

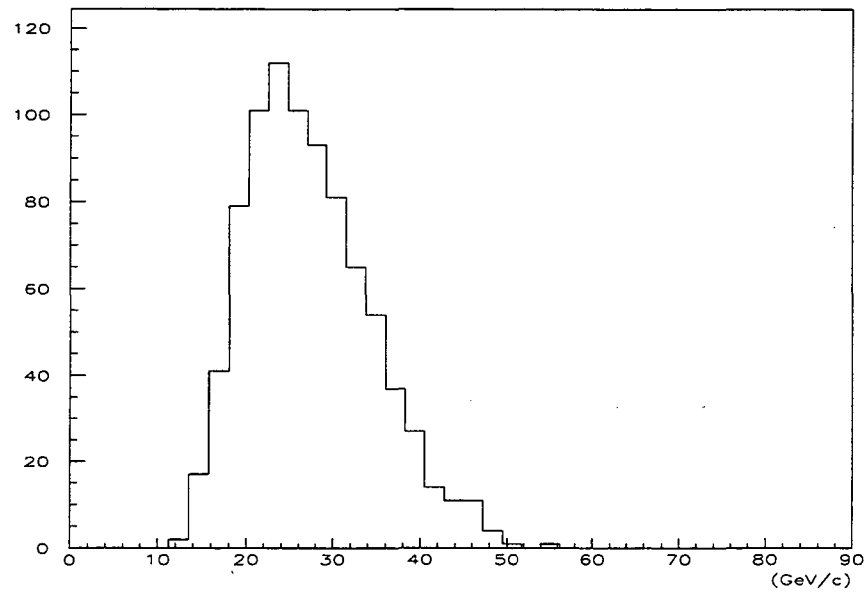

Figure 4.11: Reconstructed kaon momentum of accepted Monte Carlo $D^0 \rightarrow K\pi$ events.

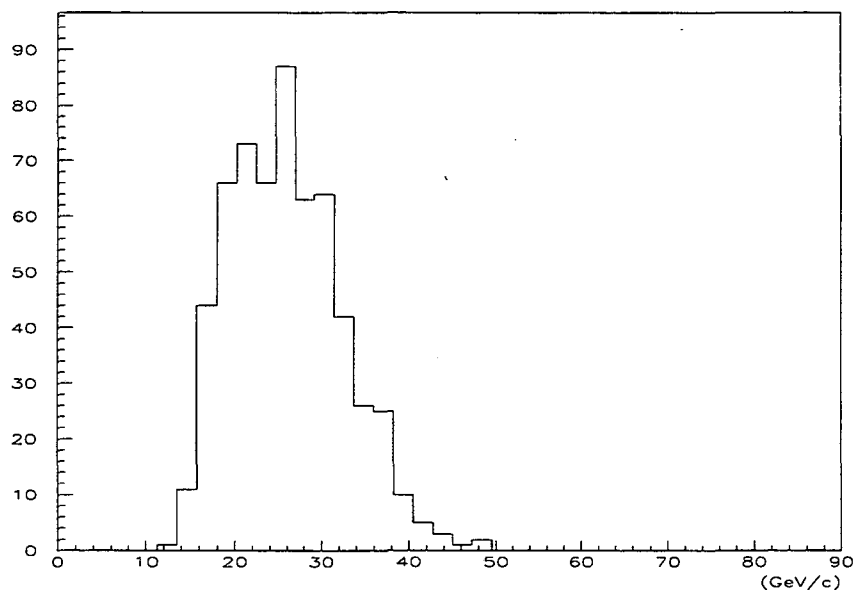

Figure 4.12: Reconstructed kaon momentum, from data, under the D^0 mass peak.

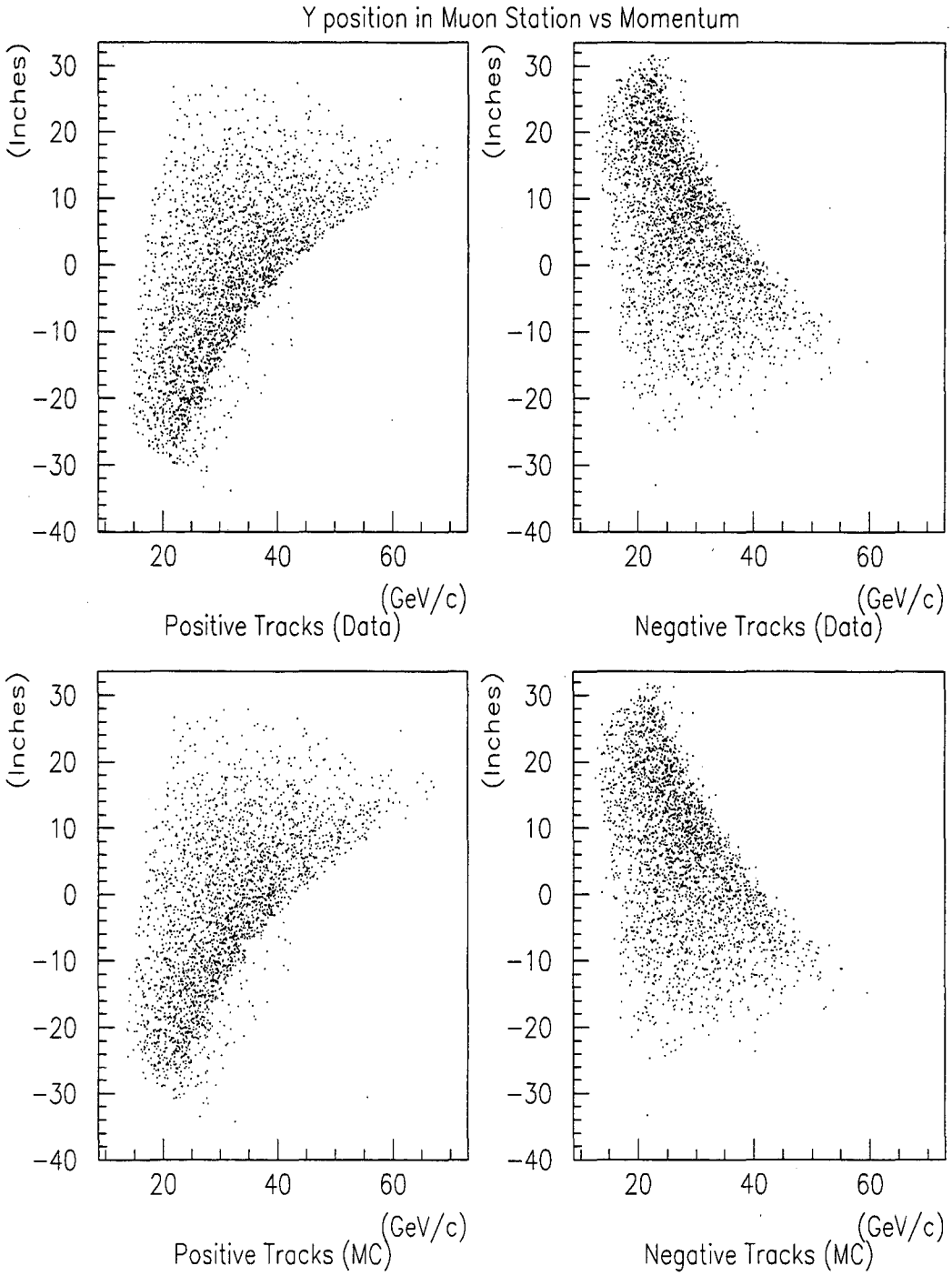

Figure 4.13: Y-Position vs. momentum, comparing data (above) and Monte Carlo (below).

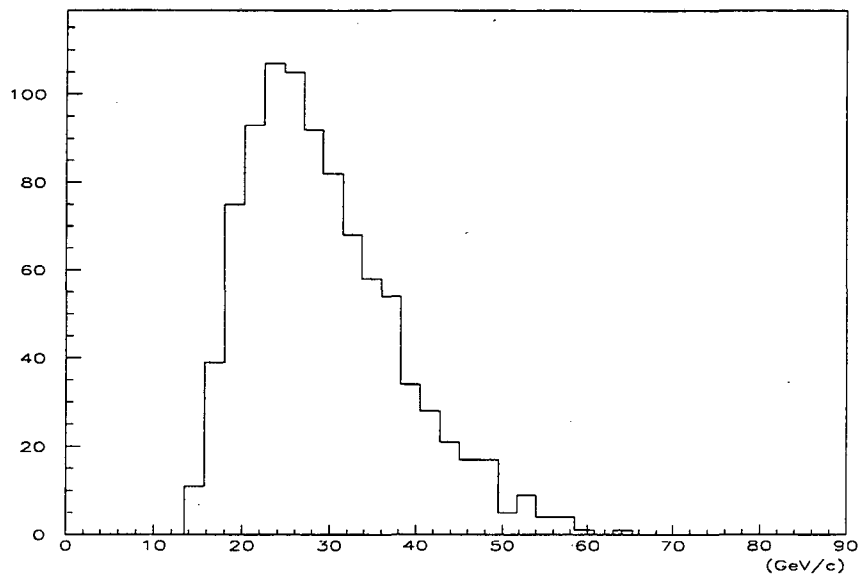

Figure 4.14: Reconstructed momentum of muons for accepted Monte Carlo $D^0 \rightarrow \mu e$ events.

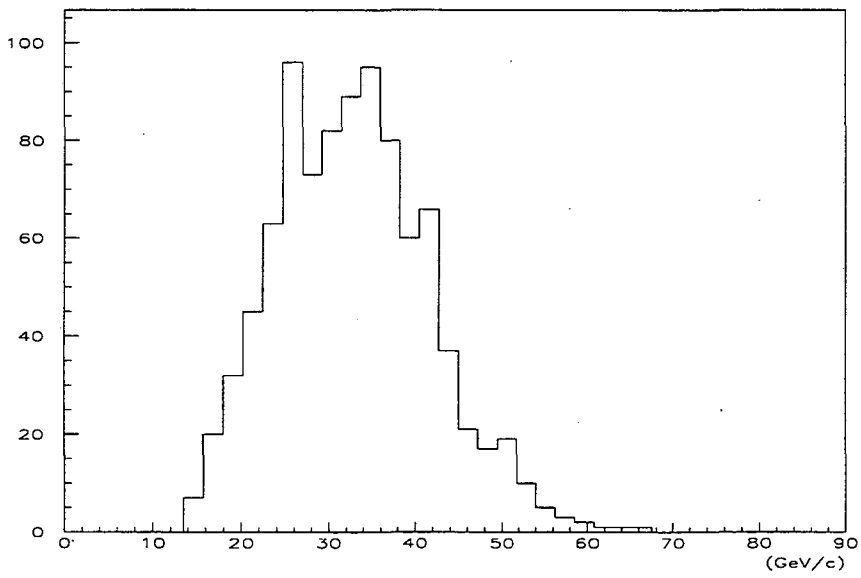

Figure 4.15: Reconstructed electron momentum of accepted Monte Carlo $D^0 \rightarrow \mu e$ events.

4.2 Geometric Acceptance

The different kinematics associated with each decay resulted in a different geometric acceptance for each decay mode. With the kinematics of each decay properly modeled, the Monte Carlo could generate the individual efficiencies by comparing the number of accepted events to the number of generated events. In addition, events that pass the geometric requirement, were subjected to the same vertex and impact parameter cuts that were applied to the data sample. The efficiency was calculated based on 40,000 events passing the geometric cuts for each mode (see Table 4.1).

Decay Mode	900A	1000A
$D^0 \to K\pi$	3.55×10^{-3}	2.37×10^{-3}
$D^0 \to \mu\mu$	3.97×10^{-3}	3.05×10^{-3}
$D^0 \to ee$	3.87×10^{-3}	3.28×10^{-3}

Table 4.1: Geometric acceptances for each decay mode. Each acceptance is based on 40,000 accepted events generated by Monte Carlo.

P_t and X_F variation

The uncertainty associated with the P_t and X_F distributions used as inputs to the Monte Carlo also contributed to the uncertainty in the relative efficiency. The limited acceptance of the spectrometer made the overall efficiency of each D^0 decay mode sensitive to variation in the P_t and especially the X_F inputs. Each input to both the P_t and X_f distributions was varied by one standard deviation. The X_F variation resulted in shifts in the absolute efficiency of up to $\pm 17\%$. However, in each case the relative efficiency of the dilepton mode and the associated normalization mode varied much less ($\sim 2\%$). Table 4.2 lists variation of each relative efficiency with the variation in P_t and X_F.

4.3 DiMuon Efficiency

Muons were identified using the Station 4 hodoscopes and proportional tubes (see Section 2.2.8 for details regarding the Station 4 configuration).

Decay Mode	P_t	X_F
$D^0 \to \mu\mu$	$3.13 - 3.14$	$3.07 - 3.10$
$D^0 \to ee$	$2.35 - 2.39$	$2.28 - 2.40$
$D^0 \to \mu e$	$2.05 - 2.06$	$1.97 - 2.06$

Table 4.2: Variation in efficiency of each dilepton mode relative to the normalization mode resulting from a one-σ variation in the inputs to the P_t and X_F characterization.

4.3.1 Proportional Tube Efficiency

The efficiency of each proportional tube (Proptube) plane was determined separately and then included in the Monte Carlo simulation. Each muon selected for this study was required to register a hit in both hodoscope planes and the remaining two Proptube planes.[2]

The Hit-Window

For a plane to register a hit associated with the track, a hit must fall within the momentum dependent hit-window at that plane. The hit-window at each plane was determined by forming a residual distribution of the spatial difference between the projection of the reconstructed track to that plane and the nearest hit in the same plane.[3] Each residual distribution was then fit to a Gaussian (see Figure 4.17). Finally, the distribution of the standard deviation (σ) of the residuals for each plane were fit to the inverse of the track momentum with a quadratic characterization. The resulting fit was then used to form a hit-window for a track at each Proptube plane by determining the σ associated with the plane for the momentum of the track (see Figure 4.18). The final window used was three-σ-wide. As before, requiring all planes to fire except the one being studied allowed for an unbiased study of that plane. As the Proptubes were not included in the trigger, no special trigger requirements were necessary.

As a by-product, the efficiency of a Proptube was then the fraction of events where an identified muon fired the plane in question. Figure 4.19 shows the Proptube efficiencies as a function of muon momentum.

[2]Since the Proptubes were not part of the dimuon trigger, no bias was introduced by requiring both hodoscope planes.

[3]The muon was identified using the other four planes in Station 4.

4.3.2 Muon Hodoscope Efficiency

The only component in the dimuon trigger which was not included in the dihadron trigger[4] was the requirement that two out of four hodoscope sectors fired in both the X and Y planes in Station 4 (see Section 2.4 for details of the E789 trigger). Determining the dimuon efficiency thus required an unbiased study of the Station 4 hodoscopes. An unbiased muon sample was chosen by selecting events that satisfied the calorimeter trigger and included at least one reconstructed muon. Muons were selected that fired two of the three Proptube planes (not included in the trigger) and one hodoscope plane. The σ for the hodoscope hit-window was formed using the σ associated with the nearest Proptube. The requirement of a hodoscope plane, whose timing had single-bucket resolution, assured that the reconstructed track was indeed associated with the triggered event. Events were required to satisfy the calorimeter trigger because the calorimeter trigger was independent of the dimuon trigger. The efficiency of each hodoscope plane was then simply determined by recording the fraction of events for which the hodoscope that was not used in the muon selection process fired as a function of the muon's momentum. Figure 4.20 shows the efficiency of each hodoscope plane as a function of muon momentum. These efficiencies were then included in the MC simulation. Two paddles of each hodoscope plane were included in the muon trigger. The MC simulation satisfied this requirement in two phases. First, dimuon events were generated with each muon required to fire both hodoscope planes. Then, the events were reconstructed with the requirement that four hodoscope planes had fired (two paddles for each plane).

To avoid misidentification from overlapping tracks, an isolation cut using the Proptubes was applied (see Section 3.4.3). The trigger requirement already isolated the tracks such that the additional Proptube isolation requirement reduced the efficiency by only 7% while reducing background significantly. The final efficiency is the result of the complete Monte Carlo simulation which included trigger requirement, and 2 out of 3 Proptubes, coupled with the momentum profiles of the $D^0 \rightarrow \mu\mu$ decay constituents.[5] This, combined with the isolation requirement, resulted in the overall dimuon efficiency of 36%. To study the variation in the overall dimuon trigger efficiency, completely independent study data sets were generated. The dimuon efficiency varied by less than 1% using any combination of the data sets.

[4]The dihadron trigger efficiency was used to form the relative trigger efficiency between the $D^0 \rightarrow \mu\mu$ decay and the $D^0 \rightarrow K\pi$ decay.

[5]Recall, all the efficiencies were tabulated as a function of muon momentum.

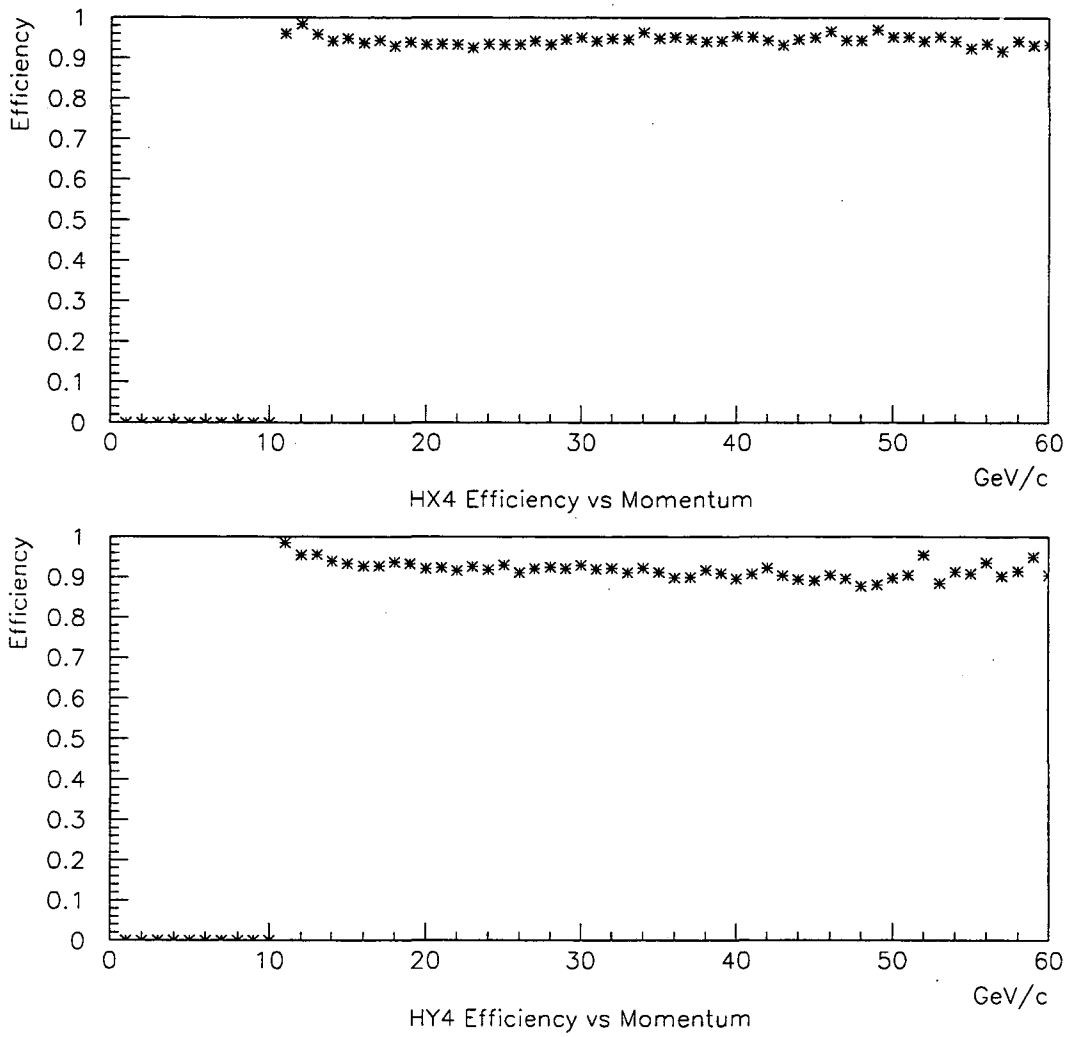

Figure 4.16: Efficiencies of the HX4 and HY4 hodoscopes as a function of muon momentum.

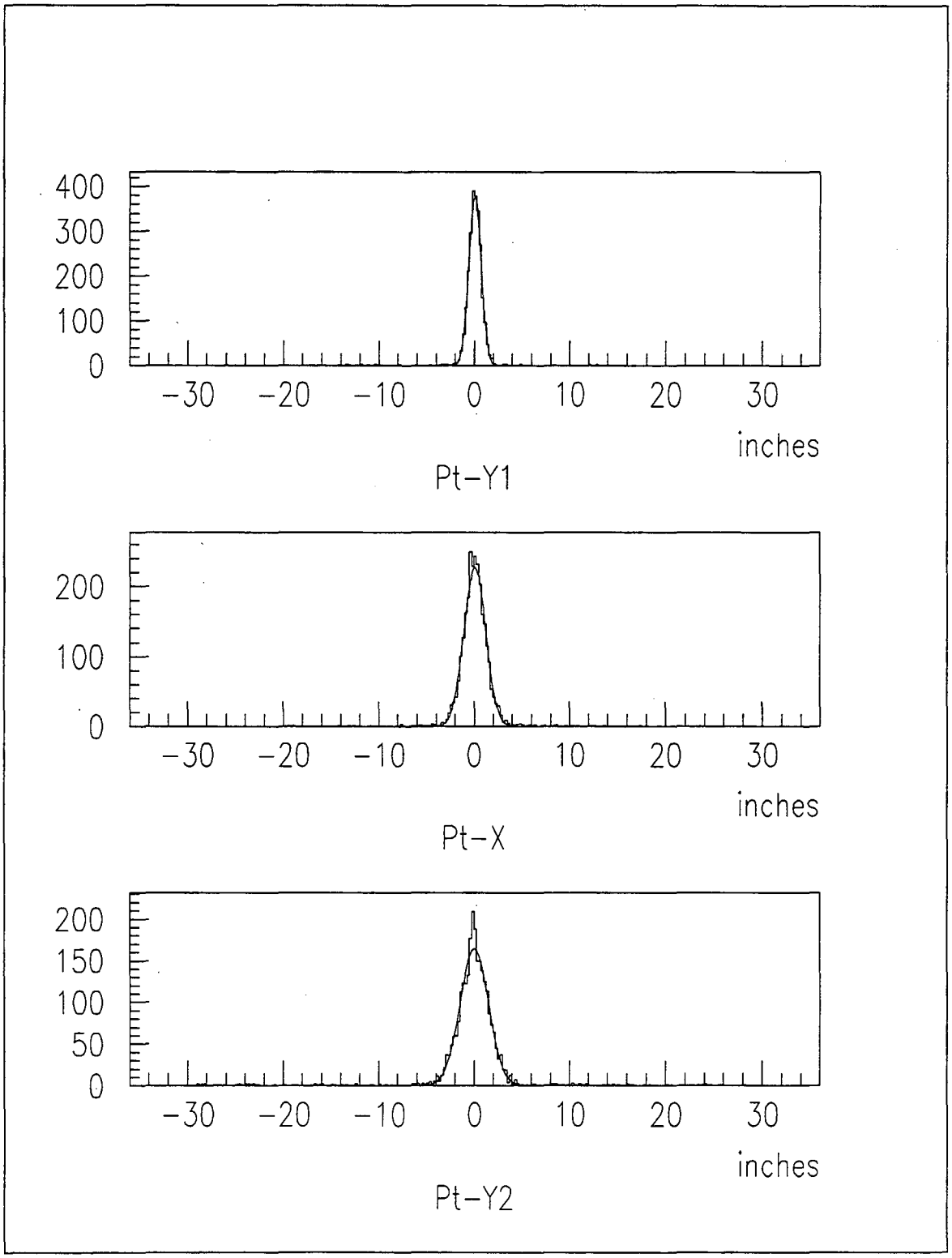

Figure 4.17: Residuals of proportional tube for 30 GeV/c muons.

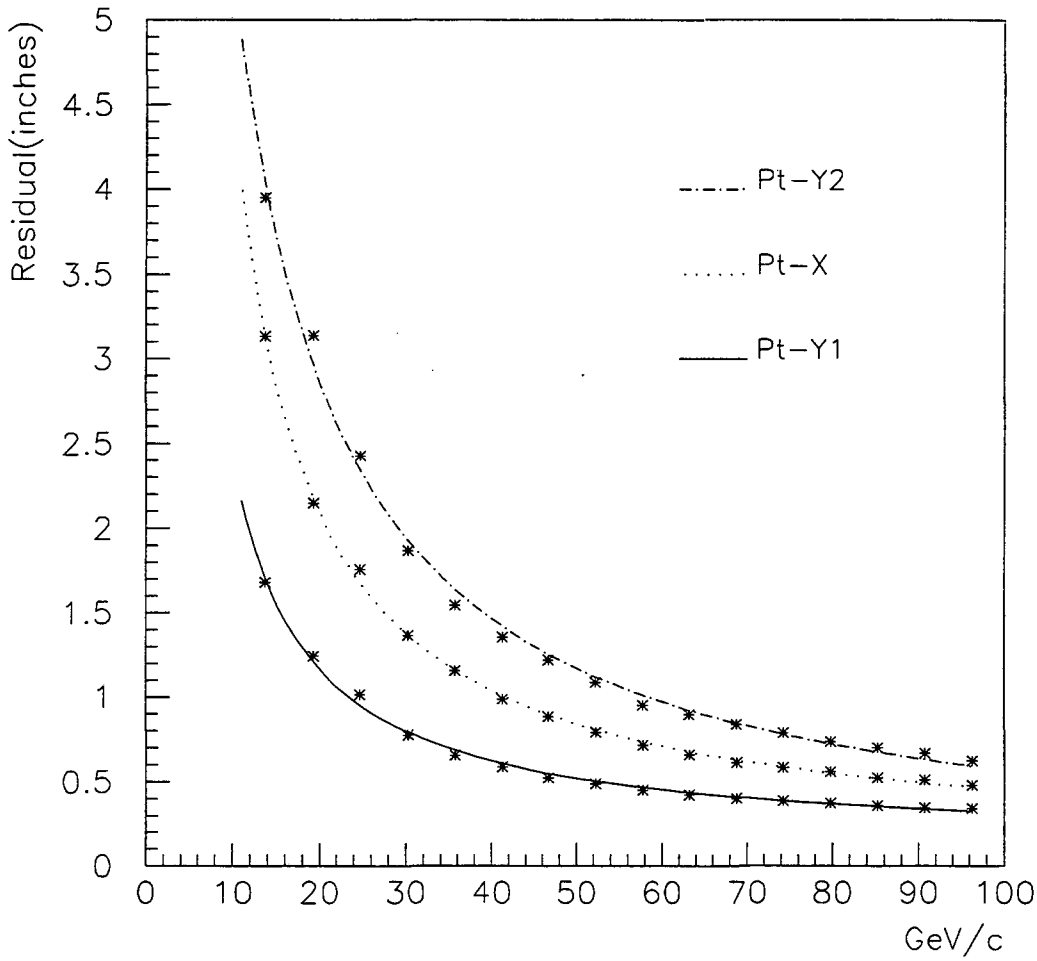

Figure 4.18: σ of residuals as a function of muon momentum for each proportional tube. The points represent the data, the lines represent the fit to the data.

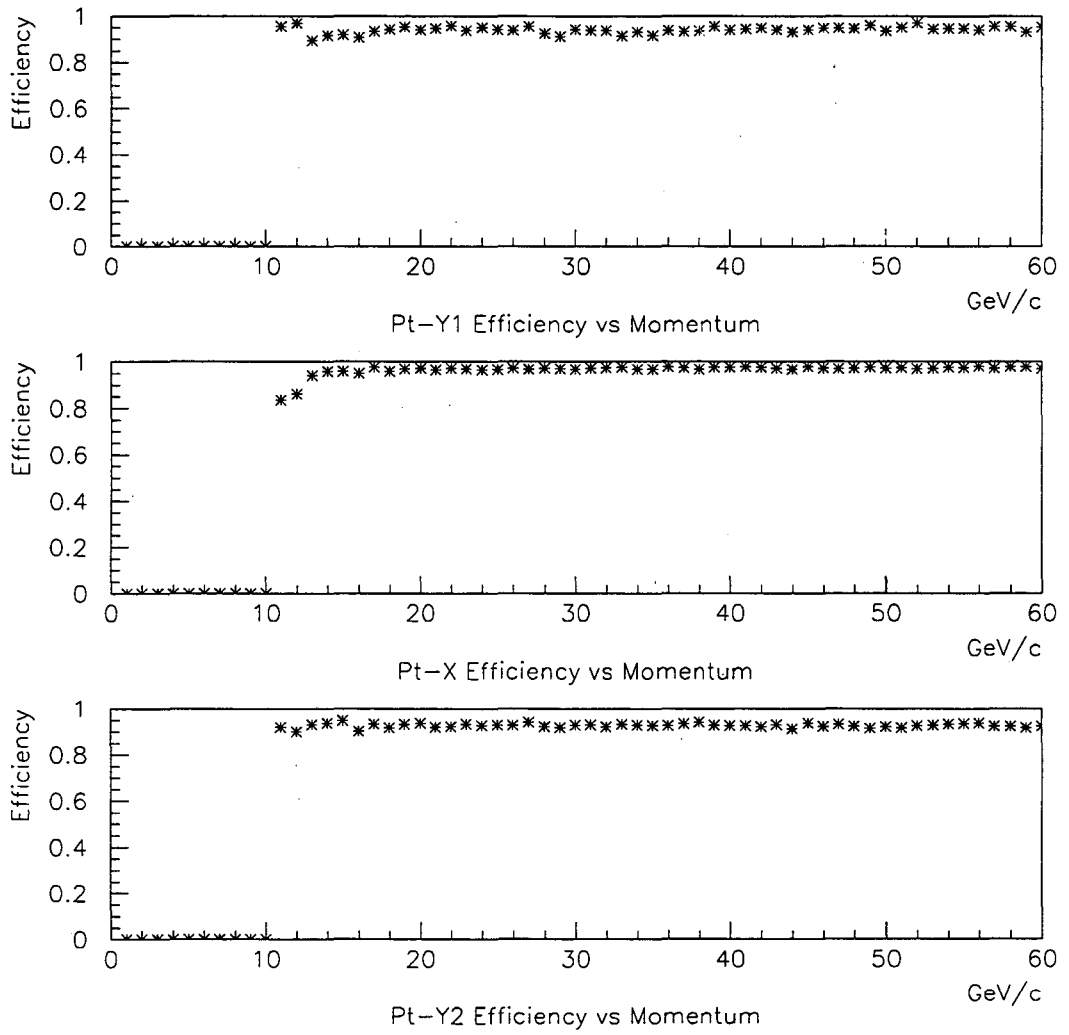

Figure 4.19: Efficiencies of the proportional tubes as a function of muon momentum.

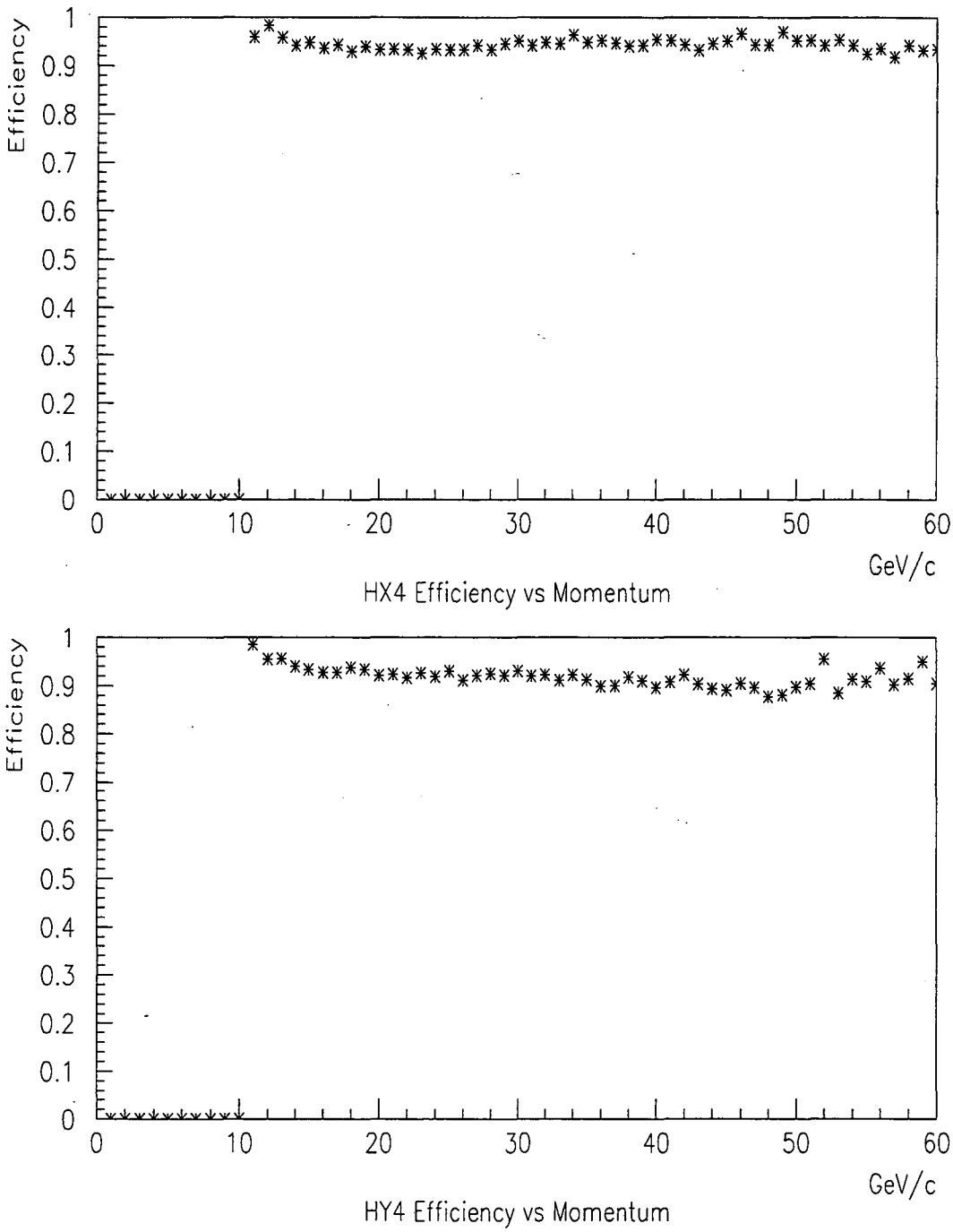

Figure 4.20: Efficiencies of the HX4 and HY4 hodoscopes as a function of muon momentum.

4.4 Dihadron Efficiency

The efficiency of the dihadron decay mode ($D^0 \rightarrow K\pi$) relative to the dilepton decay modes is dominated by the dihadron trigger efficiency. All other components of the trigger are the same for each decay mode except the particle-ID component (see Table 2.8 for a list of the trigger components). Both the dihadron trigger, and the energy deposition of hadrons in the calorimeter were modeled in the Monte Carlo.

The dihadron trigger efficiency was first determined as a function of the total momentum of the decay constituents in a dihadron event. The efficiency curve could then be used as an input to the MC.

The sample used for the dihadron-trigger-efficiency study consisted of events which passed the lowest level trigger and were not required to satisfy any of the higher level triggers; this requirement removed any possible bias by the dihadron trigger. (Note, the TFI did not include the calorimeter; see Section 2.4 for a discussion of the E789 trigger.) The dihadron sample was chosen to match the momentum profile of the accepted $D^0 \rightarrow K\pi$ events. Events were selected that had two hadron tracks with a reconstructed $K-\pi$ invariant mass in a 0.5 GeV/c^2 window about the D^0 mass. The trigger efficiency was tabulated in 2 GeV/c momentum bins. The fraction of events that fired the dihadron trigger was plotted as a function of the total momentum in 2 GeV/c bins. The resulting efficiency vs. momentum distribution was characterized by a third order polynomial. Figure 4.21 shows the efficiency as a function of momentum and the resulting fit. The efficiency curve was then used as an input to the Monte Carlo. Each event generated in the Monte Carlo was required to pass the simulated dihadron trigger which was modeled using a random number, the efficiency curve and the total momentum of the generated event. The average trigger efficiency for $D^0 \rightarrow K\pi$ events which passed the geometric acceptance of the MC was 55%. By using two calorimeter trigger data sets, in addition to the data set used for this study, and an independently generated calorimeter calibration file (see Section 3.3 for a discussion of the calorimeter calibration), the variation in the dihadron trigger efficiency was found to be less than 1%.

In addition to the trigger efficiency, the energy deposition of hadrons in each section of the calorimeter was also included in the MC simulation. The energy deposition for a generated momentum was modeled with the deposited energy histograms, which were based on data. In addition, an EM-fraction vs. momentum histogram was included. As a result,

each MC event included the total energy deposited in the calorimeter and the fraction of that energy deposited in each section. To enhance the certainty of hadron identification, the fraction of energy deposited in the electromagnetic section of the calorimeter (EM-fraction) was required to be below 70%. This cut accepted over 92% of hadrons (see Figure 4.22). Furthermore, the total energy that the particle deposited in the calorimeter divided by the particle's momentum (E/P), as determined by the spectrometer, must fall within $\pm$ 2.58 σ of the known E/P mean (see Figure 3.12).

Finally, kaon decay in-flight was also included in the Monte Carlo. Using a lifetime of 1.24×10^{-8} *sec*, a decay length was calculated for each event. The Monte Carlo tracked the path length of the particle and if the particle reached the decay point before the middle of the hadronic calorimeter, it was assumed the event was lost. The kaon decay before Station 4 could either cause the event to be misidentified or altered the event kinematics such that the reconstructed invariant mass dropped out of the D^0 region. In either case, such an event would not be included as a $D^0 \rightarrow K\pi$ candidate. Kaons that decayed into pions were accepted if the decay occurred after the last tracking chamber. 80% of $D^0 \rightarrow K\pi$ events survived this kaon decay cut.

4.5 Dielectron Trigger efficiency

The trigger efficiency for the decay $D^0 \rightarrow ee$ relative to $D^0 \rightarrow K\pi$ was dominated by the electron calorimeter trigger (see Section 2.4 for a discussion of the trigger components). The calorimeter triggers for electrons were formed by the sum of the signals from layers E2 and E3 of the calorimeter (see Section 3.3 for a discussion of the calorimeter). Two triggers were formed from this input by setting a threshold on the signal output to discriminate between single and multiple electron events. To determine the efficiency of the two-electron threshold (E_{high}), the same prescaled TFI data sample as was used for the dihadron trigger efficiency study was selected. An efficiency curve was then generated by calculating the efficiency of the trigger as a function of the ADC (Analog to Digital Converter) output of the trigger. The same events were then used to map the ADC output of E_{high} to the energy stored in the associated components of the calorimeter (E2+E3). The efficiency information was then included in the Monte Carlo.

Electron Trigger Simulation

To use the above efficiency information in the Monte Carlo, the electron behavior in the calorimeter also had to be included. To this end, events were selected that had an EM-fraction of greater than 0.95 (the electron identification requirement) and were isolated in the calorimeter. The energy deposited in the EM trigger components E2+E3 was histogramed as a function of the momentum of the track, and was included in the Monte Carlo. The trigger could then be studied as follows. An electron was generated from the $D^0 \rightarrow ee$ decay. The energy that the electron deposited in the calorimeter was generated randomly, based on the (E2+E3)/(momentum) distribution (see Figure 4.23). The (E2+E3)/(momentum) distribution was momentum dependent; so, for each 5 GeV/c momentum bin, a different distribution was used (see Figure 4.24). Once the energy stored in E2+E3 was determined, an ADC count could be generated randomly, based on the (E2+E3) to ADC mapping determined from the data (see Figure 4.25 and Figure 4.28). Finally, a random number was thrown between zero and one and was compared to the generated efficiency. Figure 4.26 shows the dielectron trigger ADC efficiency. The final trigger efficiency for $D^0 \rightarrow ee$ events that passed the Monte Carlo geometric cuts (including the momentum $\geq$ 18.5 GeV/c cut) was determined to be 60%. Figure 4.30 shows the dielectron efficiency as a function of the generated D^0 momentum.

Independent data sets were used to study the variation in the trigger efficiency, which was found to be less than 1.5%. For an electron to be identified, the EM-fraction was required to be ≥ 0.95. A separate study, using $J/\psi \rightarrow e^+e^-$ decays from data collected in an adjacent running period, found this cut to be $\geq$ 96% efficient. [25]

4.6 μe Efficiency

To find the efficiency of $D^0 \rightarrow \mu e$ relative to $D^0 \rightarrow K\pi$, we use the techniques and tools developed for the $D^0 \rightarrow \mu\mu$ and $D^0 \rightarrow ee$ efficiency analyses. In the $D^0 \rightarrow \mu\mu$ analysis, each muon was treated separately and then the two were combined to find the overall efficiency. To adapt to a single muon event, we used a simple 2-hodoscope requirement for the trigger, and 2 out of 3 Proptube planes. The single-electron was treated in a similar manner as the dielectron with the only difference being that the lower threshold of the single-electron trigger (see Section 4.5) required a different trigger efficiency to ADC mapping.

As with the dielectron case, the generated electron must pass the geometric cuts of the Monte Carlo. The electron momentum was then translated to a trigger energy which was converted to a trigger ADC count (see Figures 4.23, 4.25, and 4.29). The resulting ADC count was then mapped to its associated efficiency (see Figure 4.27). Figure 4.31 shows the turn-on curve for the single electron trigger as a function of generated D^0 momentum. The resulting single-electron efficiency was 48% and the single muon efficiency was 74%.

Using the independent data sets used to study the variation in the dielectron and dimuon triggers, the overall variation in the μe trigger was found to be less than 3%.

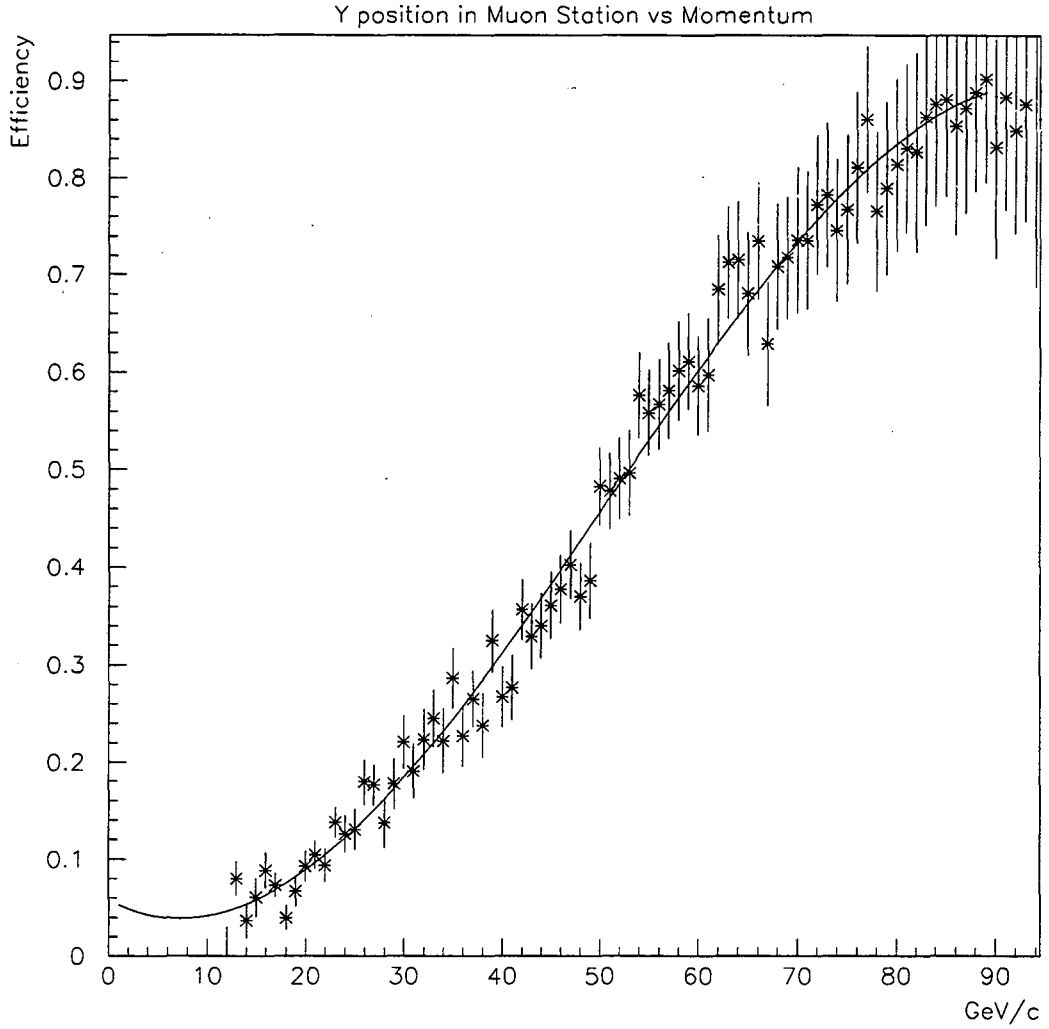

Figure 4.21: Trigger efficiency of dihadrons. The solid line is the characterization used by the Monte Carlo program.

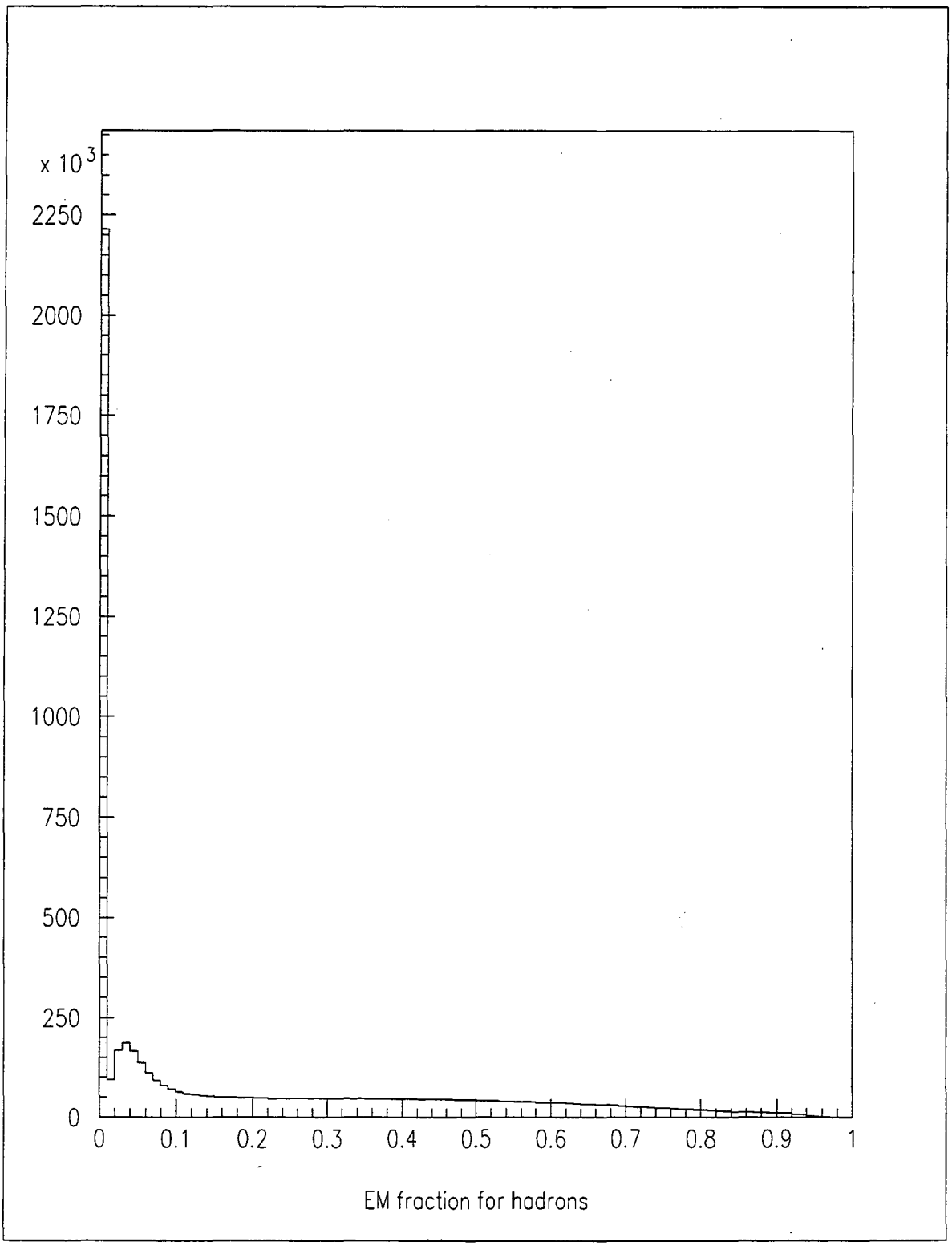

Figure 4.22: Fraction of energy deposited in the hadron section of the calorimeter.

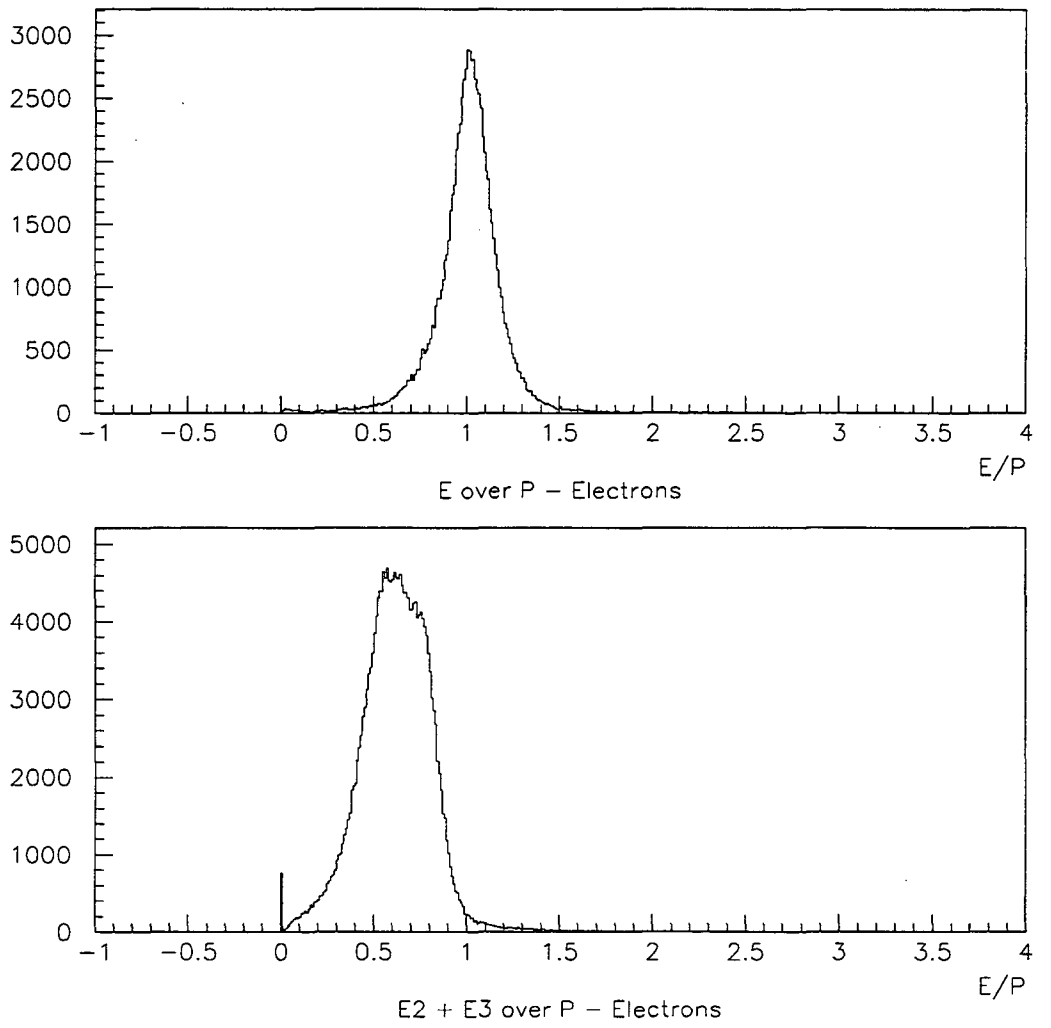

Figure 4.23: Energy divided by momentum of electrons in the entire calorimeter (above) and in the trigger components (below).

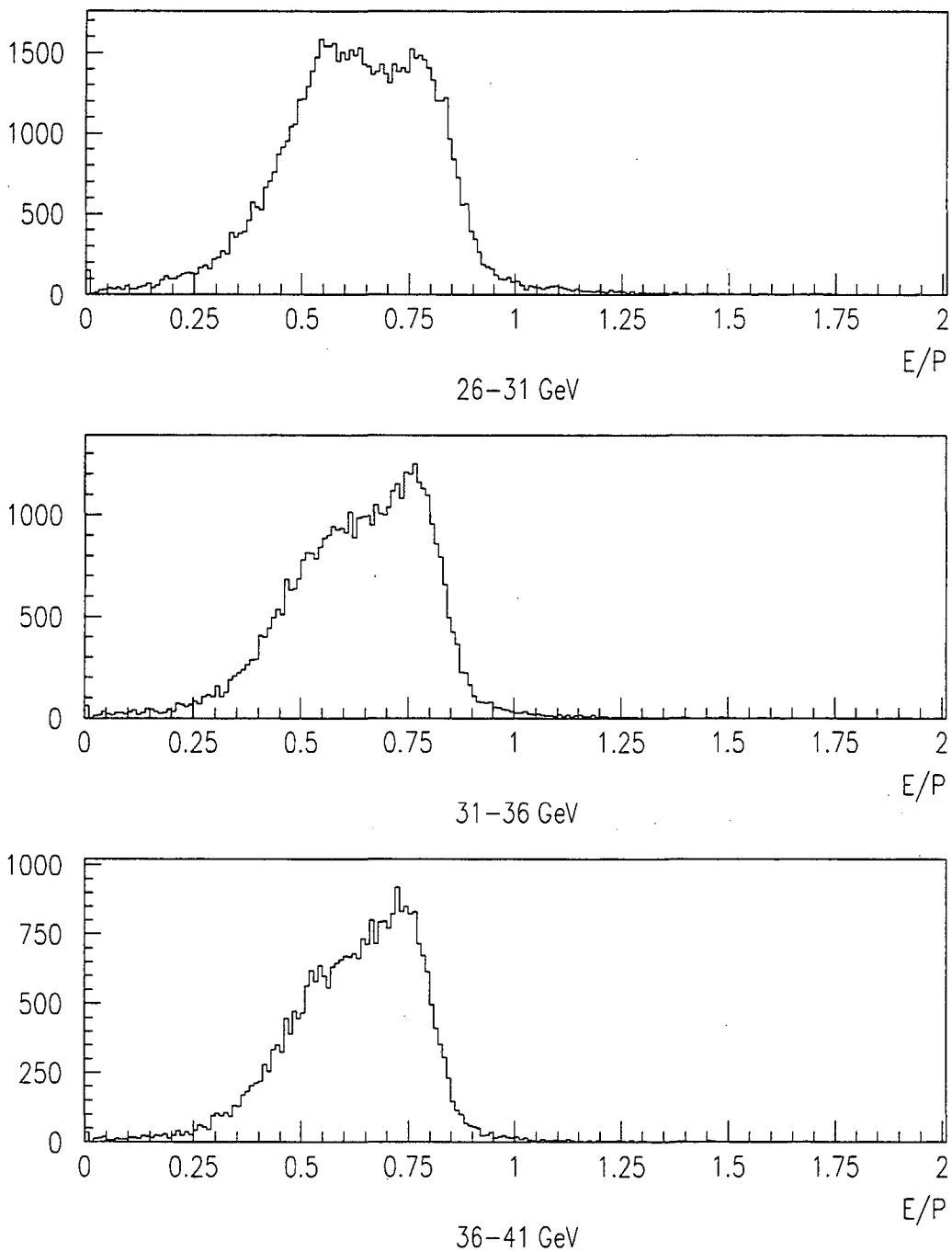

Figure 4.24: Momentum dependence of (E2+E3)/P.

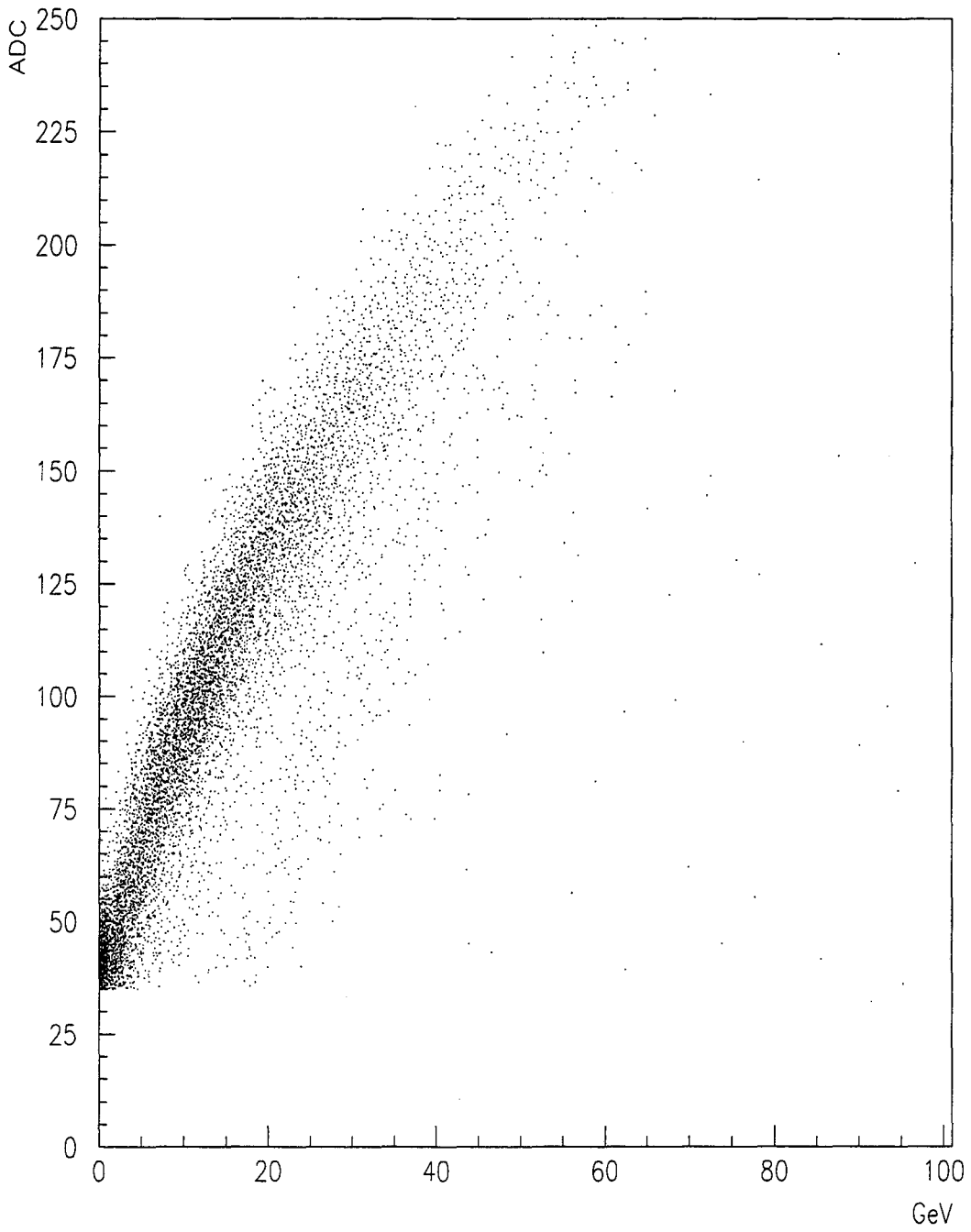

Figure 4.25: Trigger ADC map to electron trigger component (E2+E3).

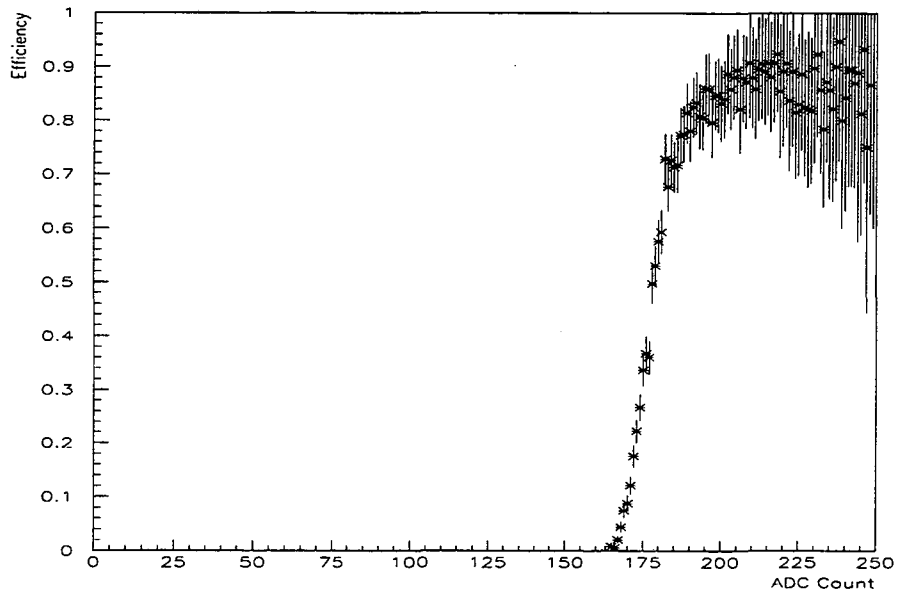

Figure 4.26: Dielectron trigger efficiency vs. trigger ADC.

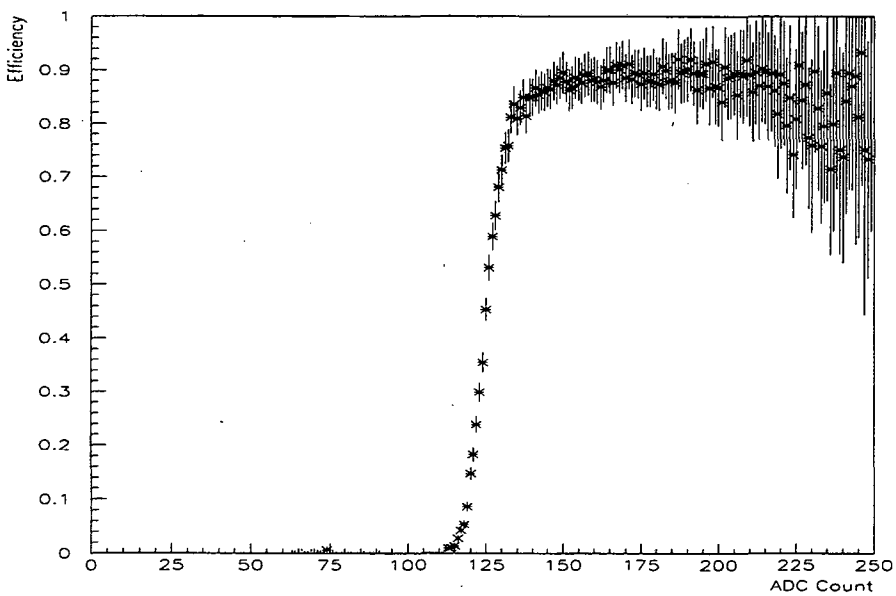

Figure 4.27: Single-electron trigger efficiency vs. trigger ADC.

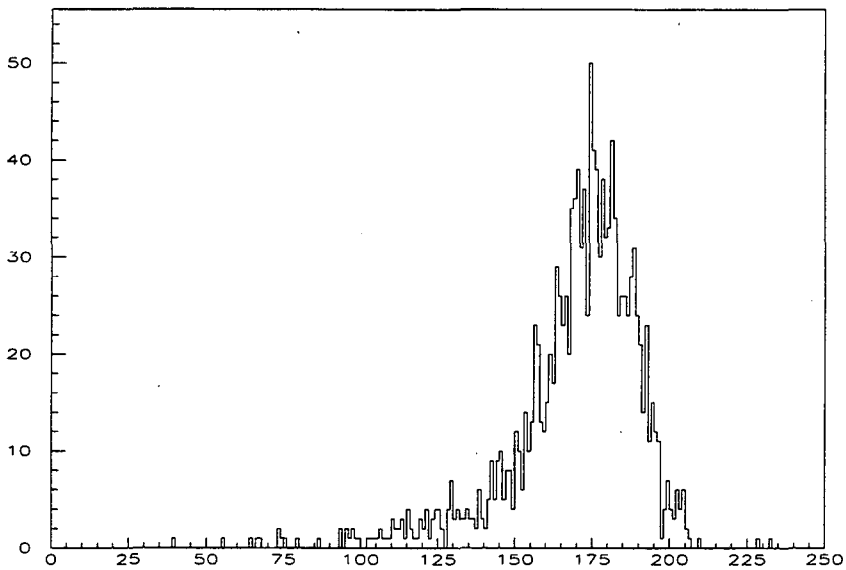

Figure 4.28: Average dielectron trigger ADC distribution (slice-projection from Figure 4.25).

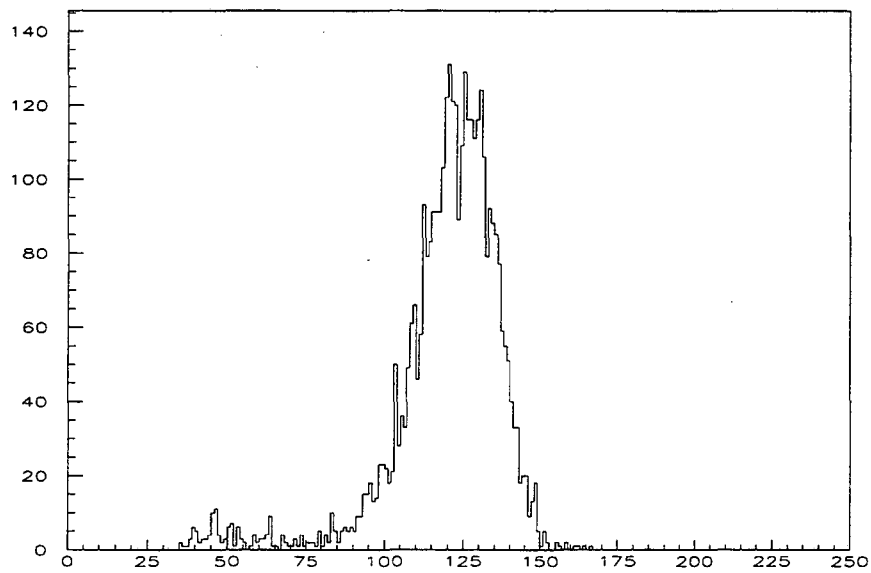

Figure 4.29: Average single-electron trigger ADC distribution (sliced projection from Figure 4.25).

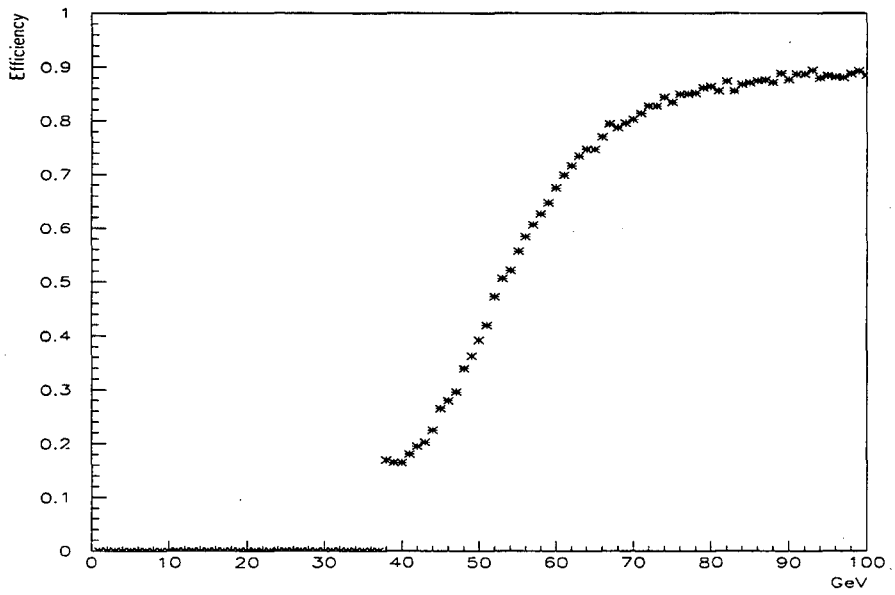

Figure 4.30: Dielectron trigger turn-on as a function of generated D^0 momentum (generated by Monte Carlo).

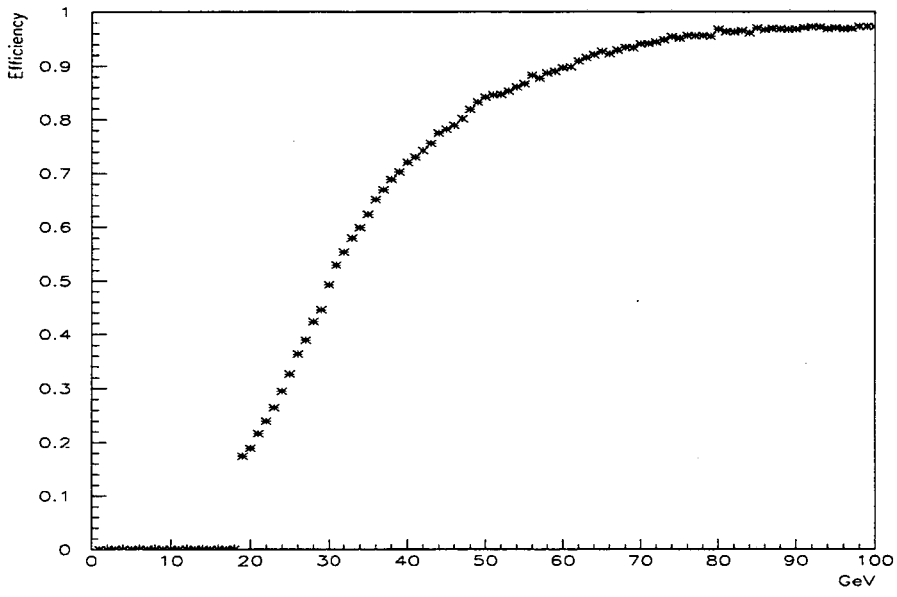

Figure 4.31: Single-electron trigger turn-on vs. generated D^0 momentum. (generated by Monte Carlo).

Chapter 5

Results

With the efficiencies determined, the final data samples for determining the branching ratios were selected. There are two different approaches in measuring the branching ratios, with and without background subtraction. Data sets were selected consistent with each approach. With a calculated branching ratio consistent with zero, upper limits were set at the 90% confidence level. The final upper limit for each dilepton decay was determined by generating a Monte Carlo distribution of the calculated branching ratio associated with each dilepton decay relative to the normalization mode ($D^0 \rightarrow K\pi$). Equation 3.1 combines the components that form the relative branching ratio and is repeated here:

$$\begin{aligned} B(D^0 \rightarrow l^+l^-) &= \frac{N_{l^+l^-}}{\epsilon_{l^+l^-}} \times \frac{\epsilon_{K\pi} \times B(D^0 \rightarrow K\pi)}{N_{K\pi}} \\ &= \frac{B(D^0 \rightarrow K\pi) \times \epsilon \times N_{l^+l^-}}{N_{K\pi}} \end{aligned} \tag{5.1}$$

The efficiencies are discussed in Section 4 and the branching ratio, $B(D^0 \rightarrow K\pi)$, is 0.0395±.0019 [29]. The normalization, $N_{K\pi}$, and the determination of the number of signal events, $N_{l^+l^-}$, are discussed later in this chapter. As will be discussed, two forms of statistical analysis are presented, one incorporating background subtraction in the dilepton invariant mass distribution, and the other without background subtraction.

5.1 Normalization

An event was labeled as a $D^0 \rightarrow K\pi$ candidate if it was reconstructed as a dihadron event, satisfied the dihadron trigger, passed the impact parameter and *lifetime significance* requirements applied to the dilepton decay being studied. There was no mechanism to distinguish the kaon from the pion, in a single event. However, from the Monte Carlo simulation of $D^0 \rightarrow K\pi$ we determined that the invariant mass distribution of the event with the incorrect particle ID assignment was much wider than the one with the correct assignment - 7.1 times as wide for the 900A data sets and 5.4 times wider for the 1000A set (see Figure 4.6). As a result, each event was included twice ($K - \pi$ and $\pi - K$) and the invariant mass distribution was then fit to a quadratic for the background and a double Gaussian for the signal. The standard deviation and normalization were allowed to vary for the narrow Gaussian, while the other was forced to scale according to the relative width as determined in the Monte Carlo simulation. In addition, both Gaussians were required to have the same mean. The number of $D^0 \rightarrow K\pi$ decays was then determined by dividing the area under the narrow Gaussian (associated with the correct particle assignment) by the bin width. The fit was performed using χ^2 minimization by MINUIT [30] from within PAW [31], [32]. The covariance matrix for the width and normalization of the signal Gaussian was then used to find the absolute error associated with the number of reconstructed $D^0 \rightarrow K\pi$ decays. For each dilepton decay mode a different set of impact parameter and *lifetime significance* cuts were used and thus a different normalization was determined. Tables 5.8, 5.9, and 5.10 list the *impact parameter* and *lifetime significance* cuts used for each decay mode and each data set. The tables include the cuts used for both statistical analyses (with and without background subtraction).

5.2 The Branching Ratio

For each dilepton decay mode the three data sets (900A-Au, 900A-Be, and 1000A-Au) were combined and the overall branching ratio is written as

$$B(D^0 \rightarrow l^+l^-) = \frac{\sum_i S_i - G_i}{\sum_i N_i \epsilon_i} \times B(D^0 \rightarrow K\pi) \tag{5.2}$$

where S_i is the number of counts in the signal region, G_i is the number of expected

background counts,[1] ϵ_i is the efficiency of the dilepton decay relative to the normalization, N_i is the normalization ($D^0 \to K\pi$), and $B(D^0 \to K\pi)$ is the branching ratio of $D^0 \to K\pi$, i is summed over each data set.

The Signal Region

Through out this discussion the term *signal region* is used. This refers to the region of the invariant mass distribution over which signal events were counted. The width of the signal region is always specified in relation to the Gaussian distribution that characterizes mass peak associated with the decay hypothesis ($D^0 \to K\pi$, $D^0 \to ee$, $D^0 \to \mu\mu$, or $D^0 \to \mu e$). The width may specified as a number of standard deviations (σ) of the Gaussian or as a percentage of the area under the Gaussian that the signal region subtends. In the analysis with background subtraction an invariant mass window covering 95% of the signal region was used. Without background subtraction, a window covering 90% of the signal region was used. In both cases, the number of reconstructed $D^0 \to K\pi$'s was reduced by the fraction of area the signal region covered.[2]

Without Background Subtraction

In this approach, the search was performed by adjusting the *impact parameter* and *lifetime significance* cuts such that there were no counts in a window 3.28 σ wide (90%). The signal window was determined by using the mean and scaled width of the invariant mass distribution of the normalization signal generated using the same cuts. The width of the invariant mass distribution of the reconstructed dilepton modes was $\sim$ 10% wider than the normalization (as determined by the Monte Carlo, see Table 5.1). The cuts for each of the decay modes in each of the data sets were determined independently. The results for each data set were then combined for the final calculation.

With Background Subtraction

This section discusses how the possibility of background was incorporated into the search. The number of background counts expected in the invariant mass distribution

[1] If the background is not considered, this term is zero.

[2] The reduction in the normalization was proportional to the *fraction* of the signal region used for each dilepton invariant mass distribution. Though the physical region used was $\sim$ 10% wider, this was a more conservative approach.

of each dilepton decay mode was determined by first characterizing the background shape and then integrating the associated function over the signal region. The background was characterized by fitting the invariant mass distribution over a window spanning 1.81 GeV/c^2 to 1.92 GeV/c^2 with a 5.18 σ (99%) region excluded from the fit. The regions on either side of the signal region (sidebands) provided the best information regarding the background behaviour in the signal region. A 3.92 σ (95%) signal region was also designated. Both the fitting and signal regions were centered on the mean of the peak found in $D^0 \rightarrow K\pi$ distribution generated using the same cuts as were applied to the dilepton distribution. The width was set by multiplying the $D^0 \rightarrow K\pi$ width by a scaling factor determined from the Monte Carlo (the width for the dilepton modes was approximately 10% larger than the $D^0 \rightarrow K\pi$, the exact scaling depended on the mode being studied. See Table 5.1 for each relative width). On average, the fit window used was $\sim$ 18 σ wide with the middle 5.16 σ (99% of the signal) excluded from the fit.

The background was fit to a straight line using a binned log likelihood fit. The Poisson nature of the low statistics associated with each bin was accommodated by an iterative procedure. The fit was first performed with equal errors assigned to each bin. The bin errors were then set equal to the square root of the mean of the original fit for each bin after which a second binned log likelihood fit was performed. The number of background counts was then determined by integrating the background function over the signal region and dividing by the bin width. The error on the background was determined using the associated covariance matrix generated by MINUIT [30].

Tables 5.11 through 5.16 list the results of the fits for both the normalization and dilepton[3] invariant mass distributions. Figures 5.1 through 5.9 present the mass distributions for each set of cuts used for each data set and each decay mode. The background fit is displayed if background subtraction was included in the evaluation of the data set for a particular mode.

5.2.1 Systematics

In addition to the statistical errors associated with the fits, various systematic errors also contribute to the branching ratio distribution. Though the systematic error of each quantity is discussed in that section where the value itself is determined (e.g. an effi-

[3] A fit was only done to a dilepton invariant mass distribution if background subtraction was incorporated into the calculation for that distribution.

	$D^0 \to \mu\mu$	$D^0 \to ee$	$D^0 \to \mu e$
900A	1.077	1.09	1.083
1000A	1.085	1.77	1.067

Table 5.1: Relative width of the reconstructed dilepton invariant mass distribution to the normalization, as determined by Monte Carlo.

ciency), the values and their associated errors are compiled here. Note that the systematics reviewed here have little impact on the branching ratio distribution in comparison to the errors associated with the normalization fit parameters or the Poisson nature of the signal and background simulations. Reference [33] discusses the nature of systematics with regard to their effect on an an upper limit calculation. As is discussed in Section 5.2.2, the systematics are included in the Monte Carlo simulation of the branching ratio.

P_t and X_F Variation

As discussed in Section 4.2, the variation of the inputs to the P_t and X_F distributions for the generated D^0 contributed to the relative error in the acceptance. Table 5.2 lists the fractional error for a one σ variation in the inputs.

Decay Mode	P_t	X_F
$D^0 \to \mu\mu$	$\pm.2\%$	$\pm1.5\%$
$D^0 \to ee$	$\pm.9\%$	$\pm2.5\%$
$D^0 \to \mu e$	$\pm.3\%$	$\pm2.2\%$

Table 5.2: Variation in acceptance of each dilepton mode relative to the normalization mode from the error associated with a one σ variation in the input P_t and X_F characterization.

Efficiency and Acceptance

The efficiency and acceptance of each decay mode is listed here. The quantity *Final cut* refers to the fraction of events that survive the most stringent impact parameter and lifetime significance cuts. Though the errors in the *Final cut* and the geometric acceptance are statistical in nature they are listed here. Specifically, the error associated with the

geometric acceptance (rounded up to 0.5%) does not include the variation in the X_F and P_t inputs (which are listed and treated separately). Tables 5.3 through 5.6 list the numbers used to determine the relative efficiency as well as their respective errors. Table 5.7 lists the relative efficiencies for each mode.

$D^0 \to K\pi$

	900A	1000A
Geometric	$3.55 \times 10^{-3} \pm 0.50\%$	$2.37 \times 10^{-3} \pm 0.50\%$
K decays	$0.78 \pm 1.0\%$	$0.82 \pm 1.0\%$
Trigger	$0.55 \pm 1.0\%$	$0.578 \pm 1.0\%$
Final cut	$7.12 \times 10^{-2} \pm 0.50\%$	$9.35 \times 10^{-2} \pm 0.50\%$
Total	$1.09 \times 10^{-4} \pm 1.7 \times 10^{-6}$	$1.05 \times 10^{-4} \pm 1.6 \times 10^{-6}$

Table 5.3: Efficiencies for the $D^0 \to K\pi$ decay.

$D^0 \to \mu\mu$

	900A	1000A
Geometric	$3.97 \times 10^{-3} \pm 0.50\%$	$3.05 \times 10^{-3} \pm 0.50\%$
Trig · (4 of 5) · isolation	$.364 \pm 1.0\%$	$.502 \pm 1.0\%$
Final cut	$7.3 \times 10^{-2} \pm 0.50\%$	$9.85 \times 10^{-2} \pm 0.50\%$
Total	$1.05 \times 10^{-4} \pm 1.5 \times 10^{-6}$	$1.51 \times 10^{-4} \pm 2.1 \times 10^{-6}$

Table 5.4: Efficiencies for the $D^0 \to \mu\mu$ decay.

$D^0 \to ee$

	900A	1000A
Geometric	$3.87 \times 10^{-3} \pm 0.50\%$	$3.28 \times 10^{-3} \pm 0.50\%$
Trigger · ID	$.596 \pm 1.81\%$	$.602 \pm 1.81\%$
Final cut	$7.15 \times 10^{-2} \pm 0.50\%$	$0.10 \pm 0.50\%$
Total	$1.65 \times 10^{-4} \pm 3.2 \times 10^{-6}$	$1.98 \times 10^{-4} \pm 3.87 \times 10^{-6}$

Table 5.5: Efficiencies for $D^0 \to ee$ decay.

$D^0 \to \mu e$

	900A	1000A
Geometric	$4.18 \times 10^{-3} \pm 0.50\%$	$3.42 \times 10^{-3} \pm 0.50\%$
μe (Trig · ID)	$0.362 \pm 3.04\%$	$0.358 \pm 3.04\%$
Final cut	$7.04 \times 10^{-2} \pm 0.50\%$	$0.10 \pm 0.50\%$
Total	$1.06 \times 10^{-4} \pm 3.3 \times 10^{-6}$	$1.28 \times 10^{-4} \pm 4.0 \times 10^{-6}$

Table 5.6: Efficiencies for $D^0 \to \mu e$ decay.

	900A	1000A
$D^0 \to \mu\mu$	0.964±.024	1.44±0.035
$D^0 \to ee$	1.51±.055	1.88±0.069
$D^0 \to \mu e$	.972±.040	1.22±0.050

Table 5.7: Total efficiencies relative to the $D^0 \to K\pi$ decay.

5.2.2 Monte Carlo

The upper limit was determined by using a Monte Carlo program to generate a series of branching ratios distributed according to each of the components of Equation 5.1 and their associated errors. The mean number of counts in the signal region, S_i, was distributed with Poisson statistics. Specifically, S was distributed as

$$\frac{e^{-S}S^M}{M!} \tag{5.3}$$

with M being the actual number of counts seen and S generated according to the probability that M counts were seen given the mean S. N_i, ϵ_i, and $B(D^0 \to K\pi)$ were each Gaussian-distributed according to their errors. As stated above, the mean associated with G_i was Gaussian distributed but G_i itself was distributed as a Poisson distribution with a mean determined by the mean number of background counts (see Section 5.2). A minimum of 10^6 events were generated for each mode.

With the distribution of the branching ratio, an upper limit at 90% confidence is the level at which 90% of the distribution is below. In both analyses, with and without background subtraction, the upper limit presented includes the entire distribution of branching ratios (including the section of the distribution that falls below zero). Without background subtraction the branching ratio was necessarily ≥ 0 as was the upper limit.

However, when background subtraction was considered, the mean of the distribution can fall below zero.[4] If only the positive section of the distribution is used to determine the upper limit, the analysis done without background subtraction will always yield a better result. This is because the presence of background widens the Monte Carlo generated distribution of the branching ratio (the background is also Poisson-distributed). However, if the whole distribution is used, background subtraction may (and most often will) shift the distribution, resulting in a better limit. Though using the positive region may be considered more conservative, the section below zero is no less valid (statistically). References [7], [35], [33], [36], and [37] are commonly cited when the question of setting an upper limit is addressed.

Table 5.17 lists the limits calculated for each decay mode.

$D^0 \rightarrow \mu\mu$

	900A-Au	900A-Be	1000A-Au
	With background subtraction		
Lifetime Significance	1.0	0.90	1.4
Impact Parameter (In)	0.00100	0.00310	0.00375
	Without background subtraction		
Lifetime Significance	1.3	0.90	1.4
Impact Parameter (In)	0.00420	0.00220	0.00415

Table 5.8: *Lifetime Significance* and *impact parameter* cuts for $D^0 \rightarrow \mu\mu$.

$D^0 \rightarrow ee$

	900A-Au	900A-Be	1000A-Au
	With background subtraction		
Lifetime Significance	0.80	0.60	0.80
Impact Parameter (In)	0.00190	0.00115	0.00220
	Without background subtraction		
Lifetime Significance	0.9	0.60	0.80
Impact Parameter (In)	0.00325	0.00115	0.00220

Table 5.9: *Lifetime Significance* and *impact parameter* cuts for $D^0 \rightarrow ee$.

[4]The section of the distribution that is greater than zero is sometimes denoted the *physical region* (see [34]).

$D^0 \to \mu e$

	900A-Au	900A-Be	1000A-Au
	With background subtraction		
Lifetime Significance	1.5	1.0	1.4
Impact Parameter (In)	0.00750	0.00355	0.00220
	Without background subtraction		
Lifetime Significance	1.5	1.0	0.90
Impact Parameter (In)	0.00750	0.00435	0.00355

Table 5.10: *Lifetime Significance* and *impact parameter* cuts for $D^0 \to \mu e$.

Data set	900A-Au	900A-Be	1000A-Au
# of $D^0 \to K\pi$ decays	606. ±56.2	1160. ±110.	971. ±57.1
Mean Mass (GeV/c^2)	1.865 ±.0010	1.863 ±.00079	1.867 ± .00063
Mass Resolution, σ (MeV/c^2)	7.03	5.77	7.32
Normalization of $D^0 \to K\pi$, N	152.5	368.0	235.6
σ-Normalization Covariance			
$\sigma - \sigma$	192.0	1040.	192.0
σ-N	-0.008160	-0.01380	-0.004930
N-N	0.7710×10^{-6}	0.4610×10^{-6}	0.3060×10^{-6}

Table 5.11: $D^0 \to K\pi$ fit parameters for the $D^0 \to \mu\mu$ search, without background subtraction.

Data set	900A-Au	900A-Be	1000A-Au
# of $D^0 \to K\pi$ decays	707. ±91.0	1563. ±154.	1749. ±129.
Mean Mass (GeV/c^2)	1.865 ±0.0012	1.863 ±0.00085	1.866 ±0.00078
Mass Resolution, σ (MeV/c^2)	6.20	5.92	6.39
Normalization of $D^0 \to K\pi$, N	203.9	470.1	477.4
σ-Normalization Covariance			
$\sigma - \sigma$	609.0	1770.	1120.0
σ-N	-0.01670	-0.01940	-0.01230
N-N	0.1080×10^{-5}	0.5450×10^{-6}	0.3580×10^{-6}

Table 5.12: $D^0 \to K\pi$ fit parameters for the $D^0 \to ee$ search, without background subtraction.

Data set	900A-Au	900A-Be	1000A-Au
# of $D^0 \to K\pi$ decays	255. ±21.0	967. ±61.7	1429. ±84.1
Mean Mass (GeV/c^2)	1.865 ±0.00074	1.864 ±0.00060	1.867 ±0.00062
Mass Resolution, σ (MeV/c^2)	6.04	6.61	7.05
Normalization of $D^0 \to K\pi$, N	75.03	263.0	358.9
σ-Normalization Covariance			
$\sigma - \sigma$	38.90	268.0.	421.0
σ-N	-0.002400	-0.005640	-0.006790
N-N	0.3780×10^{-6}	0.2880×10^{-6}	0.2770×10^{-6}

Table 5.13: $D^0 \to K\pi$ fit parameters for the $D^0 \to \mu e$ search, without background subtraction.

Data set	900A-Au	900A-Be	1000A-Au
# of signal counts	2	0	0
Mean of background	3.13 ±0.793	246.30 ±0.441	X
χ^2 of background fit /25 df	1.41	1.16	X
# of $D^0 \to K\pi$ decays	844. ±123.	1182. ±102.	1014. ±65.8.
Mean Mass (GeV/c^2)	1.864 ±0.0015	1.863 ±0.00076	1.867 ±0.00072
Mass Resolution, σ (MeV/c^2)	5.55	5.92	7.27
Normalization of $D^0 \to K\pi$, N	252.1	351.5	230.5
σ-Normalization Covariance			
$\sigma - \sigma$	1200.	792.0	221.0
σ-N	-0.02230	-0.01280	-0.005910
N-N	0.1080×10^{-5}	0.4440×10^{-6}	0.3820×10^{-6}

Table 5.14: Signal and $D^0 \to K\pi$ fit parameters for the $D^0 \to \mu\mu$ search, including background subtraction.

Data set	900A-Au	900A-Be	1000A-Au
# of signal counts	0	0	0
Mean of background	2.05 ±0.613	X	X
χ^2 of background fit /25 df	0.89	X	X
# of $D^0 \to K\pi$ decays	717. ±140.	1649. ±162.	1847. ±136.
Mean Mass (GeV/c^2)	1.864 ±0.0018	1.863 ±0.00085	1.866 ±0.00078
Mass Resolution, σ (MeV/c^2)	5.04	5.92	6.39
Normalization of $D^0 \to K\pi$, N	235.5	470.1	477.4
σ-Normalization Covariance			
$\sigma - \sigma$	1750.	1770.	1120.
σ-N	-0.03870	-0.01940	-0.01230
N-N	0.1850×10^{-5}	0.5450×10^{-6}	0.3580×10^{-6}

Table 5.15: Signal and $D^0 \to K\pi$ fit parameters for the $D^0 \to ee$ search, including background subtraction.

Data set	900A-Au	900A-Be	1000A-Au
# of signal counts	0	1	0
Mean of background	X	2.95 ±0.607	X
χ^2 of background fit /25 df	X	0.9278	X
# of $D^0 \to K\pi$ decays	269. ±22.0	1182. ±90.5	1412. ±103.
Mean Mass (GeV/c^2)	1.864 ±0.00075	1.863 ±0.00075	1.866 ±0.00097
Mass Resolution, σ (MeV/c^2)	5.04	5.92	6.39
Normalization of $D^0 \to K\pi$, N	75.03	295.0	290.9
σ-Normalization Covariance			
$\sigma - \sigma$	38.90	467.0	425.0
σ-N	-0.002400	-0.01040	-0.01070
N-N	0.3780×10^{-6}	0.4670×10^{-6}	0.6170×10^{-6}

Table 5.16: Signal and $D^0 \to K\pi$ fit parameters for the $D^0 \to \mu e$ search, including background subtraction.

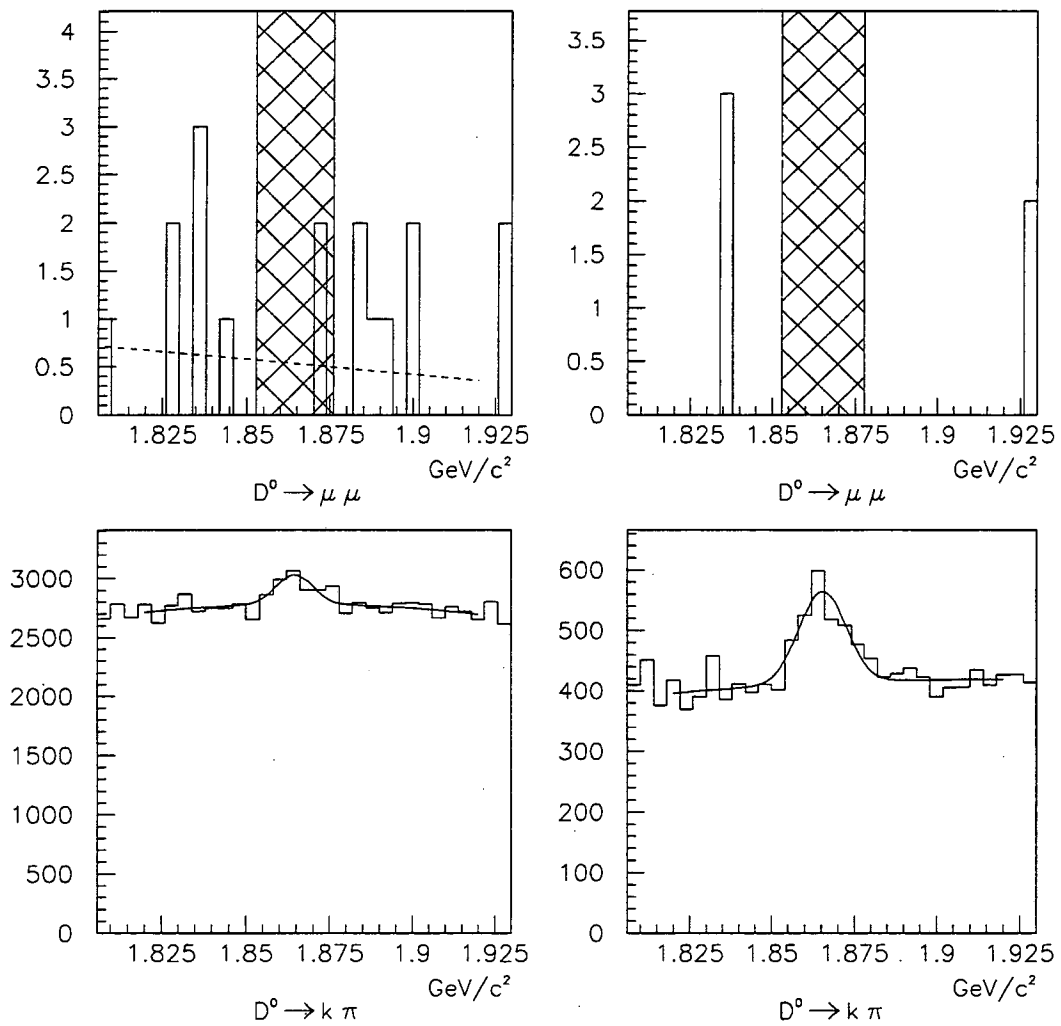

Figure 5.1: Invariant mass distributions for $D^0 \to \mu\mu$ and its associated $D^0 \to K\pi$ distribution for the 900A-Au data set. Distributions on the left are used for the analysis incorporating background subtraction and those on the right are used when background subtraction was not considered. The dashed line is the background fit. The cross-hatched area marks the signal region.

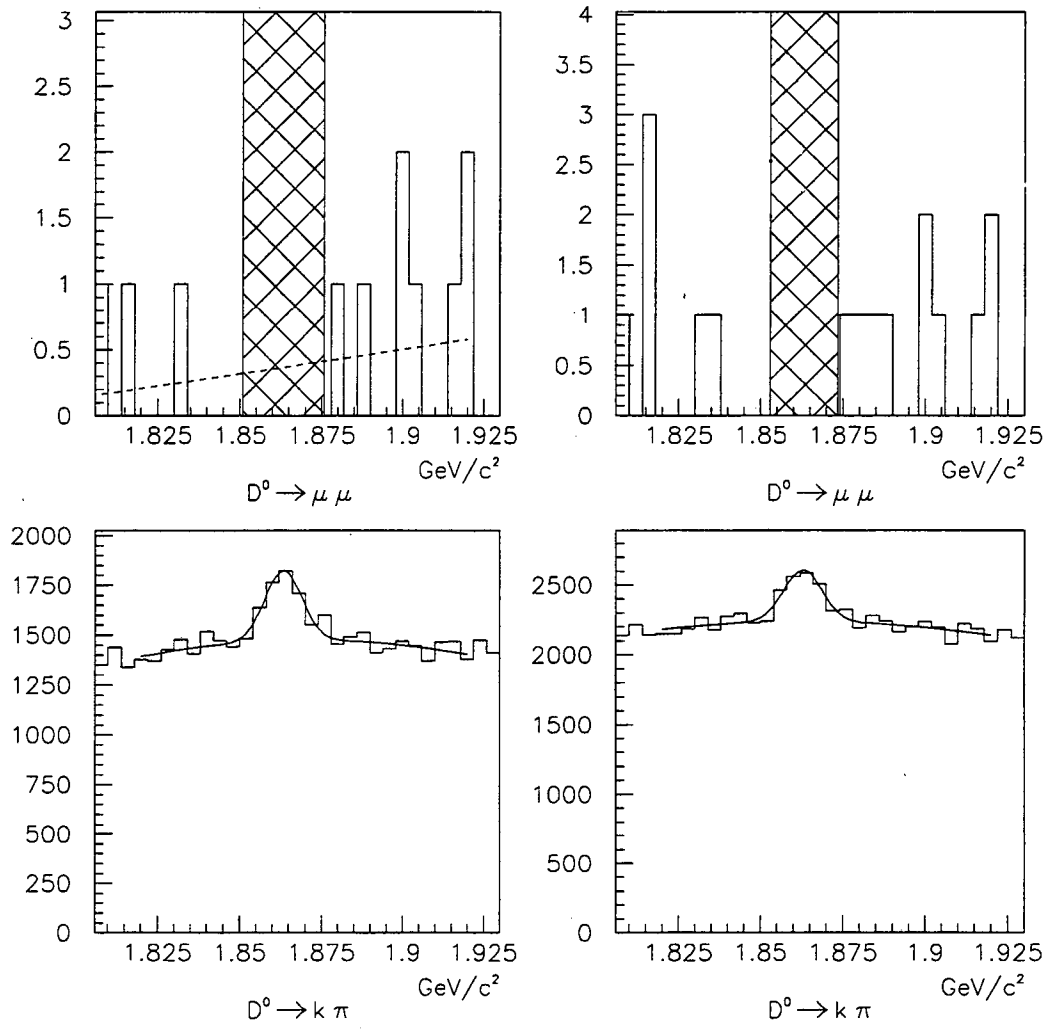

Figure 5.2: Invariant mass distribution for $D^0 \to \mu\mu$ and its associated $D^0 \to K\pi$ distribution for the 900A-Be data set. Distributions on the left are used for the analysis incorporating background subtraction and those on the right are used when background subtraction was not considered. The dashed line is the background fit. The cross-hatched area marks the signal region.

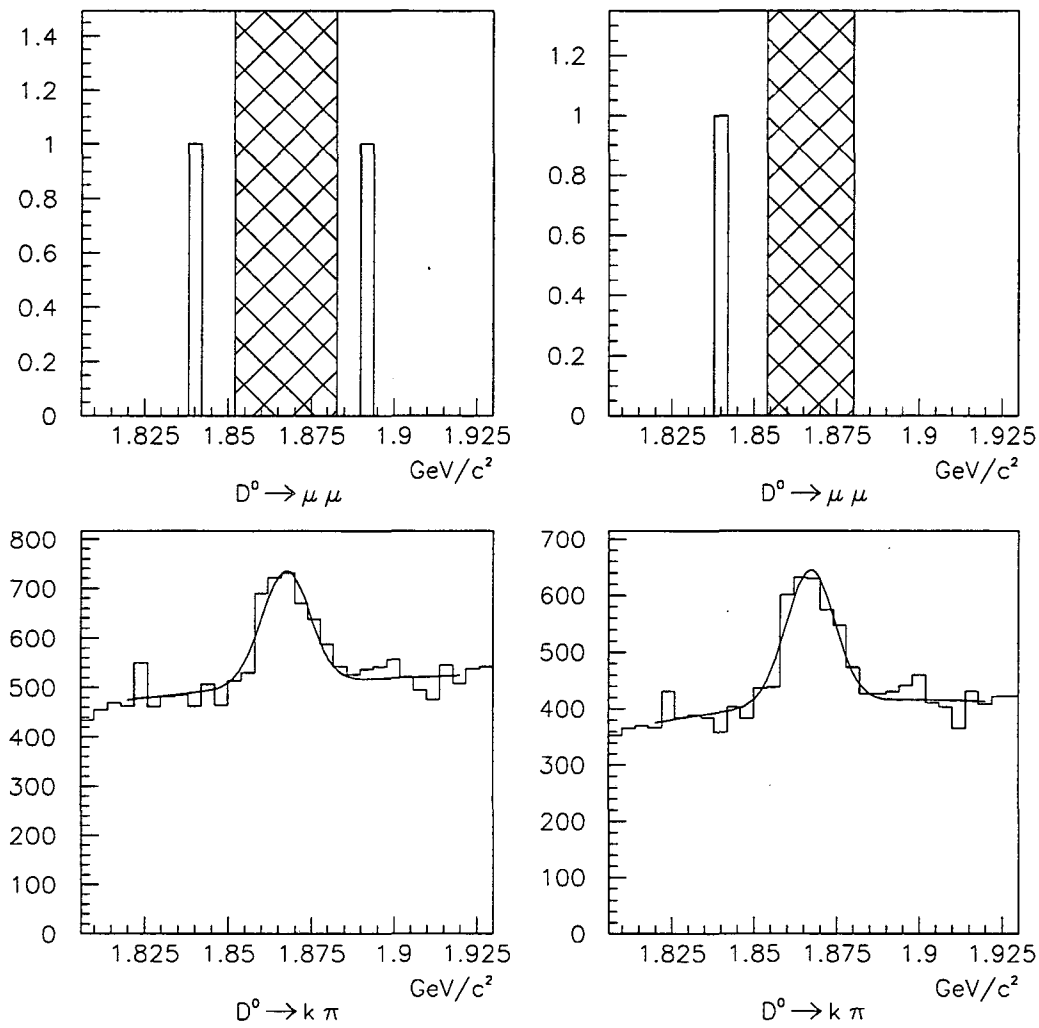

Figure 5.3: Invariant mass distribution for $D^0 \to \mu\mu$ and its associated $D^0 \to K\pi$ distribution for the 1000A-Au data set. Distributions on the left are used for the analysis incorporating background subtraction and those on the right are used when background subtraction was not considered. The cross-hatched area marks the signal region.

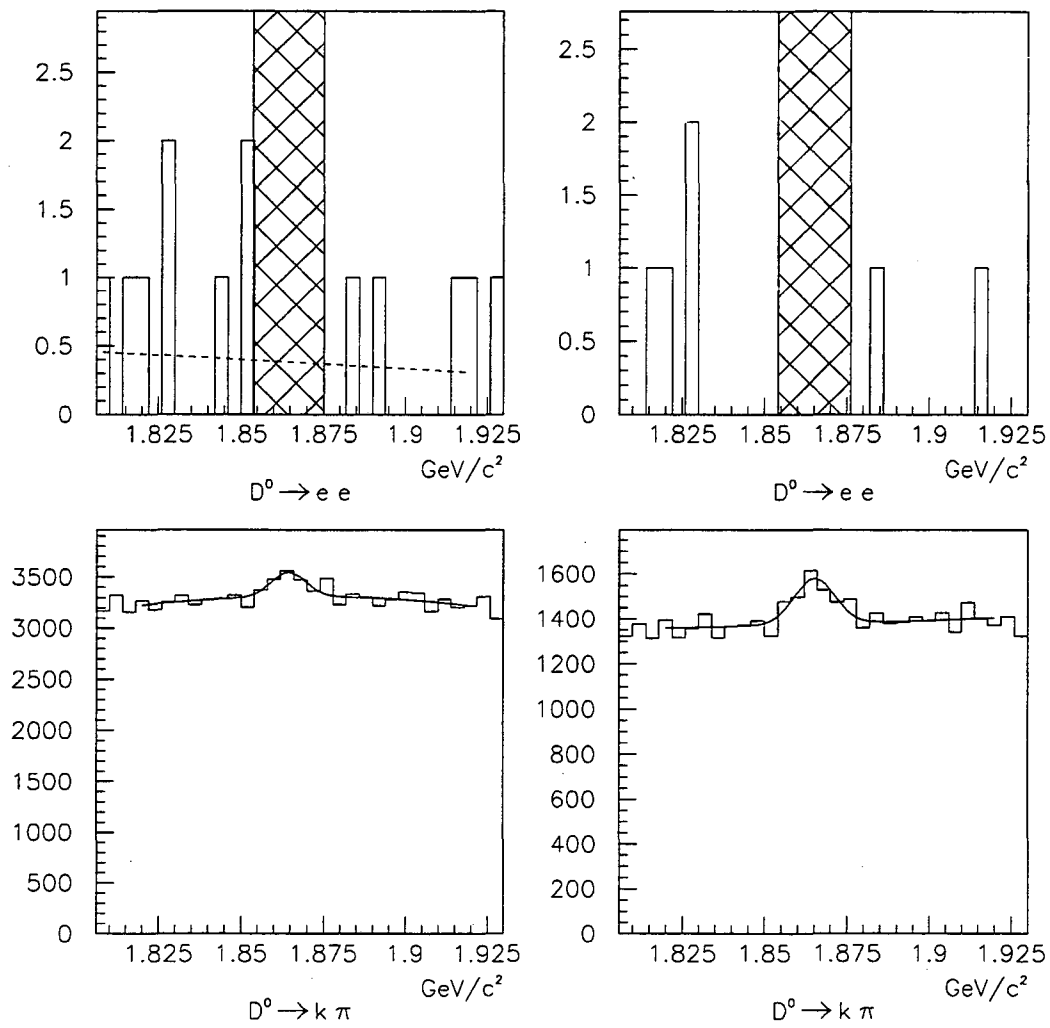

Figure 5.4: Invariant mass distribution for $D^0 \rightarrow ee$ and its associated $D^0 \rightarrow K\pi$ distribution for the 900A-Au data set. Distributions on the left are used for the analysis incorporating background subtraction and those on the right are used when background subtraction was not considered. The dashed line is the background fit. The cross-hatched area marks the signal region.

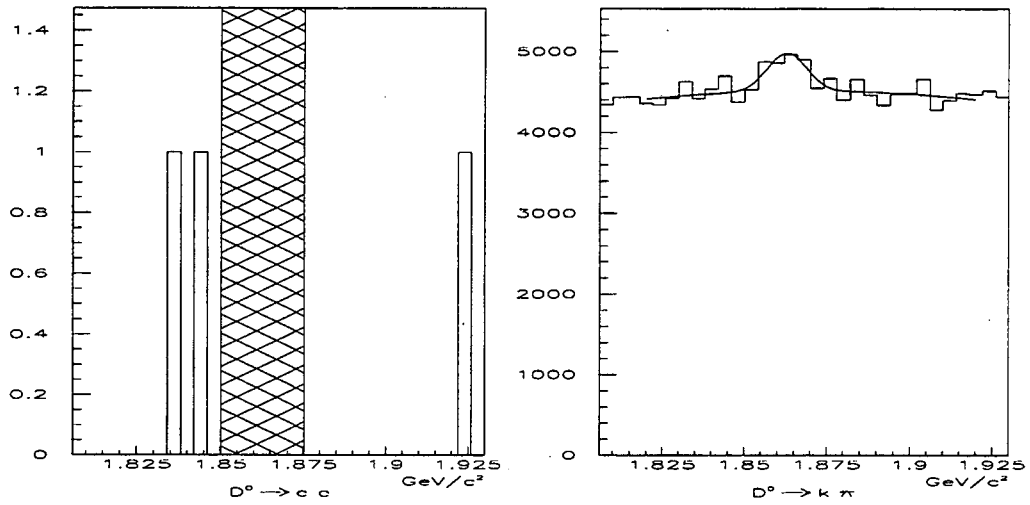

Figure 5.5: Invariant mass distribution for $D^0 \rightarrow ee$ and its associated $D^0 \rightarrow K\pi$ distribution for the 900A-Be data set. The same cuts and thus, the same distributions, were used for the analysis with and without background subtraction. The cross-hatched area marks the wider of the two signal regions (3.92 σ, or 95% probability).

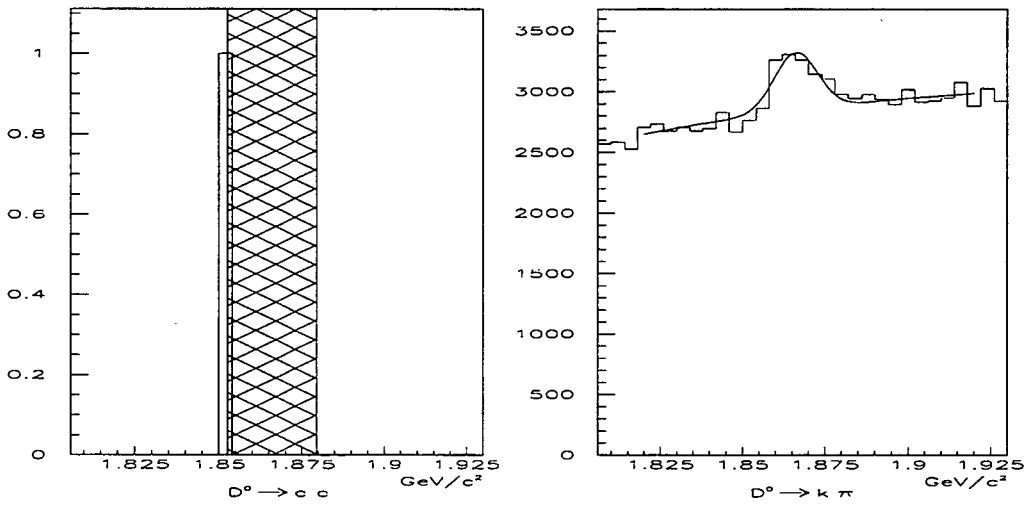

Figure 5.6: Invariant mass distribution for $D^0 \rightarrow ee$ and its associated $D^0 \rightarrow K\pi$ distribution for the 1000A-Au data set. The same cuts and thus, the same distributions, were used for the analysis with and without background subtraction. The cross-hatched area marks the wider of the two signal regions (3.92 σ, or 95% probability).

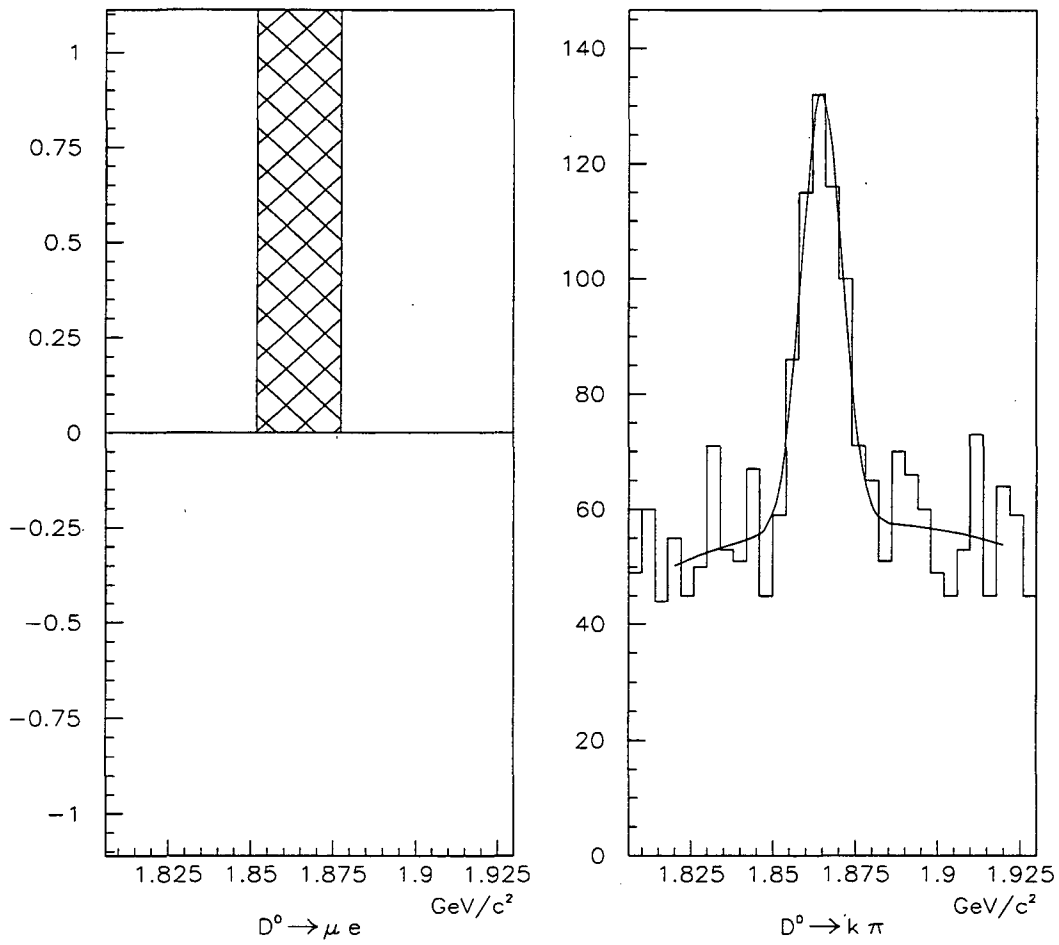

Figure 5.7: Invariant mass distribution for $D^0 \rightarrow \mu e$ and its associated $D^0 \rightarrow K\pi$ distribution for the 900A-Au data set. The same cuts and thus, the same distributions, were used for the analysis with and without background subtraction. The cross-hatched area marks the wider of the two signal regions (3.92 σ, or 95% probability).

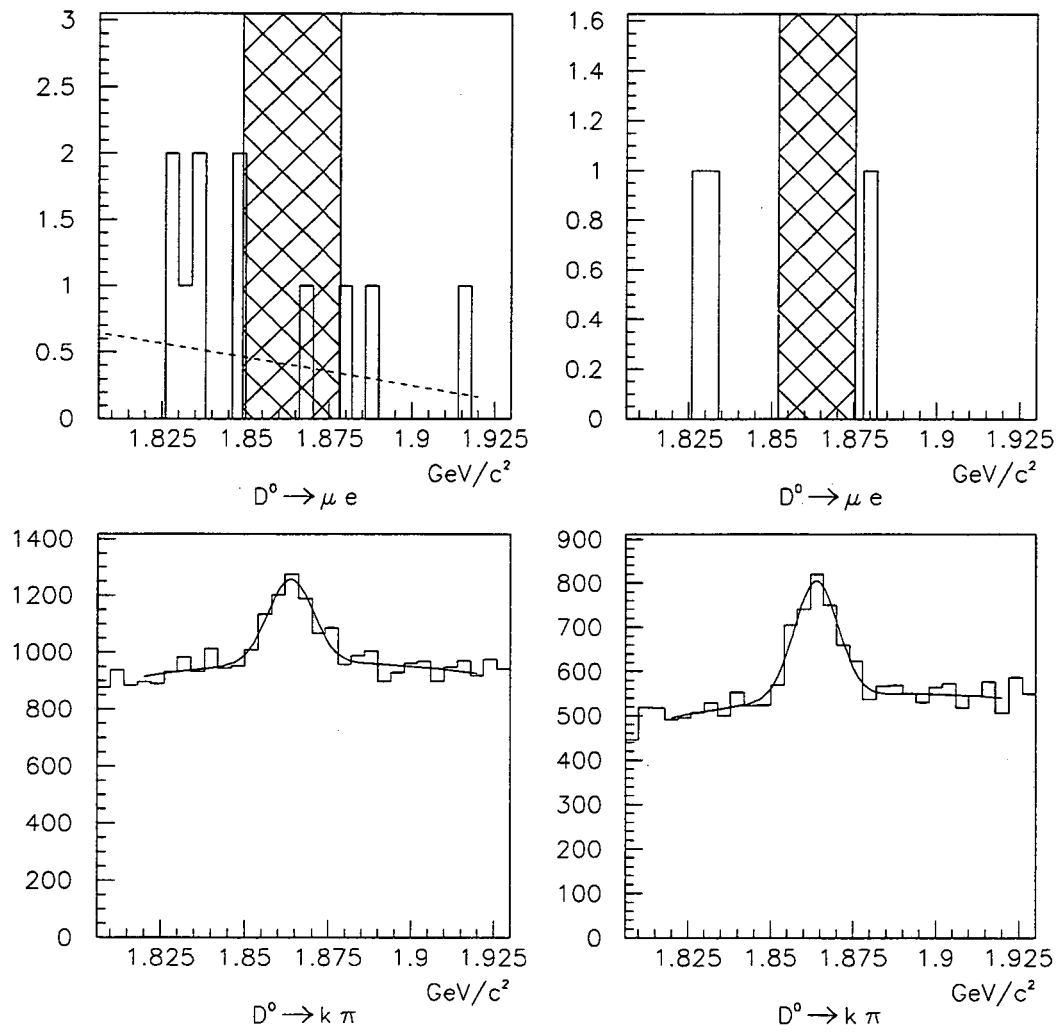

Figure 5.8: Invariant mass distribution for $D^0 \to \mu e$ and its associated $D^0 \to K\pi$ distribution for the 900A-Be data set. Distributions on the left are used for the analysis incorporating background subtraction and those on the right are used when background subtraction was not considered. The dashed line is the background it. The cross-hatched area marks the signal region.

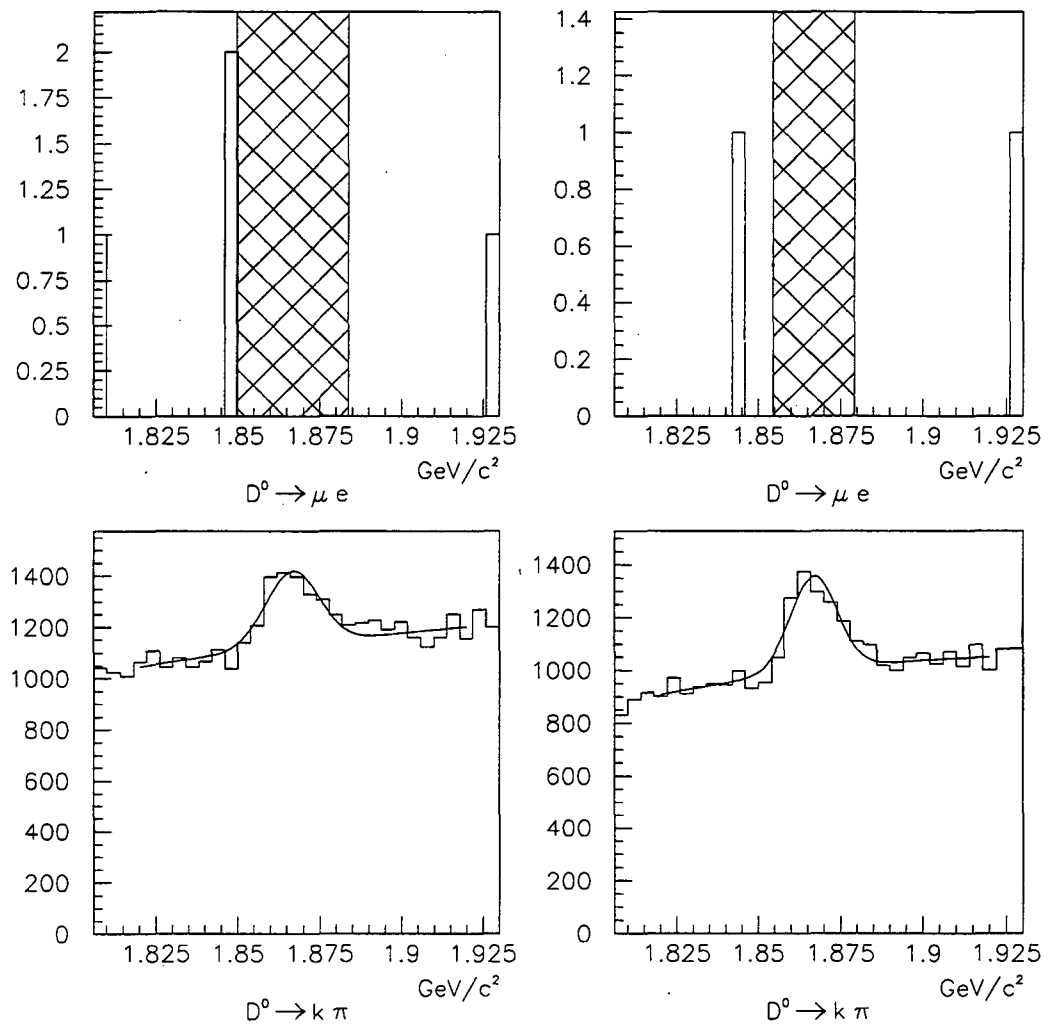

Figure 5.9: Invariant mass distribution for $D^0 \to \mu e$ and its associated $D^0 \to K\pi$ distribution for the 1000A-Au data set. Distributions on the left are used for the analysis incorporating background subtraction and those on the right are used when background subtraction was not considered. The cross-hatched area marks the signal region.

	Without background subtraction	With background subtraction
$D^0 \to \mu\mu$	2.85×10^{-5}	1.56×10^{-5}
$D^0 \to ee$	1.34×10^{-5}	6.05×10^{-6}
$D^0 \to \mu e$	3.07×10^{-5}	2.35×10^{-5}

Table 5.17: Limits set at the 90% confidence limit.

Chapter 6

Conclusions

With a Silicon Strip Detector, a tailored trigger, and an upgraded DAQ, Experiment E789 has demonstrated its effectiveness at recording and identifying two-body Charm decays. The Calorimeter and Muon Station were used to efficiently characterize electrons, hadrons, and muons. Three rare/forbidden decays, $D^0 \to \mu\mu$, $D^0 \to ee$, and $D^0 \to \mu e$ have been searched for and new upper limits have been determined. The upper limits are presented in Table 6.1. For each decay mode, two limits are presented: one with, and one without background subtraction in the procedure.

	This Experiment		World's Best Limit
	Without bckgrnd subtr.	With bckgrnd subtr.	
$D^0 \to \mu\mu$	2.85×10^{-5}	1.56×10^{-5}	4.2×10^{-6}
$D^0 \to ee$	1.34×10^{-5}	6.05×10^{-6}	1.3×10^{-5}
$D^0 \to \mu e$	3.07×10^{-5}	2.35×10^{-5}	1.9×10^{-5}

Table 6.1: Limits set at the 90% confidence level.

The measurement was based on three of the four available data sets. The different trigger configuration of the dilepton data set will require some further analysis. Preliminary studies suggested that including this data set will improve the limit by 30-50%.

The fundamental limitation of this search is luminosity. This is the case in most current searches for rare or forbidden two-body decays in the Charm sector. Despite this limitation, the results from this analysis are comparable to other similar searches. For example, the best searches for flavor changing neutral currents or lepton family number vi-

olations in D^0 meson decays have come, or are expected, from the CLEO Collaboration [38]. Their current limits are based on data collected with the CLEO II detector at the Cornell e^+e^- Storage Ring (CESR). The CLEO II detector [39] is a solenoidal detector with 67 tracking layers and a CsI electromagnetic calorimeter. They can search for a variety of $D^0 \rightarrow l^+l^-$ and $D^0 \rightarrow Xl^+l^-$ decays. The D^0 candidates comes from $D^{*+} \rightarrow D^0\pi^+$ decays. The decay $D^0 \rightarrow K\pi$ is used to normalize the measurement. As a result, the analysis of the dilepton decay modes are compared to a normalization mode with very similar kinematics.[1] The CsI calorimeter allows for efficient electron identification as well as π^0 identification. Muons can also be identified. With lab frame identical to the center of mass frame, the D^0 typically does not decay far from the production vertex (unlike Experiment E789). However, with good mass resolution, particle identification (including kaons and pions), and the requirement that the D^0 come from $D^{*+} \rightarrow D^0\pi^+$, the background in the signal region is small or non-existent. The large integrated luminosity (3.85 fb^{-1} at the $\Upsilon(4S)$ resonance), allows for the excellent limits listed in Table 6.2 (only the three decays that were studied in this analysis are listed for comparison). [38]

Decay mode	$D^0 \rightarrow ee$	$D^0 \rightarrow \mu\mu$	$D^0 \rightarrow \mu e$
Limit (90% C. L.)$\times 10^{-5}$	1.3	3.4	1.9

Table 6.2: Current $D^0 \rightarrow$ *dilepton* limits from CLEO (90% confidence limit).

Experiment E771 yielded the best published limit for the decay $D^0 \rightarrow \mu\mu$ [40]. Like experiment E789, E771 was designed primarily to study B meson production. Their primary focus was to record B mesons whose decay included a J/ψ decaying to two muons. As a result, they were also able to search for the decay $D^0 \rightarrow \mu\mu$. E771 used an open geometry large acceptance spectrometer which was capable of reconstructing events with an invariant mass that spanned from less than the mass of the ρ^0 to beyond the mass of the $\psi(2S)$ (The range spanned from $\sim 0.5\ GeV/c^2$ to $\sim 4.0\ GeV/c^2$). In addition to the tracking chambers and bend magnets, the E771 included an electromagnetic calorimeter, a muon station, and a silicon micro-strip vertex detector (SMVD). E771 presented a reconstructed invariant mass peak at the ρ^0/ω, ϕ, J/ψ, and ψ(2S) mass. However, E771 had no $D^0 \rightarrow K\pi$ signal against which its dimuon signal could be compared. The E771 collaboration determined its

[1]The analysis presented in this thesis also utilizes the same $D^0 \rightarrow K\pi$ normalization mode.

limit for $D^0 \to \mu\mu$ using their measured luminosity and calculated acceptance efficiencies. In addition to the complexities associated with calculating the absolute efficiencies,[2] the absence of any mass peak based on the downstream decay vertex (the crux of their $D^0 \to \mu\mu$ search) makes their analysis a difficult one. In this sense the E771 analysis differs from that of CLEO and this analysis. E771 presented a limit on the branching ratio for the decay $D^0 \to \mu\mu$, at the 90% confidence level, of 4.2×10^{-6}.

The best search for $D^0 \to$ *dilepton* decays in the near future will be from the CLEO collaboration. With ever increasing luminosity and enhanced sensitivity, CLEO will reach levels below any current experiments ($10^{-6} - 10^{-7}$).

In the first years of the next century, with the expected turn on of the Tau/Charm factory and further contributions from e^+e^- colliders [41] combined with the LHC-B Charm physics effort (included in the LHC-B Beauty physics program [42]), it seems the future will come from the collider experiments. However, Kaplan [43, 44, 45] presented compelling arguments for, and specific considerations of, a future dedicated fixed target program for Charm physics which could bring an additional four orders of magnitude improvement beyond the current limits.[3]

The current upper limits are still many orders of magnitude away from the levels at which the Standard Model predicts they might occur. As a result, the *window* for new physics remains large[4] and the prospect of using the Charm sector to test the Standard Model remains interesting and challenging.

[2]The efficiency calculations depend a great deal on Monte Carlo simulations.

[3]These references also provide a nice comparison of the various competing and complementary Charm physics efforts for the next decade and beyond.

[4]There may never be a single experiment whose sensitivity reaches the Standard Model level for the two-body $D^0 \to$ *dilepton* decays.

Bibliography

[1] S. Pakvasa, Chin. J. Phys. **32**, 1163 (1994).

[2] S. Weinberg, Phys. Rev. Lett. **19**, 1264 (1967).

[3] A. Salam, Originally printed in *Svartholm: Elementary Particle Theory, Proceedings Of The Nobel Symposium Held 1968 At Lerum, Sweden*, Stockholm 1968, p. 367-377.

[4] M. Gell-Mann, Phys. Lett. **8**, 214 (1964).

[5] G. Zweig, CERN Preprint, CERN-TH-412 (1964).

[6] Ford *et al.*, Phys. Rev. Lett. **18**, 1214 (1967).

[7] Particle Data Group, Phys. Rev. **D54** (1996).

[8] S. L. Glashow, J. Iliopoulos, and L. Maiani, Phys. Rev. **D2**, 1285 (1970).

[9] M. K. Gaillard and B. W. Lee, Phys. Rev. **D10**, 897 (1974).

[10] J. J. Aubert *et al.*, Phys. Rev. Lett. **33**, 1404 (1974).

[11] J. E. Augustin *et al.*, Phys. Rev. Lett. **33**, 1406 (1974).

[12] G. Goldhaber *et al.*, Phys. Rev. Lett. **37**, 255 (1976).

[13] C. Rubbia, in, Proc 17th Int. Conf. on High Energy Physics, London (Rutherford Appleton Laboratory), 1974, p. 117-120.

[14] H. Deden *et al.*, Phys. Lett. **58B**, 361 (1975).

[15] S. P. K. Tavernier, Rept. Prog. Phys. **50**, 1439 (1987).

[16] P. Depommier and C. Leroy, Rept. Prog. Phys. **58**, 61 (1995).

[17] Arisaka *et al.*, Phys. Rev. Lett. **70**, 1049 (1993).

[18] R. D. Bolton *et al.*, Phys. Rev. **D38**, 2077 (1988).

[19] F. Halzen and A. D. Martin, *Quarks And Leptons: An Introductory Course In Modern Particle Physics* (John Wiley & Sons, Inc., New York, USA, 1984).

[20] W. Buchmuller and D. Wyler, Phys. Lett. **177B**, 377 (1986).

[21] K. S. Babu, X. G. He, X. Li, and S. Pakvasa, Phys. Lett. **205B**, 540 (1988).

[22] A. Acker and S. Pakvasa, Mod. Phys. Lett. **A7**, 1219 (1992).

[23] J. O. Eeg, Z. Phys. **C46**, 665 (1990).

[24] S. Misawa, *A Search for Charmless Dihadron Decays of Neutral b-Hadrons*, PhD thesis, University of California at Berkeley, 1997.

[25] Y.-C. Chen, *Measurement of B meson production cross section in 800* GeV/c *proton-nucleus interaction*, PhD thesis, National Cheng Kung University, 1993.

[26] M. Kowitt, *Hadronic Production of J/ψ at Large x_f in 800 GeV p+Cu and p+Be Collisions*, PhD thesis, University of California at Berkeley, 1992.

[27] Schub *et al.*, Nucl. Instrum. Meth. **A376**, 49 (1996).

[28] Fermilab E653, K. Kodama *et al.*, Phys. Lett. **B263**, 573 (1991).

[29] CLEO, D. S. Akerib *et al.*, Phys. Rev. Lett. **71**, 3070 (1993).

[30] F. James *et al.*, CERN Program Library Long Writeup D506, *MINUIT* Release 94.09 (1994).

[31] R. Brun *et al.*, CERN Program Library Q121, *PAW* version 2.05/17 (1994).

[32] R. Brun *et al.*, HBOOK, *CERN Program Library Long Writeup Y250, Version 4.22*, CERN, 1994.

[33] R. D. Cousins and V. L. Highland, Nucl. Instr. Meth. **A320**, 331 (1992).

[34] L. Lyons, *Statistics For Nuclear And Particle Physicists* (Cambridge, UK: University Press, 1986), p. 78-80.

[35] O. Helene, Nucl. Instr. Meth. **212**, 319 (1983).

[36] H. B. Prosper, Nucl. Instrum. Meth. **A241**, 236 (1986).

[37] H. B. Prosper, Phys. Rev. **D37**, 1153 (1988).

[38] CLEO, A. Freyberger *et al.*, Phys. Rev. Lett. **76**, 3065 (1996).

[39] Y. Kubota *et al.*, Nucl. Instrum. Meth. **A320**, 66 (1992).

[40] E771, T. Alexopoulos *et al.*, Phys. Rev. Lett. **77**, 2380 (1996).

[41] D. Z. Besson and A. P. Freyberger, in *The Future of High-Sensitivity Charm Experiments.* Proc. CHARM2000 Workshop, Batavia, Ill., June 7-9. D. M. Kaplan and S. Kwan, eds. FERMILAB-Conf-94/190 (1994), p. 35.

[42] LHC-B, D. Websdale, Nucl. Phys. Proc. Suppl. **50**, 333 (1996).

[43] C0 Charm, D. M. Kaplan *et al.*, Presented at 3rd German-Russian Workshop on Progress in Heavy Quark Physics, Dubna, Russia, 20-22 May 1996.

[44] D. M. Kaplan, Nucl. Phys. Proc. Suppl. **50**, 260 (1996), hep-ex/9512002.

[45] D. M. Kaplan (ed.) and S. Kwan (ed.), The Future of High Sensitivity Charm Experiments. Proceedings, CHARM2000 Workshop, Batavia, Ill., June 7-9, 1994.

[46] T. R. C. Peterson and L. Lönnblad, Comp. Phys. Comm. **81**, 185 (1994).

Appendix A

Neural Net

To reduce the number of background events, a neural net was implemented. The neural net was selected to utilize the dependent nature of the variables. Rather than selecting events based on cuts associated with each variable independently, a figure of merit could be assigned to each event. The figure of merit was a single variable generated as a function of all of the cut-variables. In the end it turned out that, though the neural net was adequate to reject much of the noise and indeed did yield a normalization signal, the best enhancements came from simply setting cuts on each variable. The Net was used in the analysis and is described here.[1]

When each event was processed, the SSD track reconstruction algorithm yielded a set of potential vertices each consisting of two SSD tracks that masked to oppositely charged downstream tracks. The problem of selecting the correct vertex was addressed by allowing a neural net algorithm to select the vertex which, after passing loose quality cuts, had the highest likelihood of being the result of a D^0 decaying into two particles. The neural net package used was The Lund Neural Network Program - Jetnet 3.2 [46]. The Net algorithm assigned a probability to a vertex based on the input variables chosen to distinguish best between a signal decay vertex and those vertices from noise processes. The variables used for vertex selection were the z-position of the vertex, the impact parameter of each track in the y-z plane with respect to the target center, and the difference between the impact parameters. In addition, the relativistic kinematic variable γ and the decay distance divided by $\gamma\beta c\tau$, *lifetime significance* were included. The *lifetime significance* was calculated assuming the parent was a D^0 . To train the Net to recognize a signal decay,

[1]The neural net was only used for the preliminary data reduction (see Section 3.2.2).

the Net was fed with variables from properly reconstructed $D^0 \rightarrow K\pi$ events generated by the Monte Carlo program. These events were contrasted with noise events chosen from real data at random. The noise events had to include a vertex and had to have a reconstructed two-body invariant mass that fell within the 500 MeV/c^2 mass window about the nominal D^0 mass (1864.5 MeV/c^2 [7]). For a given vertex, the trained Net could assign a probability based on the same variables used in the training process. Figure A.1 is a comparison of the probability distributions for genuine Monte Carlo $D^0 \rightarrow K\pi$ decays and for noise events from data. It is obvious that the noise events have very different characteristics. In addition to selecting between vertices, an overall probability of greater than 0.3 was required in Pass 2 both to enhance the data reduction and maintaining yield. In Pass 3 which included a different SSD alignment and thus needed a new Net, a cut of probability greater than 0.4 was used for further data reduction. The cut was selected by simply looking at the output distributions for noise events and signal events. A cut was chosen such that eliminated the bulk of the noise while maintaining as much of the signal as possible. The following series of histograms, Figures A.2 through A.6, characterize the performance of the net with respect to the variables on which it was trained. For each variable real events are presented with and without a cut on the neural net and are compared to properly reconstructed Monte Carlo D^0 decays. In general the comparisons demonstrate the ability of the Neural Net to remove events not consistent with the training data set (Monte Carlo).

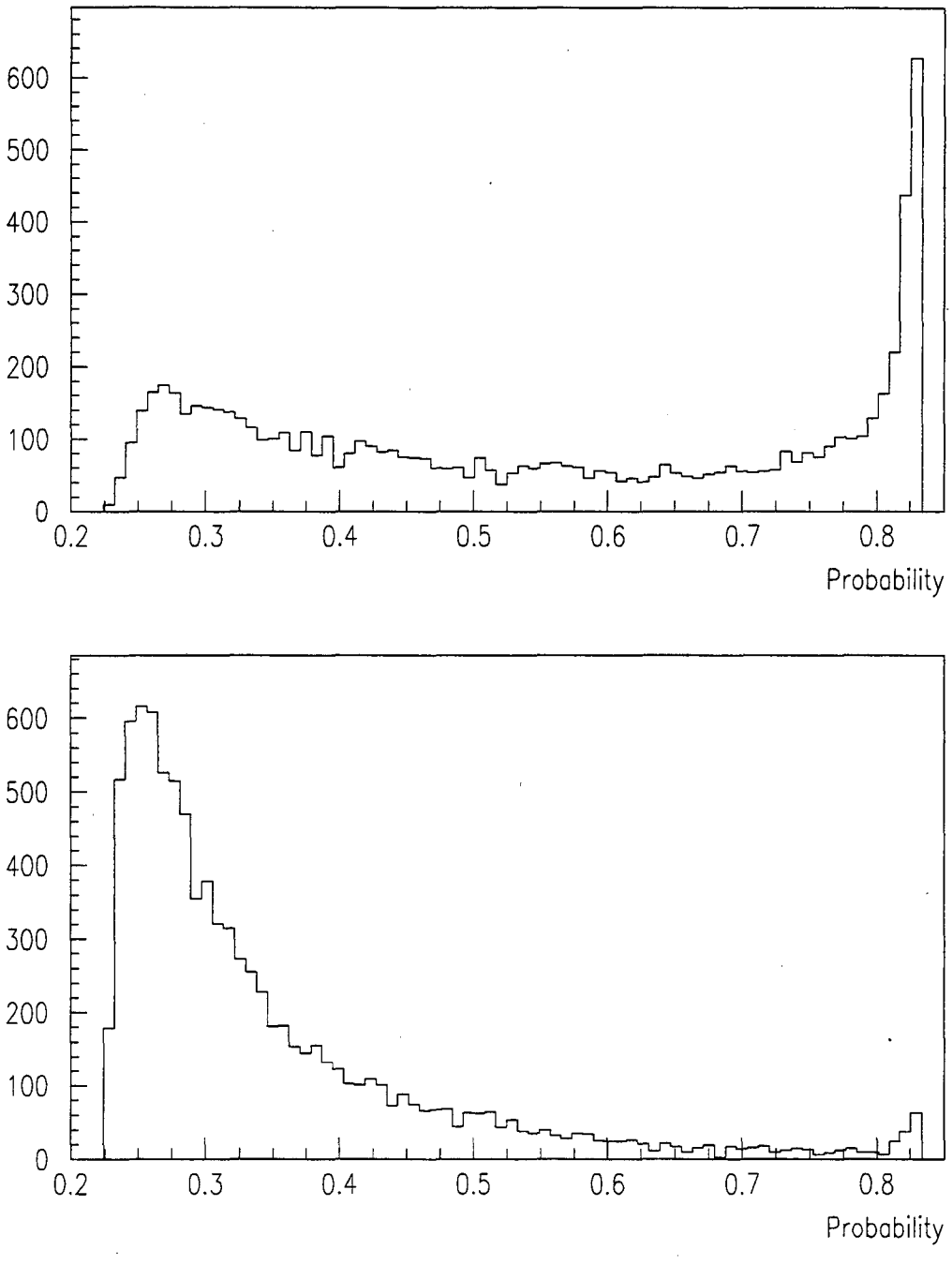

Figure A.1: Event characterization, output of the Neural Net.

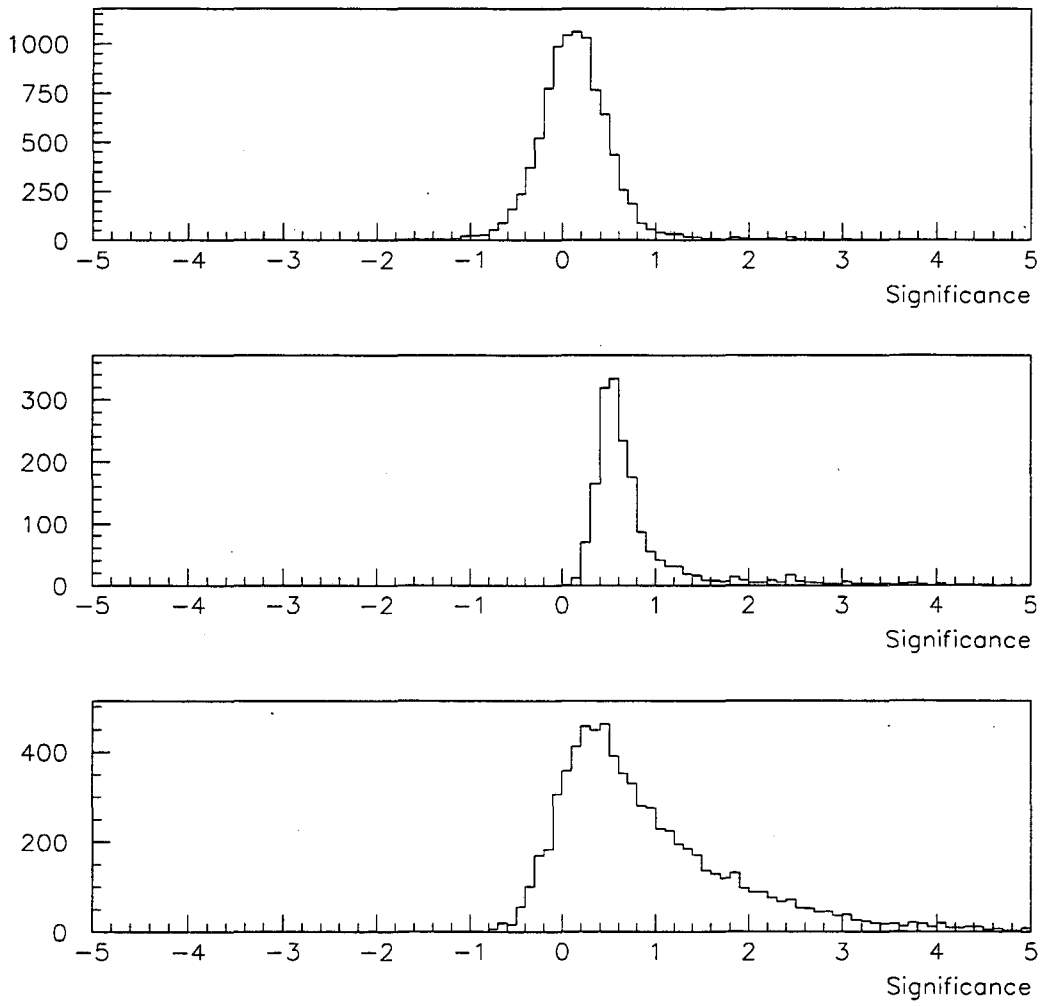

Figure A.2: The *lifetime significance* of events reconstructed as D^0 decays. The upper plot is raw data. The middle plot is the data accepted by the Neural Net. The bottom plot shows reconstructed Monte Carlo events. The plots reflect the performance of the Neural Net on the *lifetime significance* variable.

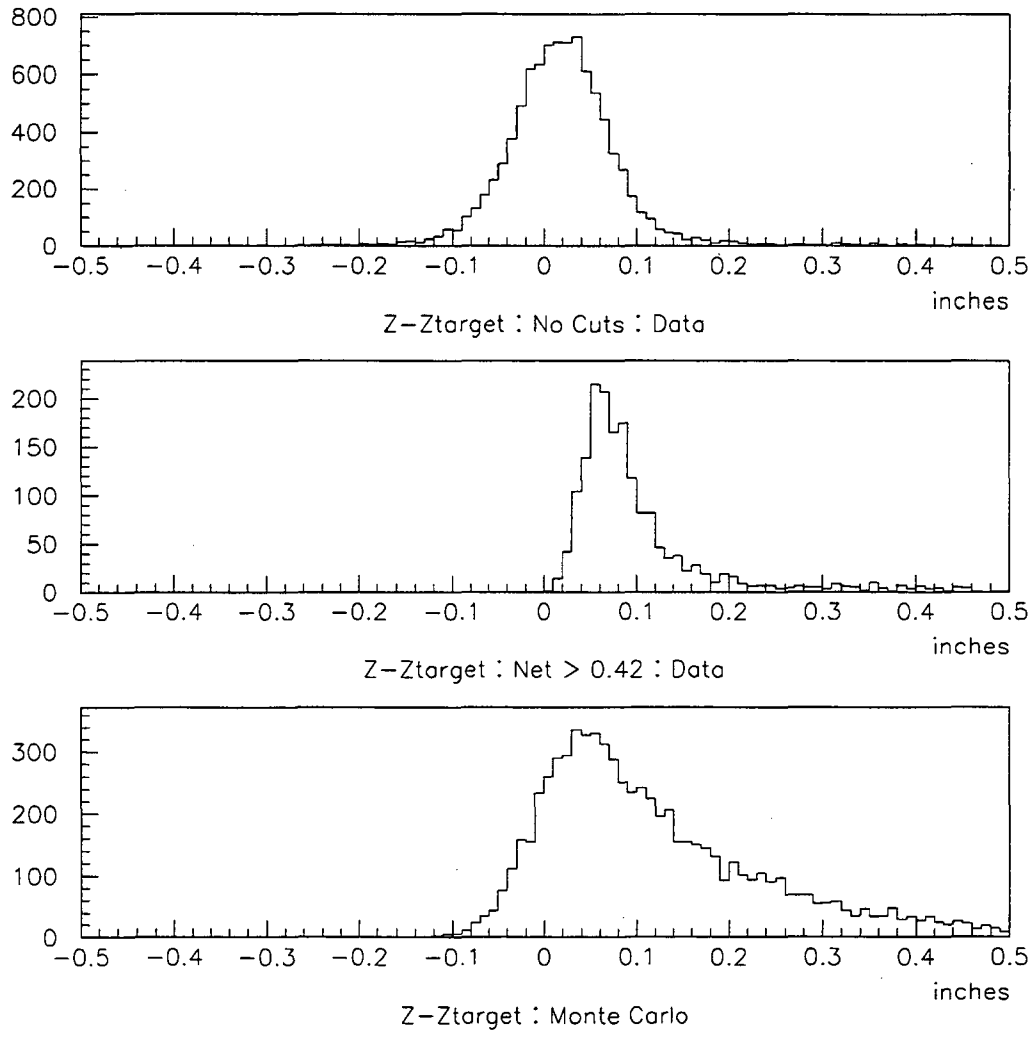

Figure A.3: The reconstructed Z-vertex minus Z-target. The upper plot is raw data. The middle plot is the data accepted by the Neural Net. The bottom plot shows reconstructed Monte Carlo events. The plots reflect the performance of the Neural Net on the reconstructed vertex.

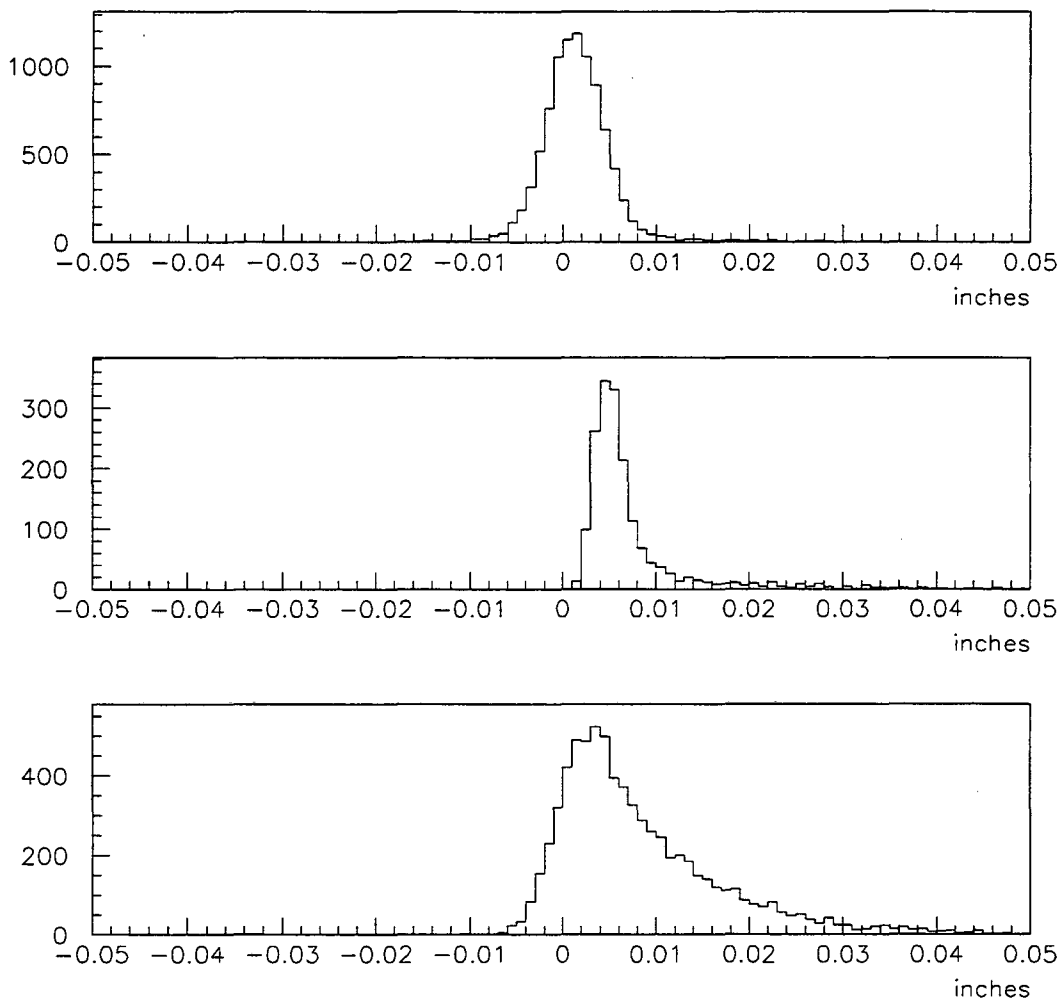

Figure A.4: The impact parameter difference. The upper plot is raw data. The middle plot is the data accepted by the Neural Net. The bottom plot shows reconstructed Monte Carlo events. The plots reflect the performance of the Neural Net on the *impact parameter difference* variable.

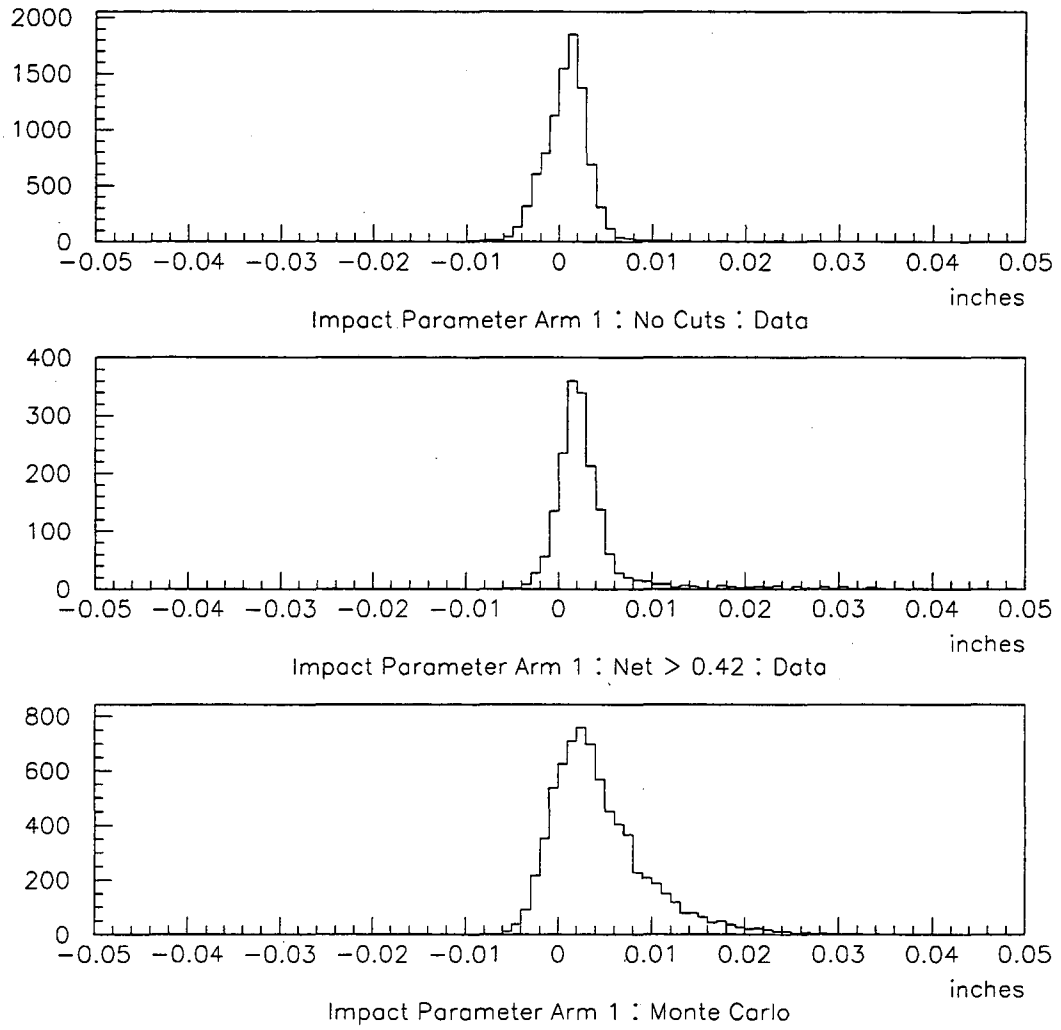

Figure A.5: The impact parameter in Arm 1. The upper plot is raw data. The middle plot is the data accepted by the Neural Net. The bottom plot shows reconstructed Monte Carlo events. The plots reflect the performance of the Neural Net on the *impact parameter* in Arm 1.

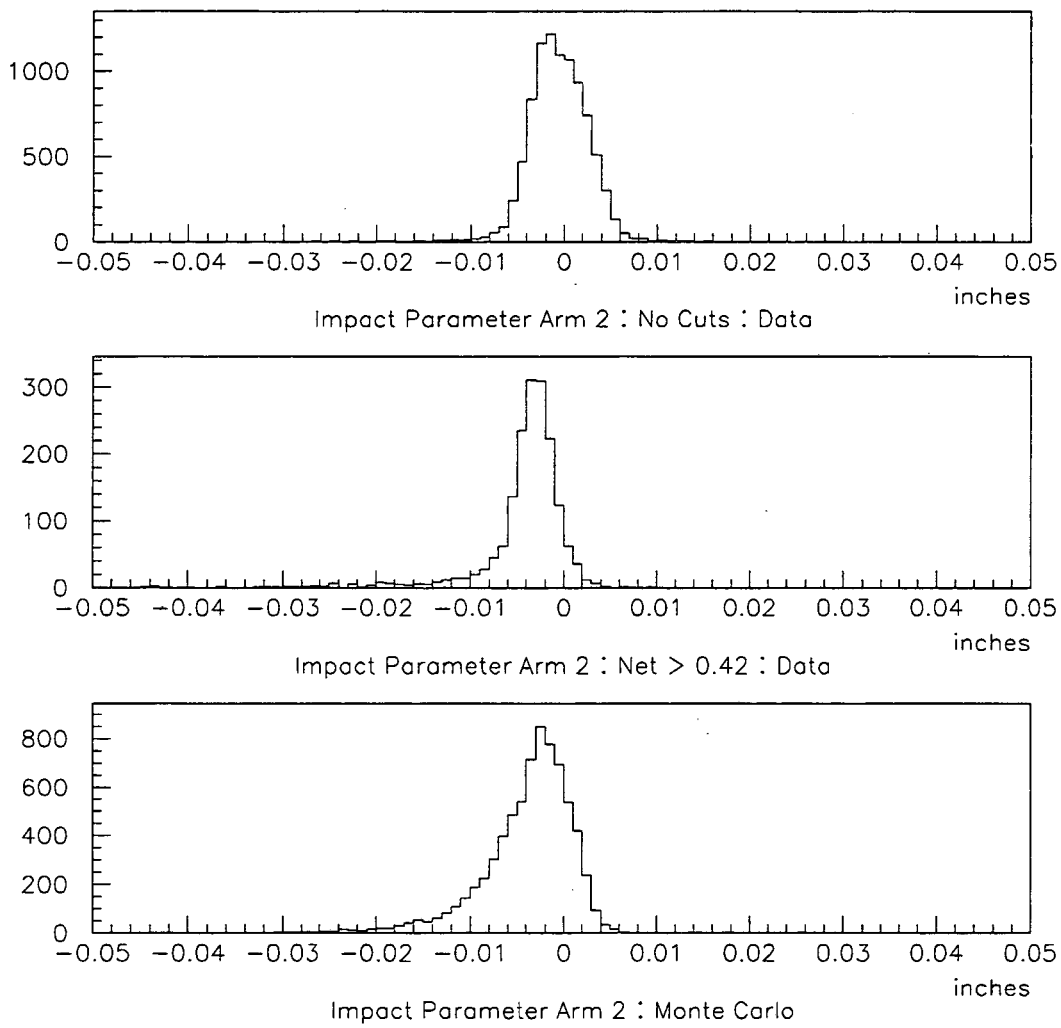

Figure A.6: The impact parameter in Arm 2. The upper plot is raw data. The middle plot is the data accepted by the Neural Net. The bottom plot shows reconstructed Monte Carlo events. The plots reflect the performance of the Neural Net on the *impact parameter* in Arm 2.

Ernest Orlando Lawrence Berkeley National Laboratory
One Cyclotron Road | Berkeley, California 94720

Prepared for the U.S. Department of Energy under Contract No. DE-AC03-76SF00098